Title

Manipulating and Measuring both Mechanical Forces and Genetic Factors to Improve Disease Models

Author

Mayner, Jaimie

Publication Date

2022

UNIVERSITY OF CALIFORNIA SAN DIEGO

Manipulating and Measuring both Mechanical Forces and Genetic Factors to Improve Disease Models

A dissertation submitted in partial satisfaction of the requirements for the degree of
Doctor of Philosophy

in

Bioengineering

by

Jaimie M. Mayner

Committee in charge:

Professor Adam J. Engler, Chair
Professor Eric Adler
Professor Pedro Cabrales
Professor Neil Chi
Professor Sylvia Evans
Professor Andrew McCulloch

2022

The Dissertation of Jaimie M. Mayner is approved, and it is acceptable in quality and form for publication on microfilm and electronically.

University of California San Diego

2022

DEDICATION

To my mother, father, brother and sister

TABLE OF CONTENTS

LIST OF FIGURES

ACKNOWLEDGEMENTS

I would like to thank Professor Adam Engler for his mentorship and support throughout my graduate studies. I am very grateful for both the freedom you gave me in choosing my project and to pursue the scientific questions I found most interesting, as well as the guidance and wisdom you provided in framing this investigation. I am especially appreciative of the patience you showed me, both in the beginning, when I first joined lab fresh out of undergrad, and towards the end of my PhD, when dealing with personal health issues. I am also thankful to the rest of my committee – Professors Eric Adler, Pedro Cabrales, Neil Chi, Sylvia Evans, and Andrew McCulloch – for their guidance through this process. In addition, I would like to thank my funding sources through the National Institutes of Health T32HL105373 grant as this work would not be possible without them.

I would also like to thank my lab mates in the Engler lab for their help and providing a friendly and collaborative environment that I truly enjoyed working in. In particular, I am incredibly grateful for the guidance Aditya Kumar and Pranjali Beri provided me when I was first starting. Lastly, I am grateful to all the undergraduate and Masters students who I had the joy of working with—Natalie Cramb, Cecilia Lee, Karington Cooper, Luke Butler, Elena Demeester, Shayan Alipourjeddi. Thank you for all your hard work and your enthusiasm, which helped keep me inspired over the years. I am excited to see the great things you will all do.

Finally, this journey would not be possible without the love and support of my family and friends. I am very grateful for parents, specifically my father for teaching me how to stay curious and my mother for instilling me with confidence. I also am very grateful for my brother and sister who both inspire me with their incredible work ethics. Thank you all for being there with me every step of the way and always finding ways to make me laugh.

Chapter 1, in full, is a reprint of the material as it appears in: Mayner J, Demeester E, Engler A.J. Chapter 14: Combining Genetic and Mechanical Factors to Model Disease, *Material-based Mechanobiology*, 2022, pp. 309-337 DOI: 10.1039/9781839165375-00309. The dissertation author was the primary author of this book chapter.

Chapter 2, in full, is a partial reprint of material as it appears in Mayner J, Masutani E, Demeester E, Kumar A, Macapugay G, Beri P, Lo Sardo V, Engler A.J. Heterogeneous Expression of Alternatively Spliced lncRNA mediates Vascular Smooth Cell Plasticity. Submitted. The dissertation author was the primary author of this paper.

VITA

2016 Bachelor of Science, University of California Los Angeles

2022 Doctor of Philosophy, University of California San Diego

PUBLICATIONS

LaMontagne E, Macdougall L, Papes F, Teng E, **Mayner J**, Sutherland B, Anseth K, Kloxin A, Muort, A, Engler A.J. Generating a Perfusable Vascularized Brain Organoid Model using Microfluidics and Photodegradable Polymer Scaffolds. In preparation.

Wu Z, Su J, Li F, Chen T, **Mayner J**, Engler A.J, Ma S, Li Q, Guan K. YAP silencing by RB1 mutation is essential for small cell lung cancer metastasis. Submitted.

Mayner J, Masutani E, Demeester E, Kumar A, Macapugay G, Beri P, Lo Sardo V, Engler A.J. Heterogeneous Expression of Alternatively Spliced lncRNA mediates Vascular Smooth Cell Plasticity. Submitted.

Mayner J, Demeester E, Engler A.J. Chapter 14: Combining Genetic and Mechanical Factors to Model Disease, *Material-based Mechanobiology*, 2022, pp. 309-337. In press. DOI: 10.1039/9781839165375-00309.

ABSTRACT OF THE DISSERTATION

Manipulating and Measuring both Mechanical Forces and Genetic Factors to Improve Disease Models

by

Jaimie M. Mayner

Doctor of Philosophy in Bioengineering

University of California San Diego, 2022

Professor Adam J. Engler, Chair

In order to improve disease models, understanding and manipulating the factors that contribute to cellular phenotype is of utmost importance. The role of genetics in disease, while long appreciated from a clinical standpoint, has become more elucidated by modern sequencing techniques. Mechanical forces include both the environmental forces that act on cells as well as the forces exerted by cells back on their environment. While focusing individually on genetics or mechanics is important, this dissertation aims to highlight the value of utilizing both in combination to improve disease modeling.

In chapter one, we first provide an overview of the tools that allow us to manipulate and study genetic risk for disease, including gene editing techniques as well as induced pluripotent stem cell (iPSC) technology, and then provide examples where they have been successfully utilized to improve our understanding of cancer and heart disease. We then describe progress in the field of material based-mechanobiology and the engineered systems for mimicking forces exerted on cells by the extracellular matrix (ECM), surrounding fluid, and neighboring cells. We conclude by highlighting studies that have successfully manipulated both genetic and mechanical factors to improve our understanding of different cancers and heart diseases.

In the second chapter, we provide an example of how combining patient derived iPSCs and haplotype editing with biophysical cell sorting can unveil insight into how the non-coding gene locus, 9p21.3, incurs risk for coronary artery disease. Utilizing adhesion-based sorting with a microfluidic device, we show that iPSC-derived vascular smooth muscle cells from patients with single nucleotide polymorphisms (SNPs) at 9p21 (RR) have increased phenotypic heterogeneity compared to those lacking the SNPs and isogenic knockouts, specifically with increased presence of a synthetic, non-contractile phenotype. We identified heterogeneous expression of an alternatively spliced long-non coding RNA within a RR patient population drives a subset of cells towards the synthetic phenotype, exacerbating disease and potentially explaining the incomplete penetrance of the disease locus.

The methodology highlighted here has broad applicability to a number of different diseases, highlighting the value of approaches that both manipulate and measure genetic factors and mechanics to investigate disease development.

Chapter 1. Combining Genetic and Mechanical Factors to Model Disease

1.1 Abstract

To study the origin of disease, which is complicated by patient-to-patient variability and tissue heterogeneity, it is necessary to study the root causes of both extrinsic and intrinsic mechanisms. While extrinsic factors are generally obvious for diseases, *e.g.* diet and exercise, intrinsic ones are less so, *e.g.* genetics or environmentally induced genetic stimuli. This chapter first summarizes recent work investigating the effect of inherited genetic risk using examples from cardiovascular disease and cancer and technologies such as iPSCs and/or gene editing. Second, we summarize recent advancements in materials-based mechanobiology in which mechanical stimuli, whether from the ECM, surrounding fluid, or neighboring cells, were modulated to study their role in disease. Finally, instances where both genetics and mechanics are jointly manipulated to model disease are discussed. Most genetic risk acts through unknown mechanisms; however, we propose future systematic study of these effects in combination to uncover novel mechanisms that would otherwise be missed if modeled separately.

1.2 Introduction

The classic Mendelian approach to disease inheritance, in which hereditary, single-gene mutations result in disease by loss of function, does not explain most inherited diseases or genetic predisposition. The complexity of diseases, with patient-to-patient variability and heterogeneity within diseased tissue, remains poorly understood. Cell–cell variability in gene expression (and phenotype) within a population is ubiquitous in disease and caused by (1) genetics, *e.g.* heterogeneous mutations within a tumor, and (2) asymmetric application of nongenetic stimuli on a population. These symmetry-breaking events are at the core of developmental biology and create distinct phenotypes arising through both extrinsic and intrinsic factors. Extrinsic factors include the large variety of complex environmental cues from different tissue niches, which include both biochemical and mechanical stimuli and will be the focus of this chapter. Intrinsic factors, although less understood, create the spontaneous diversification of clonal populations into distinct variants through some symmetry-breaking event propelled by a stochastic process that drives these discrete options, *e.g.* stochastic gene expression ‘‘noise’’[1]. Phenotype is driven by both genetic and nongenetic factors, and therefore studies in which these are independently investigated, while fruitful and tightly controlled, do not capture the entire picture of disease. Systems where both genetic and environmental factors and how they act together are modeled can elucidate novel pathways in disease development, prompting drug discoveries. This chapter will first focus on single-factor disease model systems in which genetics or mechanics alone are investigated. We will then conclude with a discussion of instances where both genetics and mechanics are jointly manipulated to model heart disease and cancer.

1.3 Modeling Disease with a Single Variable

1.3.1 Genetic Models

While disease development is a complex process that cannot be attributed to a single cause, significant progress can be made by developing models that alter a single variable and measure biological responses. Historically speaking, the medical field has long recognized the importance of genetics in disease risk, with physicians using family history to assess patient risk for a multitude of conditions. In addition to inherited genomic risk, acquired mutations, often attributed to environmental stressors[2–4], have long been hypothesized to play a role in late onset diseases, such as cancer[2,4,5]. However, genomic regulation is multilayered and remains poorly understood. Next-generation sequencing (NGS) technologies such as Illumina Sequencing, Roche 453 Sequencing, and Ion Torrent: Proton/PGM sequencing, coupled with novel genetic editing tools such as CRISPR[6], have ushered in a new era of disease modeling where the contribution of individual genes to disease pathogenesis can be modeled *in vitro*.

In more recent years, genetic reprogramming of primary cell lines into induced pluripotent stem cells (iPSCs) has become a valuable tool for studying a variety of cell types using recently developed differentiation protocols. Paired with the affordability and accessibility of modern next-generation sequencing, patient-specific genetics can be studied in a variety of diseases relevant cell types. However, when specific edits are required, gene editing has been made possible through nucleases, which create site-specific double-stranded breaks at the target location[7,8]. These breaks are repaired through homologous recombination (HR), which allows for a template sequence to be inserted, or nonhomologous end joining (NHEJ)[7,8]. Early genetic engineering methods include zinc finger nucleases (ZFN), which cut DNA at defined triplet nucleotide locations[9] and were used extensively in iPSC reprogramming[10]. However, cost and off-target cleavages led to more modern gene-editing nucleases, *e.g.* transcription activator-like effectors attached to nucleases (TALENs)[11] and ultimately the clustered regulatory interspaced short palindromic repeats (CRISPR)-Cas9 nuclease system. Unlike TALENs and ZFNs, which rely on chimeric protein binding to DNA, CRISPR/Cas systems bind to target DNA sites using a complementary noncoding RNA (guide RNA). CRISPR-Cas9 was developed from a naturally occurring adaptive immune response in bacteria, by which DNA from invading viruses are captured to create DNA segments, or CRISPR arrays, which can be utilized by the bacteria to create RNA segments to target the virus if it invades again, as the guide RNAs also bind Cas9 nucleases[6,8]. CRISPR has proved to be more efficient and robust due to the simplicity of its construction and its flexibility for use in many gene loci[12]. These major advancements in genome editing have revolutionized both basic and translational research and are summarized in **Figure 1.1**; specific disease modeling examples are described next.

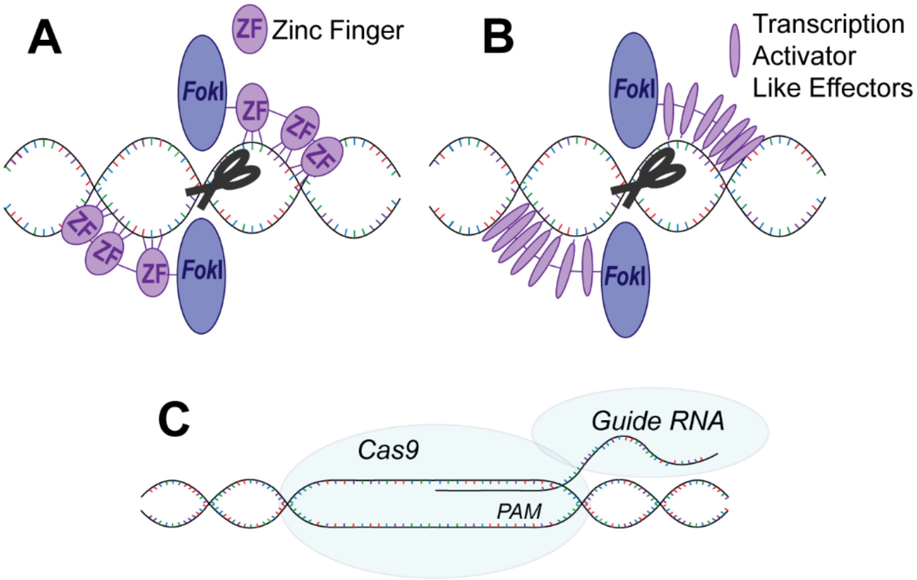

Figure 1.1. Genetic editing techniques: (A) Schematic of zinc finger (ZF) nuclease editing where at least 3 zinc finger monomers are required and must recognize 3 base pairs. FokI nuclease dimerizes and binds to perform the edit and cut. Some genomic regions are inaccessible to ZF nucleases due to chromatin compaction. **(B)** Schematic of TALE nucleases. Each TALE monomer recognizes 1 base pair, providing greater flexibility in the target sequence. TALE monomer recognition occurs via 2 hypervariable amino acid repeat variable di-residues. Again, the FokI nuclease dimerizes and binds for editing, and, again, some genomic regions are inaccessible due to compact chromatin. **(C)** Schematic of the CRISPR/Cas9 system, which recognizes genomic DNA by a PAM sequence. A single guide RNA recognizes the target genomic sequence. CRISPR/Cas9 only needs a short guide RNA for DNA targeting, unlike ZF and TALE nucleases. Simultaneous genomic modifications at multiple in-dependent sites are possible with CRISPR/Cas9.

1.3.1.1 Heart Disease

Cardiovascular disease (CVD) is the leading cause of death in the world[13], and, of that, coronary artery disease (CAD) is responsible for one in every five deaths in the developed world[14]. Family history has long been used in medicine to predict CAD; however, the search for the associated genes has remained mainly fruitless until the advent of modern sequencing techniques. Genome-wide associate studies (GWAS) have not only confirmed that genetics account for 50% of susceptibility[15] but have also identified genetic variants that increase risk[16–18]. At least 10^6 disease-causing single-nucleotide polymorphisms (SNPs) have been identified in the genome, but most are located in noncoding regions, making the mechanism through which they enhance disease risk enigmatic[19]. Three separate GWAS studies in parallel identified variants at the 9p21 locus to be associated with CAD as having the greatest correlation with CAD, making it the most impactful genomic risk factor. Like many other associated SNPs, it does not contain any annotated genes and is in a noncoding region of DNA[17,19–22].

Cardiovascular disease (CVD) is the leading cause of death in the world[13], and of that, coronary artery disease (CAD) is responsible for one in every five deaths in the developed world[14]. Family history has long been used in medicine to predict CAD, however, the search for associated genes has remained mainly fruitless until the advent of modern sequencing techniques. Genome wide associate studies (GWAS) have not only confirmed genetics account for 50% of susceptibility[15], but have also identified genetic variants that increase risk[16–18]. At least 10^6 disease-causing single nucleotide polymorphisms (SNPs) have been identified in the genome, but most are located in non-coding regions, making the mechanism through which they enhance disease risk enigmatic[19]. Three separate GWAS studies in parallel identified variants at the 9p21 locus to be associated with CAD as having the greatest correlation with CAD, making it the most impactful genomic risk factor. Like many other associated SNPs, it does not contain any annotated genes and is in a non-coding region of DNA[17,19–22].

To study how variants at 9p21 result in CAD, one group generated iPSCs from patients with and without homozygous risk variants (risk and non-risk). By differentiating the iPSCs into vascular smooth muscle cells (VSMCs), the group found that phenotype of VSMCs was impacted by the risk variants, notably that risk patient’s VSMCs had reduced contractility and adhesion strength. Because VMSCs function in blood vessels by contracting to regulate vascular tone and, during CAD progression and vascular remodeling, they become more proliferative and less contractile, the reduced contractility of the risk patient's VSMCs mirrored the disease status of patients. Isogenic comparison between VSMCs from the same risk patients with and without the SNPs was possible using TALENs to knock out (KO) the variant containing region. Isogenic VSMCs containing SNPs also had reduced con tractility and adhesion strength compared to their KO counterparts[23] **(Figure 1.2A)**. This example demonstrates that editing methods can dramatically reduce background genetic variation to more easily highlight subtle mechanisms associated with enhanced disease risk.

Another common cause of heart failure and hypertension and the leading cause of heart transplants is dilated cardiomyopathy (DCM)[24], which is characterized by ventricular dilation and systolic dysfunction. Of all DCM cases, 20–35% are familial, although incomplete penetrance and the large set of associated genes (420) make understanding its inheritance less clear[25]. A growing number of studies have similarly employed iPSCs to study the genetic causes of DCM, as iPSCs are an essentially infinite source of human cardiomyocytes and primary cardiomyocytes are both rare and difficult to isolate[26,27]. In one study, iPSC-derived cardiomyocytes were generated from DCM patients with a point mutation (R173W) in the TNNT2 gene and from unaffected healthy family members without the mutation[28]. TNNT2 encodes sarcomeric protein cardiac troponin T, one of the three subunits of the troponin complex, which regulates contraction and force production of cardiomyocytes through its regulation of sarcomere thin filament assembly and activity[29]. Cardiomyocytes from patients with the TNNT2 mutations exhibited abnormal sarcomere structure, altered calcium ion signaling, and decreased contractility[29].Other examples include but are not limited to using iPSC-derived cardiomyocytes from long QT patients with CALM2 mutations to faithfully recapitulate reduced action potentials found in patients[30] and from patients with Danon disease and LAMP mutations who had impaired calcium handling[31].

While this study serves as an example of how single-point mutations can model disease mechanisms and potentially outcomes, iPSC-derived progeny can also elucidate novel gene interactions. By sequencing a large DCM affected family, another study found that heterozygous sequence variants in TPM1, the tropomyosin 1 gene, and VCL, the gene coding for vinculin, co-segregate in individuals with DCM diagnoses[32]. Tropomyosin binds troponin and is also an actin thin filament protein involved in contraction, whereas vinculin is an actin-binding protein involved in focal adhesion (cell– ECM) and adherens junctions (cell–cell)[33]. Employing CRISPR to create a series of TPM1 and VCL variant combinations in patient-derived iPSCs revealed that cardiomyocytes from patients with both TPM1 and VCL variants had the greatest reduction in contractility, measured using TFM, and in disorganized sarcomeres[32]**(Figure 1.2B)**. This study serves as an example of how combinatorial effects from genetic variants can be linked to disease using genetic models employing novel gene editing techniques like CRISPR and biomechanical assays, like TFM, when inheritance patterns are not as transparent as single-gene Mendelian inheritance patterns.

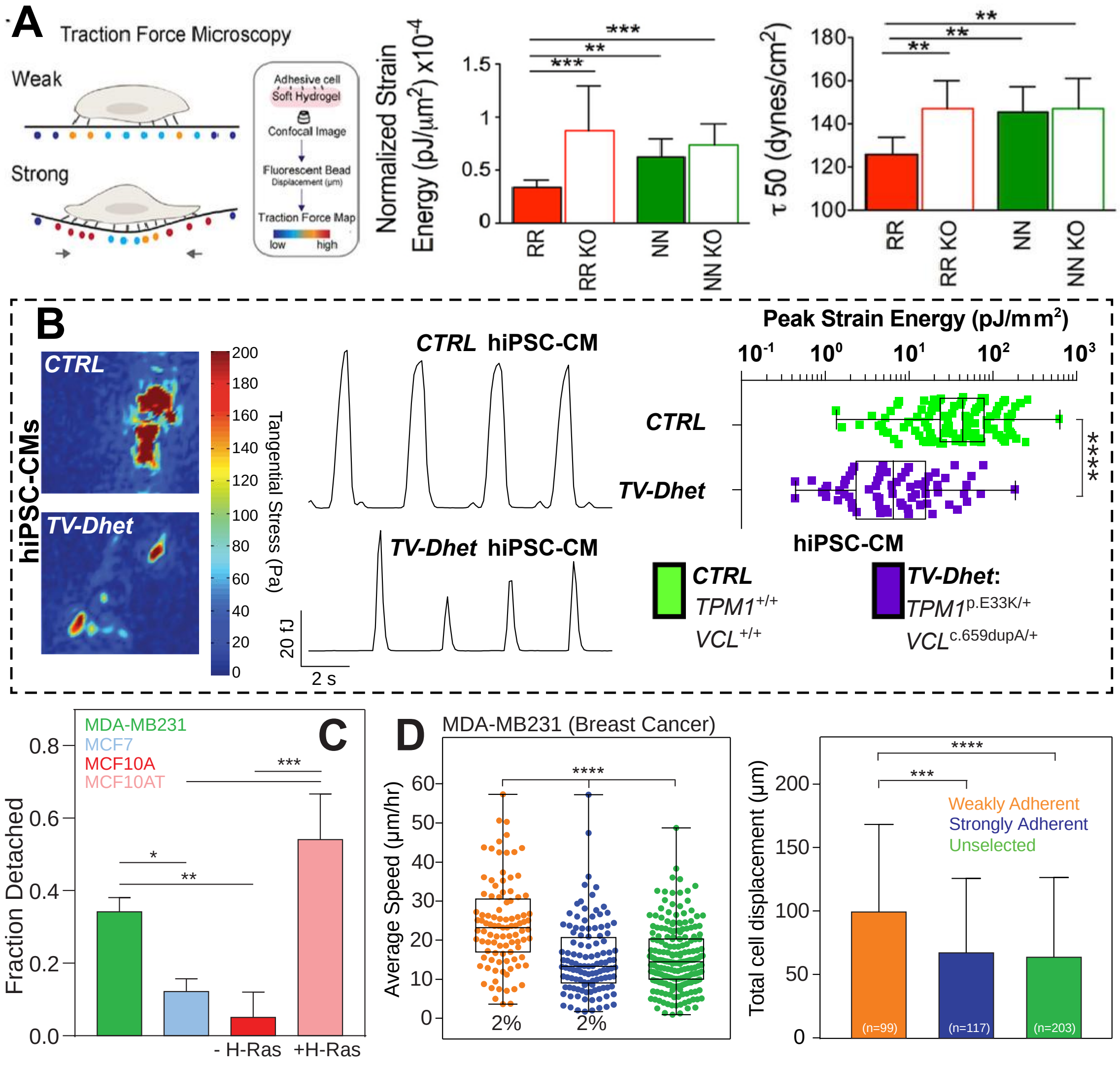

Figure 1.2. Genetic models to understand disease-in-a-dish. (A) Schematic of traction force microscopy (TFM) assay (left) applied to patients with (R/R) or without (N/N) variants in the 9p21 risk locus (center). Total strain energy was normalized to cell area and plotted (n > 25 in each assay; mean ± 95% CI). ***$p < 0.001$ one-way ANOVA-Bonferroni. Adhesion strength (right) assessed by spinning disk assay for SMCs of indicated genotypes (n > 10 in each assay; mean ± 95% CI.). **$p < 0.01$ one-way ANOVA-Bonferroni. Reproduced from ref. 23 with permission from Elsevier, Copyright 2018. **(B)** Single cardiomyocyte traction force microscopy studies of patient-derived iPSCs with double heterozygous variants in TPM1 and VCL, i.e. TV-Dhet, or control with normal copies of these genes. Tangential stress heat maps (left), strain energy time courses (center), and peak strain energy analyses (right) are shown. ****$P < 0.0001$; two-sided Student's t-test. Reproduced from ref. 32 with permission from Springer Nature, Copyright 2019. **(C)** Plot showing the fraction of detached cells from MDA-MB-231, MCF7, and MCF10A and their H-Ras–transformed counterparts MCF10AT after exposure to 250 dynes cm−2 of shear stress. *$P < 0.05$, **$P < 0.01$, and ***$P < 0.001$ for two-tailed unpaired t-test between lines. **(D)** Average speed (left) and total displacement (right) were plotted for MDA-MB-231 cells sorted by the indicated shear stress and allowed to migrate on collagen gels for 24 hours. Percentages reflect the portion of each population that detaches at a given stress. ***$P < 0.001$ and ****$P < 0.0001$ for two-tailed unpaired t-test between lines. Reproduced from ref. 37 with permission from AACR Publications, Copyright 2020.

1.3.1.2 Cancer

In contrast to inherited heart disease, many genetic causes of cancer are acquired. Mutations are often acquired in tumor suppressor genes, e.g. DNA repair genes such as p53, and oncogenes, e.g. receptors and small GTPases such as HER2 and RAS, respectively. However, there are inherited germline variants that predispose one to developing cancer, e.g. tumor suppressor genes BRAC1 and BRAC2, which increase likelihood of acquiring melanoma and breast, ovarian, and prostate cancer[34].To study oncogenes in disease models, such as the rat sarcoma (RAS) proto-oncogene family, including HRAS, KRAS, and NRAS, somatic cells can be transformed such that the exogenous oncogene of interest is incorporated and expressed. For example, to study breast cancer, non-transformed MCF10A breast epithelial cells can be transfected with constitutively active T24 H-Ras oncogene to create malignant MCF10CA1a cells that are malignant, or premalignant MCF10AT cells[35]. MCF10CA1 cells exert greater traction forces than MCF10AT and MCF10A[36], helping them to metastasize; adhesion differences that result from these mutations also regulate metastasis **(Figure 1.2C, D)**[37].

This common strategy has been pervasive in the literature over past decades but has recently been enhanced by modern editing methods such that lines can easily carry multiple oncogene or tumor suppressor mutations as occurs in vivo. Once edited, the impact of these edits – such as on the mechanical properties of cells – can be more easily observed. Studies have shown that the viscoelastic properties of cells are modified in cancer cells, specifically that metastatic cancer cells become more deformable. That helps cells to pass through denser adjacent stroma than softer healthy tissue[38,39]. One study compared the elasticity of oral carcinoma cell lines (Cal-33, Cal-27, PC1-1, PC1-13) to that of healthy oral keratinocyte cell lines (OKF-4, OKF-6) using a microfluidic optical stretcher and found that tumor grade and thus mutation state scaled with deformability[40]. Similarly, the viscoelastic properties of nuclei isolated from different cancer cell lines (MCF-7, IMR-5, and HEK 293T) showed that chromatin organization is spatially inhomogeneous, specifically that the outer periphery of the nucleus had reduced stiffness and was more sensitive to mechanical stimuli [41]. These changes in nuclear structure and others associated with cancer help the cells to both squeeze through more narrow networks and in mechanosensing and recognition of these environmental changes[42].

These findings on cancer cell deformability not only show promise for both novel diagnostics[43] but also as a research tool for identifying candidate genes (and mutations) in systematic genetic screens. Future applications of these methods could include CRISPR-based microfluidic screening system to identify novel tumor suppressor kinases. Loss of function aided by CRISPR/Cas9 and paired with a deformation-based microfluidic cell separation platform can sort and sequence flow-through cells, quickly identifying a library of kinases that enhance cell deformability and a potentially metastatic phenotype[44]. CRISPR/Cas9 system has also been used by other groups to screen for genes that regulate cell survival and drug resistance[45] or to investigate genetic networks through combinatorial perturbations[46], hinting that these CRISPR screens are powerful strategies for systematic genetic analyses of cancer. Moreover, they can be utilized to identify not only cell cycle regulatory genes but also genes involved in cytoskeletal rearrangement and other relevant structures in cancer.

1.3.2 Environmental Effects on Cells

While genetics can impact cell phenotype, environmental cues can also impact cell fate in development and disease. Accurate disease models should mimic not only native tissue in the chemistry of soluble factors and scaffolding but also its mechanical properties. Gene expression and cellular phenotype more closely replicate healthy tissue by using biomimetic cell culture environments, and, importantly, the changes in the ECM environment during disease progression can also be modeled. The importance of replicating the mechanical signals from the environment, including from the ECM, neighboring cells, or surrounding fluid, is becoming a well appreciated feature of disease models **(Figure 1.3)**.

The relationship between mechanics and disease status is becoming more widely studied. In some pathologies, cell phenotype is defined by reduction in mechanical output, *e.g.* reduced cardiomyocyte contractility in dilated cardiomyopathy (DCM)[28]. In other diseases, e.g. cancer, the relationship is less understood. In both cases, the use of materials-based mechanobiological assessments adds valuable quantification to cell phenotype and is useful in genetic studies for uncovering molecular mechanisms linking genomic variants to disease predisposition. Mechanobiological measurements can include examining the extent of a cell's interaction with the extracellular matrix (ECM), such as the traction forces exerted by a cell onto its environment[36], especially in muscle[23,32] or the adhesion of the cell to ECM when exposed to fluidic shear stresses[37]. Cell–cell interactions can also be measured[38,47–51], a notable property for diseases in which such bonds are disrupted, such as endothelial barrier function in cardiovascular diseases[52,53]. The elasticity or viscoelasticity of a cell and specific organelles[54] is also related to a cell's ability to squeeze through the surrounding dense ECM network, an especially relevant metric for cancer cell migration[40,41,44]. Continuing to move smaller in length scale, the tension on individual proteins can be measured, which can provide insight into gene expression, structure, and disease phenotype[55,56].

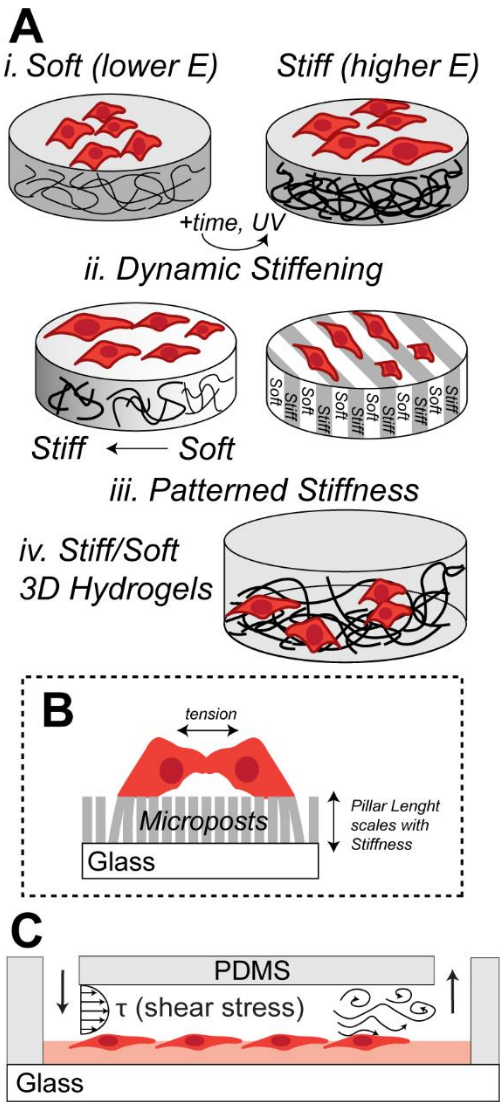

Figure 1.3. Schematic of mechanical environmental cues: **(A)** Cell–ECM interactions are commonly manipulated in culture by hydrogels (i) of different stiffness, (ii) of time-dependent stiffness, or (iii) that contain spatial patterns of stiffness. While these systems culture cells on top of the hydrogel generally, they can also be used (iv) in 3D systems where the material again can be soft or stiff depending on polymerization properties. In these systems, cells generate forces on the material. **(B)** Cell–cell interactions are also often probed in these systems. While panel A highlights continuous surfaces, discontinuous surfaces can also directly control and measure interactions, *e.g*. with microposts and cell–cell and cell–matrix tractions. **(C)** In contrast, forces can be directly applied to cells, such as with fluid shear stress. In microfluidic systems, a chamber is fabricated where cells reside and fluid is pumped through the chamber (see inflow and outflow arrows at the ends of the device made out of polydimethylsiloxane [PDMS]). Fluid motion obeys pipe flow and exerts a defined, laminar shear stress on cells, which can become turbulent in the presence of obstructions, *e.g*. stenosis.

1.3.2.1 Modeling Cues from the ECM

1.3.2.1.1 Hydrogels Mimic ECM Stiffness and Viscoelasticity

ECM is a three-dimensional fibrous network comprised of various amino acid and sugar-based macromolecules that provide functional and biochemical support for cells, control tissue structure, and diffusion of nutrients, growth factors, and metabolites. ECM is tissue specific with different protein compositions, resulting in unique integrin-binding profiles and different bulk mechanical properties, such as tissue stiffness. Synthetic hydrogels – which are covalently linked networks of polymers – are often used to model ECM in a reproducible manner because they can decouple chemical, physical, and biological properties in ways that native ECM cannot[57].Natural hydrogels can also be made utilizing fibrous proteins, such as collagen, fibrin, glycosaminoglycans, and polysaccharides[58]. While biocompatible, these naturally derived polymers are less manipulatable because properties are coupled; as one increases protein concentration (a haptic cue), the matrix also stiffens (a mechanical cue). Therefore, synthetic polymers are often used in a reductionist manner to decouple properties.

Hydrogel mechanical properties depend on the rigidity of the original polymer chain, a product of the chemistry of its monomer, the density of the chains, the degree of the crosslinking, and the degree of swelling due to hydrophilic/hydrophobic balance. To mimic the elasticity of the specific tissue of interest, for a chosen hydrogel, the polymer density or the degree of crosslinking of the polymer can be adjusted[59]. Crosslinking can be either physical, using noncovalent hydrogen bonds to entangle polymers chains, or chemical, through covalent bonds between functional groups on the polymers. Adjusting the pH, temperature, or ion concentration of the surrounding solvent can all promote physical crosslinking, and the use of linker molecules, photo initiators and UV, and enzymes can all be utilized as crosslinking agents for chemical polymerization[60]. Cell responses to different stiffness, dimensionality, stiffness patterns, or temporal changes can all be used to study diseases, *e.g.* cancer and atherosclerosis,[61] which affect these parameters. For example, fibroblasts migrate faster on soft, 2D substrates[62,63] . Within the tumor environment, increased fibrillar collagen deposition and the resultant increased tensile strength both contribute to cell–EM interactions that promote cancer cell invasion[64], as well as allow the tumor to grow in size and displace host tissue[65]. Similarly, atherosclerotic lesions are characterized by increased collagen composition and are stiffer than healthy vasculature[66]. While these examples present 2D surfaces to cells, stiffness dependent behavior is also observed in 3D systems and depends on crosslinking type (covalent versus ionic) and pore size. Breast adenocarcinoma cells (MCF-7) seeded within 3D alginate hydrogels ranging between 150 and 4000 Pa show decreased viability with increasing stiffness[67].MDA-MB 231 cells, another breast cancer carcinoma, are more invasive, traveling greater depths into 3D collagen gels of greater stiffness above a pore size threshold[68]. Stiffness can even promote cell plasticity where cells undergo epithelial-to mesenchymal transition (EMT) and become more migratory and invasive in mammary[69–71], lung[72], hepatocellular[73], and prostate[74] carcinomas, among others. Even squamous cell carcinomas, *e.g.* oral (OSCC), exhibit plasticity and EMT on stiffer substrates, making them more migratory and invasive[75]. These cells exhibited memory of the stiffness of their past environment[75], an idea not unique to oral cancer, and has been noted in other tissues like mammary tumors[76] and colon cancer[77].

The importance of elasticity is well appreciated, but the ECM is not strictly elastic. Many soft tissues are viscoelastic, exhibiting stress relaxation in response to deformation, creep in response to mechanical stress, or dissipating mechanical energy stored in the material[78]. Notably, viscoelastic properties, including the rate of stress relaxation, are altered in diseased tissues like breast cancer[79]. Hydrogels with tunable viscoelastic properties are increasingly being used to study how time-dependent relation and creep properties impact behavior, including stem cell differentiation,[80] cell spreading, proliferation[78], and matrix formation. When the matrix is more plastic, cells actually switch between migration modes from protease-dependent to -independent mechanisms[81]. Cell spreading, traction forces, and focal adhesion size can indeed scale with stiffness but can also be independent of plasticity[82]. While many questions are still unanswered, viscoelasticity is being recognized for its role in regulating cell phenotype[83].

1.3.2.1.2 Dynamically Stiffening Hydrogels

While materials can passively creep or relax over time, materials can also be actively driven to soften or stiffen as would occur during disease remodeling *in vivo*. Dynamic materials can mimic disease processes like fibrosis, including tumor stiffening, to interrogate the timescale over which cells probe their environment or even change shape to model developmental processes and disorders. For example, polyethylene glycol (PEG) hydrogels have been engineered to dynamically stiffen and mimic the stiffness transition from healthy to fibrotic heart muscle using anthracene photodimerization. On these gels, cardiac fibroblasts exhibit rapid, stiffness dependent localization of nuclear factor of activated T-cells (NFAT), a transcription factor downstream of intracellular calcium signaling that activates fibroblasts[84]. Similarly, cell response timescales can be studied by designing hydrogels with tunable viscoelastic spectra; reversible boronate ester crosslinking creates tunable viscoelasticity, and fibroblasts cultured on these gels had reduced cell and nuclear area, focal adhesion tension, and localization of YAP/TAZ compared to cells on elastic hydrogels with similar storage moduli[85]; frequency-dependent viscoelastic material properties impact fibro-blast activation and YAP/TAZ translocation[85]. Overall, these highlight how materials with dynamic elasticity and viscoelasticity can elucidate the timescales at which cells sense their environment, specifically in the con-text of fibrosis. Dynamic materials can also elucidate signaling pathways that are not observable in static stiffness systems in the context of cancer. Mammary epithelial cells (MCF10A) cultured on methacrylated HA hydrogels undergo EMT upon stiffening; both the degree of stiffening and time cultured prior to stiffening regulate this transformation, but importantly tumor spheroids do not exhibit memory of the mechanics of the prior niche given their multiple, overlapping mechanotransductive signaling pathways[70] **(Figure 1.4A)**. While stiffness-driven EMT has been reported previously in static stiffnesshydrogels[69], this dynamic system was able to elucidate the cooperative effect of both paracrine signaling and stiffness-mediated changes leading to EMT[70]. Finally, dynamic materials can be used to study how shape changes that take place during development of direct cellular behavior and therefore also can be used in modeling developmental disorders. Dynamic shape changes occur during morphogenesis to give rise to more complex biological structures. To mimic such processes, such as formation of the heart tube or neurulation, one group designed a PEG diacrylate-based thin film incorporated with *ortho*-nitrobenzyl moieties, which through photodegradation induced swelling transforms from a flat 2D sheet to folded 3D structures via exposure to UV[86].These and other photodeformable polymer gels[87] show potential for revealing the signaling pathways induced by the complex structural changes of morphogenesis and could shed light on associated disorders.

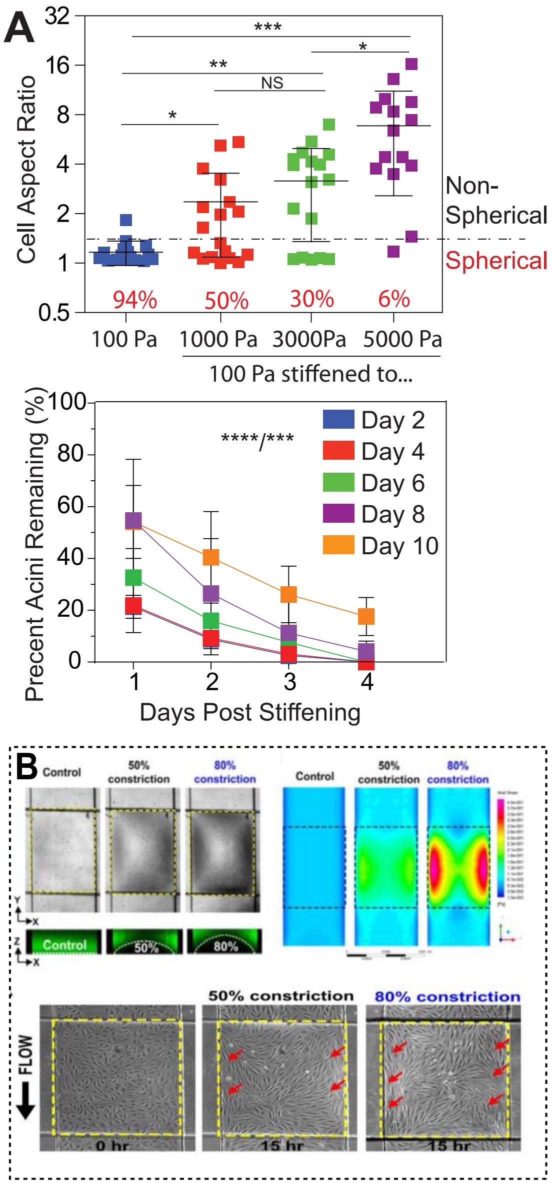

Figure 1.4. Dynamic Extracellular Cues: (A) Cell aspect ratio (top) is plotted with each color corresponding to its stiffening regiment indicated at bottom. The dashed line at 1.5 indicates an approximate transition point from spherical to non-spherical morphology. The percentage of data below the transition is shown, indicating the fraction of the population that remains spherical. $*P < 0.05$, $**P < 1 \times 10^{-2}$, and $***P < 1 \times 10^{-3}$from an unpaired Student t test (*n*>415 spheroids per condition). N.S., not significant. (Bottom) Cell clusters were also plated for the indicated days (colors in legend), stiffened, and tracked over 4 days post stiffening. $***P < 1 \times 10^{-3}$and $****P < 1 \times 10^{-4}****$ for two-way ANOVA indicating significance when comparing the effects of time pre- and post-stiffening. Reproduced from ref. 70 with permission from National Academy of Science. **(B; Top)** At right are representative bright-field images showing different channel constrictions at the stenosis region (yellow dotted box) with corresponding confocal images of the cell channel loaded with FITC dye illustrating constrictions (white dotted lines). At left, fluid simulations highlighting the wall shear stress across the 3D constriction (dotted box). **(B; Bottom)** Phase contrast images of TNF-α treated HUVECs monolayer at different constrictions after 15 h of perfusion culture ($1\ dyn/ccm^2$). Active cell alignment parallel to the flow was observed for HUVECs along the high shear zones (red arrows) for 50% and 80% constrictions. Reproduced from ref. 129, https://doi.org/ 10.1063/1.4993762, under the terms of the CC BY 4.0 license https:// creativecommons.org/licenses/by/4.0/.

1.3.2.1.3 Mechanically-Patterned Hydrogels

ECM changes with time, but it also changes spatially; cells move across stiffness gradients in a number of diseases, *e.g.* when cancer cells metastasize and migrate from the stiffer tumor to the softer surrounding stroma[88], or when fibroblasts and mesenchymal cells enter injured tissue, or when smooth muscle cells migrate from the tunica media into the intima of the blood vessel[89] .Hydrogels with patterned stiffness can be used to study how cells are directed by matrix stiffness (durotaxis) for a variety of tissue niches and diseases. Patterned regions of different stiffnesses were initially created using uncontrolled droplet mixing[63,90]. Conventionally today, patterns are typically created: (1) by controlled, radical-based photoinitiation using a photomask[91] , (2) by spatial composition of the precursor materials, or (3) by hydrogel thickness[92]. For light-based polymerization, photomasks can be designed with varying opacity or created by moving a mask during UV treatment[93]. Photoinitiators include those bound to polymers (*e.g. o*-nitrobenyzyl[94] or ketal-acetyl derivatives as photocleavable groups[95] and vinyl benzene, cinnamic acid, norbornene, or benzophenone as photocrosslinkable groups[92]) or those added exogenously, such as Irgacure[96]. For improved precision, the ratio of monomer to crosslinker can be controlled using hydrodynamic systems, like a combination of syringe pumps[97], a microfluidic gradient generator[98,99], or other unique devices[100]. Finally, stiffness patterns can be achieved through spatial control of hydrogel thickness. If the hydrogel is attached to a rigid substrate, the magnitude of the displacement field attenuates due to the no-slip boundary condition at the matrix substrate interface, and the amount of attenuation is inversely related to the matrix thickness[101].Therefore a substrate-bound chemically homogeneous hydrogel can have a patterned stiffness locally varying the thickness of the hydrogel. This can be accomplished by using pattered photomasks and layering gels to create distinct soft and stiff striped regions[102] or by layering beads beneath compliant gels[103].

Significant recent progress has been made in understanding cell behaviors on patterned substrates. For example, fibroblasts on collagen-coated hydrogels with 14 and 30 kPa regions exhibited increased migration speed when traveling ‘‘up’’ the stiffness gradient (soft to stiff) but turned away from the boundary when migrating on the stiff region[63]; this biased migration occurs in most adherent cell types and has been termed ‘‘durotaxis’’. Biased migration has been shown for fibroblasts and endothelial cells on fibronectin-coated hydrogels[104], for various cancer cell lines on fibronectin coated hydrogels[88], and for smooth muscle on collagen-functionalized hydrogels[105,106]. Speed and persistence in these regions depend on gradient range and magnitude (slope of the gradient) but also on how the cells are interacting with the gradient, *i.e.* durotactic behavior is often ligand specific[105]. Finally, patterns need not be smooth gradients but rather can be stripes or other shapes with near step transitions. Such patterns have been used to position motor neurons and myoblasts to create neuromuscular junctions[107]. With each of these patterns, the goal is always to improve the functionality of disease-in-a-dish model.

1.3.2.2 3D Systems Structural Properties

While stiffness has been extensively studied, ECM structure, porosity[108], fiber interconnectivity and tortuosity, fiber size[109], and fiber surface topography and chemistry[110] are becoming increasingly studied given their influence on cell behavior in 3D. The following is a summary of the materials-based mechanobiological systems used to study these variables independently, as outlined in **Figure 1.3**.

1.3.2.2.1 Electrospun Fibrous Scaffolds

Hydrogels cannot recapitulate 3D fibrillar architecture as in collagen and fibrin[111,112]. To overcome this limitation, polymers are often electrospun into a fibrous morphology, which involves extruding a charged polymer solution through a blunt needle across a large potential difference. A variety of polymers with different properties have been electrospun, including poly(glycolic acid) (PGA), poly(lactic acid) (PLA), poly(caprolactone) (PCL), polydioxanone (PDO), and even natural polymers like collagen (types I, II, III, and IV), gelatin, elastin, and fibrinogen; mixing synthetic and natural polymers is also possible[112].Electrospinning manipulates a variety of fibrous scaffold features ranging from fiber topography to mesh or network size of the spun fibers[113]. For example, by adjusting the viscosity or concentration of the polymer solution, the fiber diameter can be adjusted (increasing concentration increases diameter)[114]. To adjust the scaffold's thickness, the volume spun can be adjusted to the size and shape of the scaffold, and the ground targets geometry can be varied[115]. By rotating the ground target, fibers can be aligned to produce anisotropy of both the fiber orientation and bulk physical properties[116]. These properties have been investigated for their influence on cellular behavior. For example, PLA fiber alignment can guide migration of fibroblasts [117], filament curvature is sufficient to influence the direction of nerve cell outgrowth[109],and the expression of collagen genes and proliferation markers in fibroblasts increases with the decreasing diameters of silk fibers[118].

1.3.2.2.2 3D Printing

Three-dimensional (3D) printing, in contrast to traditional manufacturing processes, enables the fabrication of complex and diverse architectures through computer-aided design and layer-by layer application of materials. 3D printing allows for spatial patterning of cells and biomaterials to recapitulate the complexity of tissues and organs and has the potential for patient-specific disease modeling using computed tomography (CT) and magnetic resonance imaging (MRI) data[119]. To identify the minimum design requirements that allow for optimal tissue growth and function, such as size, choice of biomaterial ink, vascularization, and cell type composition, significant research efforts are still required. Furthermore, the variety of materials suitable for 3D printing, which must be mechanically suitable for extrusion yet stiff enough to maintain the desired architecture while layers are deposited are limited[120]. However, the spatial precision allowed by 3D printing methods has been useful for disease modeling of high-order tissues, in which cell–cell interactions are critical. 3D printing has been used to study a number of tissues and organs, such as bone[121], blood vessels[122], and skin[123]. For example, extrusion-based 3D printed gelatin methacryloyl (GelMa) scaffolds have been shown to trigger mineral deposition of osteoblasts in the absence of exogenous osteogenic factors, but osteoblasts seeded onto the same formulation in film failed to deposit minerals, suggesting that the 3D architecture of the scaffold promoted differentiation rather than its chemical cues[124]. In addition to recapitulation of architecture, 3D printing can also add precision to the placement of cells by using cell-laden viscous polymers. Manipulation of cell placement can be used to promote cell–cell interactions mimetic of native tissue, *e.g*. chondrocytes and MSCs embedded in alginate and printed with high spatial viability[125]. Conversely, modeling multicellular organ systems is complicated by tissue size, with larger organs requiring vascularization for their cells to maintain metabolic requirements[122]. Therefore, there has been a growing demand for functional vasculature for perfusion of biofabricated organs, with the ability to perform gas and nutrient exchange as well as waste product removal[126]. The precise placement of multiple cell types via 3D printing highlights its promise for creating more complex organs by simultaneously constructing an integrated vascular system. For example, multiple bioprinted and perfusable networks of capillaries and arteries have been achieved and are a significant step in overcoming this long-standing disease modeling limitation[127]. Vascular systems have also been fabricated by 3D printing and shown to support biopsied tumors, a useful attribute, as traditional tumor models are not able to support the highly vascularized nature of tumors in vivo. This was accomplished by 3D printing sacrificial PVA scaffolds embedded with different combinations of ECM (such as collagen and fibrin) and different geometries that supported endothelial cell infiltration and migration along the channels, resulting in functional microvasculature that was also able to support fluid flow[128].

1.3.2.3 Active Forces Applied to Cells

Environmental cues are largely passive and sensed by cells pulling or pushing on their niche. Conversely, external application of forces on cells, by matrix, other cells, or fluid, can also significantly impact cell function. The most common forces experienced are hemodynamic forces, and understanding how they affect vasculature has become increasingly important to model diseases such as CAD, strokes, and metastatic cancer. The use of 3D systems has been particularly useful to better understand the interaction of hemodynamic forces and cell tissue. Typically, blood flow is laminar and pulsatile. However, changes in vessel construct, such as bifurcations, turns, stenosis (*i.e.* stiffening and narrowing of vessel), and other disease phenotypes can cause disruptions to flow and change the shear stresses experienced by cells and surrounding tissue. For example, diseases such as atherosclerosis and thrombosis will characteristically show disturbed flow instead of laminar flow due to buildup of plaque, excessive clotting and stiffening of the arterial walls.

The hemodynamic response is complex and requires the interaction of different fluid forces and multiple levels of tissue. As such, studying diseases that are impacted by hemodynamics requires reductionist systems that can emulate both the relevant fluid and the tissue-induced mechanical forces **(Figure 1.4B).**[129] Such 3D systems make it possible to study the complexity of native-like tissues in response to hemodynamic forces in vitro. For example, vascular endothelial cells, which are in direct contact with blood flow and are the first to detect and implement a response, detect and respond to changes in shear stress and flow[130,131]. Disturbed flow induces their inflammatory response, reorients actin stress fibers, and changes nuclear morphology within endothelial cells. These behaviors are mediated by the YAP/TAZ pathway responding to disrupted flow, as shown in atheroprone models. While these examples use continuous flow, oscillatory shear is more representative and can sensitize cells even further. For example, atheroprone oscillatory shear decreases in inhibitory phosphorylation of YAP/TAZ, increasing activation of its downstream targets, whereas laminar shear stresses do not[132]. A similar study, also using HUVECs, showed that disturbed flow activated YAP activity and decreased its cytoplasmic retention, whilst unidirectional shear stresses (USS) suppressed YAP activity thus inhibiting atherogenesis[133]. While shear stresses classically effect endothelial cells, it also impacts many important blood components, e.g. platelets, which reduce their adhesion and clotting ability with increasing blood shear stress[134]. Despite our vascular focus, active forces and stresses are extremely prevalent environmental cues; this larger topic, the material-based mechanobiological tools used to measure them and their larger influence on cell function, is more thoroughly reviewed elsewhere[135–137].

One final point to emphasize is that, regardless of tissue, multiple active forces or multiple cell types can be present. While the systems just discussed isolate single forces, it is important to note that disease mechanisms are often dependent on multiple mechanical forces interacting with one another, *e.g.* shear stress and ECM stiffness, or multiple cell types, *e.g.* endothelial cells (ECs) and smooth muscle cells (SMCs). To examine these more complex systems, ECs and SMCs have been cocultured in microfluidic devices to study cell–cell interaction upon exposure to fluid flow. This EC-SMC-signaling-on-a chip was exposed to 1–1.5 Pa shear stress and strain of 5–8%, which resulted in the endothelial layer adopting a ‘‘cobblestone’’ morphology, while the smooth muscle cells aligned themselves perpendicularly to direction of flow. This study represents one of the first co-cultured systems able to mimic the construction of the vasculature and respond to its mechanical environment in vitro[138]. Subsequently, several other multiforce/cell systems have been fabricated. For example, atheroprone vasculature develops inflammatory plaques in part from disturbed flow and recruited immune cells. Bifurcated flow-through slides seeded with HUVECs have been used to model this system. Nonuniform shear stress and inflammatory cytokines greatly enhanced monocyte cell adhesion and changed endothelial gene expression; telmisartan was able to inhibit this response via downregulation in VCAM-1, a protein involved in leukocyte adhesion[139]. These studies ultimately show the importance of using multivariable systems to elucidate cell–cell responses to their mechanical microenvironment.

1.4 Combining Genetic and Environmental Factors to Model Disease

While the previous section focused individually on genetic or environmental factors, their combinatorial effects are becoming well recognized for their importance in initiating and regulating disease pathologies[140]. Their continued study can improve our ability to estimate patient risk attributes[141], improve understanding of biological pathways and dose–response relationships, provide clarity on heterogeneity across studies[142], and identify novel candidate genes[143]. Environmental risks that can aggravate genetic causes of disease are not restricted to traditional concepts, such as smoking or UV exposure, increasing the risk for cancer but also include endogenous molecules' more subtle changes within a tissue that develop over the natural progression of disease and aging[141]. Often environmental factors will ‘‘reactivate’’ and upregulate expression of noncoding DNA, which itself can contain single nucleotide polymorphisms (SNPs) that exert control over signaling and result in a higher likelihood of disease[17,144]. The vast majority of SNPs are present in noncoding regions leading to incomplete penetrance[145] and highlights the need for disease models to capture conditions that lead to the disease phenotype in order to study mechanism. Next we review major organ systems and diseases where combinatorial effects have been identified thus far.

1.4.1 Heart Disease

Significant risk for coronary artery disease is inherited, although 23 of the 33 genetic risk variants for CAD identified by GWAS act through unknown mechanisms[17]. Clearly, approaches that model in vivo mechanical signals along with patient-derived iPSC present potentially fruitful methodology for resolving signaling mechanisms. For example, iPSC-derived endothelial cells cultured with microfluidic devices respond to proangiogenic growth factors and shear stresses to form functional and perfusable capillaries[146]; forces also enhance EC differentiation[147] and make their behavior more representative and patient specific for drug toxicity studies[148]. Overall, iPSC-ECs have been shown to be a reliable and reproducible source of ECs for disease modeling using 3D vascular networks, providing opportunities for genetic studies in which microphysiological conditions are mimicked. In this section, we summarize several recent case studies of gene–environment interactions, organized by their system and specific cardiovascular disease.

As a first representative example, patient-derived iPSCs are differentiated (in this case into SMCs) and fashioned into a 3D tissue (in this case self-assembled rings)[149]. Here, iPSCs were obtained from a patient with a loss-of function, premature termination in exon 10 of the elastin gene (ELN), resulting in supravalvular aortic stenosis syndrome (SVAS). SVAS is characterized by SMC hyperproliferation that narrows the ascending aorta[150]. Patient iPSC-VSMCs had reduced contractile strength and were also more proliferative[149] in these rings when subjected to force. This example, nearly six years old now, represents an early, albeit superficial analysis of disease mechanisms induced by a combination of gene–environment stimuli. More complex bioreactors with a fiber mesh and pulsatile flow conditions[151] or even decellularized blood vessels[152] under flow are technological improvements on the environment that should be applied to the ELN truncation to further probe it.

A second, more complex and recent example employs tissue-engineered blood vessels made from collagen, lined with endothelial cells, and perfused with media using a peristaltic pump. iPSC-SMCs from patients with Hutchison–Gilford progeria syndrome (HGPS) were used in this system to study how their accelerated aging phenotype was affected by perfusion and the presence of collagen. HGPS is a rare genetic disorder caused by an altered form of the Lamin A gene, LMNA, resulting in nuclear accumulation of progerin, a truncated lamin A protein[153]. The main cause of death of HGPS patients is cardiovascular disease, but our understanding of its cardiac specific mechanisms is limited. With this study, authors investigated the effect of progerin and aging in general, using iPSC-derived SMCs from a HGPS patient in this tissue-engineered blood vessel system. HGPS iPSC-SMCs had reduced vessel wall diameter, increased medial wall thickness, and increased calcification and apoptosis compared to TEBVs fabricated from healthy patient iPSC-VSMCs[154]. HPGS patient-derived iPSCs but not healthy patient-derived cells had an exacerbated inflammatory and DNA damage responses to the strain in this system caused by pulsatile flow. This phenotype could be reversed by lovastatin, a drug that is used in combination with other statins to extend HGPS patient life[155]. To further mimic blood vessels, this same group differentiated patient-derived iPSCs into both ECs and SMCs rather than just the SMCs. When patient matched, HGPS ECs aligned with flow but exhibited reduced gene expression responses to flow. HGPS vessels also exhibited a reduction in both vasodilation and vasoconstriction, while mixed vessels only exhibited reduction in vasodilation[156]. Overall, this study served as an example in which coculture of iPSC-derived ECs and VMSCs can elucidate how genetics influence responses to mechanical forces, such as those induced by fluid flow. It also points out the importance of isogeneity.

While the previous examples focus on vascular models, iPSC-derived cardiomyocytes have also been used extensively to investigate the role of biomechanical cues in genetic heart diseases. For example, cardiac microtissues (CMT) engineered from iPSCs from patients with DCM have been used to investigate the pathogenicity of genetic variants. Mutations causing truncations of the massive sarcomere protein titin (TTNtv) are the most common genetic cause of DCM. 3D CMTs suspended between PDMS pillars, as discussed in previous sections, more faithfully recapitulate native cardiomyocyte architecture and mechanics, promote maturity, and improve sarcomere alignment. Contractile function of iPSC-derived CMTs from patients with mutant titin TTNtv was reduced compared to those from wild type patients. By combing this sort of functional analysis with RNA-seq analysis, the group also found that certain missense mutations were more tolerated than others. Namely truncations in the A-band domain of the TTN impair contraction more than truncations in the I-band domain, which are less likely to result in DCM. A-band truncations also resulted in impaired response to mechanical stresses, accomplished by altering the PDMS post stiffness. To ensure that observed functional differences were not due to differences in background genetics, TTNtv was also introduced into independent iPSC lines using CRISPR/Cas9, to create isogenic comparisons with only the truncation of titin varied. Overall, this study provided genomic insights into DCM, finding that while both A- and I- band titin truncations result in contractile deficits, alternative exon splicing mitigates pathogenicity of I-band TTNtv[157].

Finally, while these genetic studies using biomimetic culture conditions have alluded to the importance of physiologically relevant mechanical stimuli, another study demonstrated that genetically linked disease phenotype may only be detectable under the appropriate environmental conditions. While GWAS identified numerous common polymorphisms associated with CAD, the majority are in noncoding genomic regions, making how they regulate cell function and contribute to disease largely unknown. To study how SNPs at the 9p21 locus, one such noncoding region with the greatest disease association

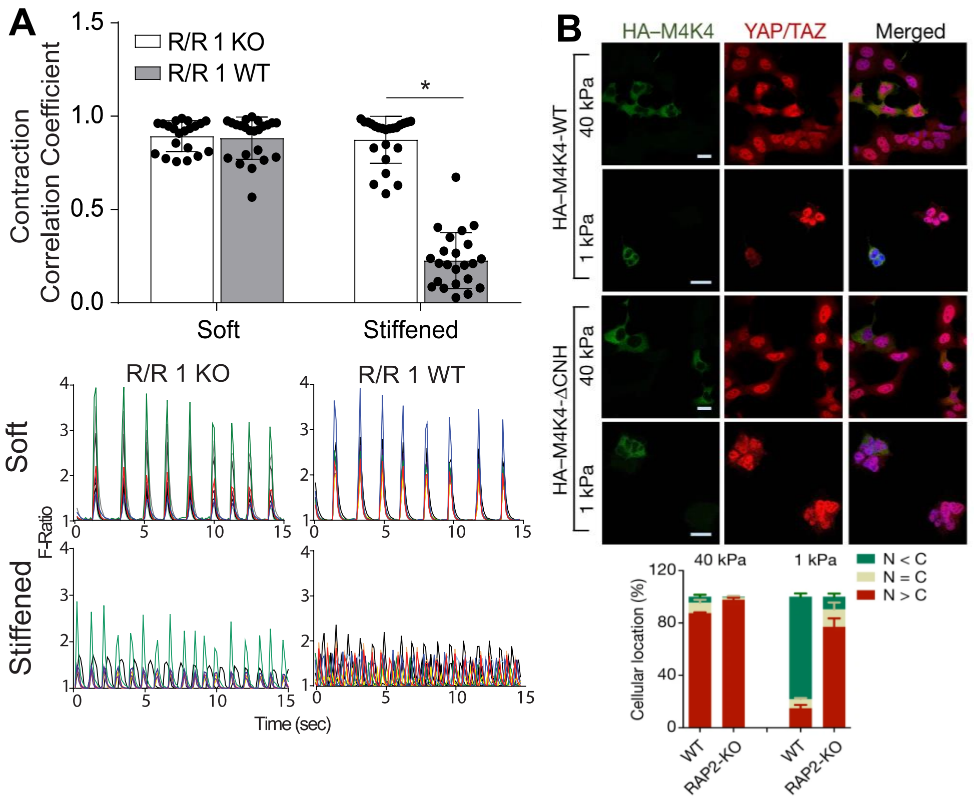

Figure 1.5. Combining gene-environment studies to understand their interplay: (A) At top is plotted the contraction correlation coefficient for R/R cardiomyocytes, with or without the 9p21 locus knocked out.$* p <$ 0.01 for all comparisons; one-way analysis of variance (ANOVA) followed by Tukey's multiple comparison test. At bottom are representative spontaneous Ca2 + transients plotted as the fluorescence intensity F-ratio over a 10-s time interval for the corresponding genotypes. The different colors represent transients from different cells. Reproduced from ref. 158 with permission from Springer Nature, Copyright 2019. **(B)** Expression of wild-type MAP4K4 (M4K4-WT), but not the citron domain-deleted mutant (M4K4-DCNH), rescued localization of YAP and TAZ in MM 8KO (MST1/2-MAP4K1/2/3/4/6/7-8KO) cells at low stiffness. HA, hemagglutinin. Combined signals from HA–MAP4K4 (green), YAP and TAZ (red), and DAPI (blue) are shown. Below is a plot that quantifies YAP and TAZ localization. Reproduced from ref. 165 with permission from Springer Nature, Copyright 2018.

leading to CAD, iPSC technology and dynamic PA hydrogels with controllable stiffness were used. In a physiological environment mimetic of healthy tissue, cultured cardiomyocytes from iPSCs from patients who are homozygous for cardiovascular-risk alleles (R/R) and cardiomyocytes from iPSCs from healthy, homozygous for non risk alleles (N/N) both contracted synchronously, independently of genotype. However, once the hydrogels were stiffened, to mimic fibrosis, only the R/R iPSC-cardiomyocytes contracted asynchronously, while the N/N iPSC-cardiomyocytes were able to remain synchronous

(Figure 1.5A). These mechanically induced phenotypic changes were associated with increased expression of a short isoform of ANRIL, the long noncoding RNA located in the 9p21 risk locus. ANRIL induced a c-Jun N-terminal kinase (JNK) phosphorylation-based mechanism that impaired gap junctions, specifically resulting in loss of connexin-43 expression. TALEN-mediated deletion of the risk locus was sufficient to prevent the stiffness-induced asynchronous contractions, in addition to a JNK antagonist[158] . Overall, this study revealed the potential for unveiling previously unknown functions of noncoding loci by employing microenvironmental models with relevant mechanical stimuli and iPSC technology. As the relevance of noncoding loci in disease becomes increasingly evident, the utility of strategies that employ both mechanical and genetic factors to model disease becomes increasingly important.

1.4.2 Cancer

While the proportion of cancer phenotype attributed to germline genotype, or inherited cases of cancer, is not as great as inheritance of heart disease, it is still a considerable proportion of heritable cases (for example 30% for breast cancer in Nordic countries[159,160]) and acquired genetic mutations with combined effects from gene–environment account for even greater proportions. Studies investigating how genetic factors, both acquired and hereditary, interact with the environmental factor have the potential to unveil novel mechanistic information and even identify new genetic risk factors. Explorative gene–environment interaction studies aim to identify such pathways[161]. In this section, we summarize several recent case studies of gene–environment interactions.

Exploration of gene–environment interactions date back several decades, with one early example to understand how H-RAS transformation leads to substrate adhesion–

independent growth. While substrate adhesion plays a role in regulating cell growth of normal cells, it has long been recognized that oncogene-transformed cells grow and proliferate independently of substrate anchorage regulation. To investigate this, H-RAS-transformed fibroblasts and nontransformed controls were cultured on different-stiffness collagen-coated PA substrates. Nontransformed cells had decreased rates of DNA synthesis, increased rates of apoptosis, decreased cell spreading area, and decreased traction forces on flexibility compared to stiffer substrates. However, transformed cells lost this stiffness response, maintaining proliferation and apoptosis rates as well as spreading and traction forces. Similarly, the tumor-initiating glioblastoma (GBM) cells are insensitive to stiffness cues of laminin-functionalized hydrogels, evading inhibition of spreading, proliferation, and migration typically imposed by softer ECM. Constitutive activation of RhoA restricted 3D invasion of GBM spheroids and restored stiffness-dependent spreading and motility[162]. Overall, this suggests that oncogenic mutations may contribute to a loss in mechanosensing, explaining their unregulated growth[163].

Epithelial carcinomas are the most common type of cancer and the focus of recent research, including that in which both mechanical and genetic cues are modulated. For example, Hippo pathway effectors YAP and TAZ, which are known for their role in mechanosensing ECM composition and mechanics, were investigated for their role in regulating focal adhesion (FA) formation. First, the authors found that, by controlling FA formation and cell spreading area through micropatterning fibronectin onto different stiffness surfaces, FA formation and cell size correlated with YAP nuclearization. Cells transiently overexpressing YAP and TAZ mutants had either cytoplasmic or nuclear localization through their inability to either be phosphorylated – trapping them in the nucleus

– or, lacking the PDZ domain required for nuclear shuttling, sequestering them in the cytoplasm. Moreover, transcriptionally active YAP but not TAZ increased FA signaling. This study, by finely tuning both the mechanical environment the cells experience as well as their gene expression, was able to provide new insights into the mechanism of YAP mechanosensing[164]. Another study investigating the Hippo pathway in breast cancer cells found that by deleting different GTPases and monitoring YAP/TAZ, the group identified RAP2 as a key intracellular signal transducer; deletion of RAP2 blocked regulation of YAP and TAZ by stiffness signals and promoted aberrant growth **(Figure 1.5B)**. By deleting or overexpressing targets and measuring nuclear translocation of YAP/TAZ on different stiffnesses, the study determined that matrix stiffness activates PDZGEF1 and PDZGEF2 to then activate RAP2. In low-stiffness ECM, RAP2 binds MAP4K4/5/7, which inhibits YAP and TAZ through LATS1 and LATS2[165]. Overall, these studies validated the importance of YAP and TAZ in mechanical regulation of transcription and that YAP has a more context-dependent role in mechanotransduction[164,165].

Finally, the cooperative effects of oncogenic transformation and matrix stiffness have also been investigated in the context of EMT using isogenic comparisons of nontransformed and H-RAS-transformed MECs (MCF10A versus MCF10AT) cells on PA gels of different stiffness. While both cell lines exhibited spreading, indicative of EMT, on stiff hydrogels, only transformed 10ATs exhibited heterogeneous behavior on soft gels. Within this heterogeneous population, those with stretched/mesenchymal morphology exhibited nuclear localization of EMT transcription factor TWIST1. While traditional mechanosensitive pathways, like YAP and TGF-b, did not mediate this spreading, the study found ERK activation induced the spreading on soft hydrogels via microtubule dynamics[166].

This is another example of tuning genetics (via transformation) and mechanics (ECM stiffness) in order to elucidate novel disease pathways.

1.5 Conclusions and Perspectives

Investigating the effect of a single variable, such as inherited genetic risk, by using, for example, iPSC technology and/or novel gene editing techniques, has improved our understanding of the pathology of several diseases. This chapter highlighted genetic studies in heart disease and cancer. For example, the role of SNPs in a noncoding locus, 9p21, in enhancing risk for CAD was investigated using iPSCs and TALENs to study smooth muscle cell phenotype[23]. Genetic risk for cardiomyopathies, such as DCM, has also more fruitfully been studied using iPSCs differentiated into cardiomyocytes. For example, utilizing CRISPR, the combinatorial effects of heterozygous. sequence variants in TPM1 and VCL genes, which co-segregate in patients with DCM, was demonstrated to disrupt sarcomere structure and function[32]. In addition to inherited genetic risk, acquired mutations have also been investigated. Oncogenes, such as RAS, have been investigated for their effect on cellular phenotype in cancer progression, which remains less defined. Comparing cell lines with different oncogenes and tumor suppressor gene mutations and correspondingly with different metastatic potentials, different biomechanical properties have been observed, *e.g.* differences in strength of adhesion to the ECM[34] traction forces[37], and cellular deformability[40], to name a few.

In addition to genetics, this chapter highlighted the use of material-based mechanobiology in which mechanical stimuli, whether from the ECM, surrounding fluid, or neighboring cells, were modulated to study their role in disease. For example, hydrogels have been widely used to investigate the effects of matrix elasticity on several processes, as stiffness changes have been implicated in diseases such as cancer and atherosclerosis, which are both characterized by fibrosis[61,64,67]. In addition to comparing cellular responses to hydrogels of different stiffnesses, stiffness patterns have been investigated, with durotactic behavior of many cell types being noted, and temporal changes in stiffness have also been investigated. For example, mammary epithelial cells cultured on hydrogels that stiffen over time demonstrate EMT, important in cancer metastasis[70]. Stiffness-dependent behavior is also observed in 3D systems.

In addition to stiffness, porosity, fiber interconnectivity, and topography are important in their influence on cell behavior in 3D. Both 3D printing and electrospinning are valuable methodologies for studying such variables systematically. 3D systems have also been important in their role in studying the impact of hemodynamics on phenotype, which is important in the study of diseases in which flow is disturbed, such as during atherosclerosis in which plaque buildup leads to stenosis[129]. Microfabricated systems that model these changes in arterial structure have been successfully utilized to demonstrate morphological changes in endothelial cells in response to fluidic shear stress,[130,131] as well as activation of important mechanotransduction pathways, such as the Hippo pathway[132].

While focusing individually on genetics or mechanics is important, their combinatorial effects are increasingly becoming recognized for their importance in disease pathology. Most genetic risk variants identified through GWAS for CAD act through unknown mechanisms[20] and therefore present a perfect opportunity for novel approaches in which patient-derived iPSCs, gene editing, and biomimetic microfluidic devices or tissue-engineered constructs may be used in conjunction. Both iPSC-derived endothelial cells and

SMCs have successfully been used in such systems to unveil novel signaling mechanisms activated through hemodynamic forces such as shear stress or flow-induced vessel strain[146–149,151]. Similarly, iPSC-derived cardiomyocytes have been utilized in more biomimetic cardiac tissue constructs[157]. Dynamically stiffened hydrogels have been used with TALEN-edited iPSC-derived cardiomyocytes to elucidate mechanisms through which SNPs at a noncoding locus result in disease in response to fibrosis[167]. In the context of cancer, oncogenic mutations have been investigated in different stiffness conditions, with studies highlighting the resultant loss in mechanosensing[163]. Simultaneously controlling gene expression and the focal adhesion area through microcontact printing has also been used to study Hippo pathway effectors YAP and TAZ[164]. Deletion of various GTPases and culturing gene-edited breast cancer cells on dynamically stiffened hydrogels have also revealed novel regulators of the Hippo pathway[157].

Overall, these studies show evidence for the power of more cross disciplinary studies in which both genetics and mechanical stimuli are manipulated. Combinatorial effects from the environment and genetics have long been appreciated in disease, and therefore systems that systematically manipulate these parameters in conjunction can uncover novel mechanisms that would otherwise be missed if modeled separately. Studying genetics or biomechanics in an isolated system, though useful, can run the risk of oversimplifying the effect of each factor. As we further develop the field of materials-based mechanobiology, combined systems will become crucial to further elucidate the interplay between the multiple factors in a biological system.

1.6 Acknowledgements

The authors acknowledge support from National Institutes of Health grants R01AG045428, R01NS116802, R01CA206880 and R21CA217735 (to A.J.E.), and as well as support from the National Science Foundation grant 1763139 (to A.J.E.) for financial support. Chapter 1, in full, is a modification of the material as it appears in: Mayner J., Demeester E., Engler A. 2022. Chapter 14: Combining Genetic and Mechanical Factors to Model Disease. *Material Based Mechanobiology*. DOI: 10.1039/9781839165375-00309. The dissertation author was the primary author of this chapter.

Chapter 2. Heterogenous Expression of Alternatively Spliced lncRNA mediates Vascular Smooth Muscle Cell Plasticity

2.1 Abstract

9p21.3 locus polymorphisms have the strongest correlation with coronary artery disease, but as a non-coding locus, disease connection is enigmatic. The lncRNA ANRIL found in 9p21.3 may regulate vascular smooth muscle cell (VSMC) phenotype to contribute to disease risk. We observed significant heterogeneity in induced pluripotent stem cell-derived VSMCs from patients homozygous for risk versus isogenic knockout or non-risk haplotypes. Sub-populations of risk haplotype cells exhibited variable morphology, proliferation, contraction, and adhesion. When sorted by adhesion, risk VSMCs parsed into synthetic and contractile sub-populations, i.e., weakly adherent and strongly adherent,

respectively. >90% of differentially expressed genes co-regulated by haplotype and adhesion were associated with Rho GTPases, i.e., contractility. Weakly adherent sub-populations expressed more short isoforms of ANRIL, and when overexpressed in knockout cells, ANRIL suppressed adhesion, contractility, and αSMA expression. These data are the first to suggest that variable lncRNA penetrance may drive mixed functional outcomes that confound pathology.

2.2 Significance

Intronic polymorphisms in the lncRNA ANRIL are associated with the highest increased risk of vascular disease. Splice variants containing a proximal termination of transcription (in exon 13) are upregulated in the presence of risk polymorphisms and cause phenotype differences in induced pluripotent stem cell-derived vascular smooth muscle cells, but with variable penetrance. By sorting cells via physical differences, we identify sub-populations within the risk haplotype that have different morphology, proliferation, contraction, and adhesion; when overexpressing ANRIL in knockout cells, the phenotype reverts. These data suggest a reason why vascular disease pathology may be variable in patients despite the elevated risk caused by this lncRNA.

2.3 Introduction

Cardiovascular diseases are the leading causes of death in the United States of which coronary artery disease (CAD) accounts for over 370,000 deaths annually[168]. Of the more than 10^6 single nucleotide polymorphisms (SNPs) in our genome[16–18], most SNPs are located in non-coding regions, making mechanisms through which they enhance disease risk enigmatic[19]. SNPs having the strongest association with CAD are found in the non-coding 9p21 locus[21,22,169], occur with significant frequency and in linkage disequilibrium in most populations, and are associated with up to 60% increased risk[21]. While prevalence and impact are now being widely studied, understanding mechanisms employed by the most common SNPs in 9p21, i.e., the "risk haplotype", has been further complicated by their presence only in higher order primates[20,170]. Mechanisms may also be cell type-specific, given that clinical presentation can vary widely and affect different cell types differently[171].

Vascular smooth muscle cells (VSMCs), which are the primary cell type in the arterial wall and regulate vascular tone[172,173], dedifferentiate and migrate into the intima in response to endothelium injury as part of plaque formation[174–176] forming the main cell type in the neointima[176,177]. The role of VSMCs in atherosclerosis has become increasingly recognized, with lineage tracing studies identifying that VSMC content in plaques has historically been underestimated and VSMCs misidentified as macrophages[176,178]. VSMCs exhibit remarkable plasticity, in which they dedifferentiate, from a quiescent, *contractile phenotype*, to a more proliferative and migratory *synthetic phenotype*[173–176,179,180]. While environmental cues–ranging from substrate stiffness[173,181–184] to soluble factors[176,179,185]–can direct VSMC phenotype, distinct VSMC sub-populations from unique developmental origins have been identified within the vessel wall and as a function of CAD[186].

Being limited typically to human models, studies examining 9p21.3 primarily have relied on population surveys, post-mortem analyses, or primary cells isolated from other organ systems; these approaches preclude actively perturbing systems to validate causal relationship. Recently, however, patient-specific induced pluripotent stem cells (iPSCs) were generated with haplotypes representing patients who are homozygous for the risk allele

(RR), homozygous non risk (NN), or whose risk allele was knocked out (RR KO)[23]. With this approach, direct sub-population comparisons, which originated from the same isogenic patient cell line, are possible and can more easily identify key pathways related to phenotypic plasticity. This approach also lends itself well to single cells analyses, which can point to specific genomic mechanisms. Here we observed phenotype heterogeneity in iPSC-derived VSMCs from patients homozygous for the risk haplotype, and via a function sort based on adhesion, we could identify populations of both synthetic and contractile sub-populations, i.e., weakly adherent and strongly adherent, respectively, within risk haplotype. Phenotype appears to be directly modulated by the presence of short isoforms (containing a proximal termination of transcription in exon 13) of the long non-coding RNA (lncRNA), *ANRIL*[187], suggesting that variable lncRNA penetrance could drive a range of functional outcomes that lead to complex pathology.

2.4 Results

2.4.1 Haplotype mediates iPSC derived VSMC phenotype with patient-specific penetrance

iPSCs were derived from patients who are homozygous for the risk allele (RR), determined by genotyping at rs1333049, rs2383207, and r10757278[23], or homozygous non risk (NN); heterozygous patients were omitted for clarity. To validate effects, isogenic TALEN edited knock out (RR KO) lines were created as well. iPSCs stained positive for pluripotency makers Nanog, Sox2, and Oct4 (**Figure 2.1A**) and were differentiated into vascular smooth muscle cells **(Figure 2.1B)** using a protocol developed by Cheung et al for VSMCs[188], specifically deriving cells from the lateral plate mesoderm[189,190] as in vivo. iPSC-

VSMCs from all haplotypes stained positive for SMC makers calponin and SM22 **(Figure 2.1C),** however there were notable morphological differences comparing haplotypes, with both RRWT patient lines significantly smaller than the NN and RRKO lines as well as between RRWT patient lines **(Figure 2.1C-D)**. Given the critical role that adhesion complexes play in cell spreading and morphology, we assessed integrin transcript differences via hierarchal clustering of bulk-RNA sequencing data from multiple patient and clonal lines from each haplotype[23]. RRWT patients (red color-coded columns) clustered together and exhibited deficits in fibronectin and collagen binding integrins, as shown by the extracellular matrix (ECM) binding partners color coded in rows **(Figure 2.1E)**. To determine if such deficits in RRWT patients resulted in functional deficits, cell adhesion strength to collagen, which is the primary ECM constituent of the tunica media[191,192], was investigated using a spinning disk assay **(Supplemental Figure 2.1)**. Comparing the shear stress value at which 50% of the population detached, i.e., τ_{50}, VSMCs derived from both RR patient lines were lower than both the NN and RRKO, indicating reduced adhesion strength **(Figure 2.1F)**. These morphological, transcriptomic and adhesion strength differences across haplotypes suggest that haplotype-specific changes VSMC phenotype might be impact function and CAD progression, i.e., VSMC dedifferentiation from contractile to synthetic phenotype[173–176,179,180]. However, phenotype plasticity may not be universally penetrant, so we next employed single cell assays to sort cells into distinct phenotypic populations, i.e., strongly adherent, contractile cells versus proliferative, synthetic cells.

Figure 2.1. iPSC-VSMC phenotype is haplotype-mediated but has patient-specific penetrance depending on Integrins: (A) Staining of patient-derived iPSCs for self-renewal markers Nanog (red), Sox2 (green), and Oct4 (white) as well as nuclei (blue). Scale bar is 500 µm. **(B)** Schematic of differentiation process based on Cheung et al.[188] The timeline illustrates conditions, timing, and growth factors required. **(C)** iPSC derived VSMCs from the indicated patient or clone with haplotype indicated by color were stained for Calponin and SM22 expression. Scale bar is 100 µm. **(D)** Cell area for the same haplotypes. N=1229, 1286, 130, and 295 for RR P1, RR P2, NN, and RR KO, respectively. **(E)** Heatmap of integrin expression for VSMCs from the indicated haplotypes, noting their extracellular matrix binding partner (at right). Hierarchical clustering of bulk RNA-seq data[23] using Euclidean distance was performed on both genes and patient samples with haplotype indicated by color; data was scaled within rows. **(F)** Adhesion strength, measured as the shear stress required to detach 50% of the population, i.e., τ 50 (measured in dynes/cm2) using a spinning disk assay, is plotted for the indicated haplotypes. N=10,11,7 and 8 for RR Patient1, RR Patient 2, NN and KO of RR Patient 1, respectively. **(G**) Cells from the same haplotypes were also characterized for their percent detachment at 90 dynes/cm2 using a microfluidic device. N= 4, 15, 4, and 4 for RR Patient1, RR Patient 2, NN and KO of RR Patient 1, respectively. *p<0.05, **p<10-2, ***p<10-3, and ****p<10-4 for one-way ANOVA with Tukey multiple comparison test.

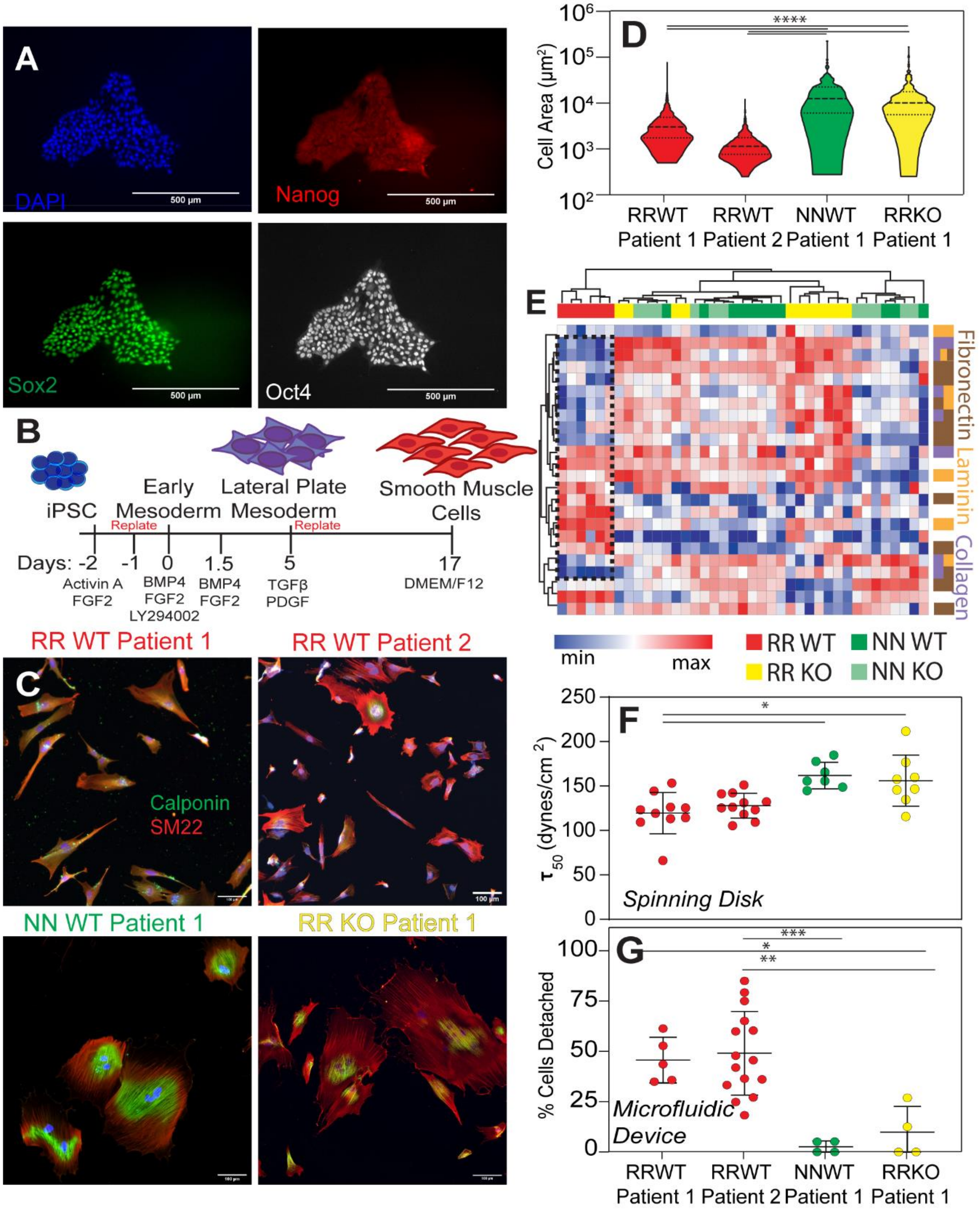
A
DAPI
500 µm
Nanog
500 µm
Sox2
500 µm
Oct4
500 µm
B
iPSC
Early Mesoderm
Lateral Plate Mesoderm
Smooth Muscle Cells
Replate
Replate
Days: -2
-1
0
1.5
5
17
Activin A FGF2
BMP4 FGF2 LY294002
BMP4 FGF2
TGFβ PDGF
DMEM/F12
RR WT Patient 1
RR WT Patient 2
C
Calponin
SM22
100 µm
NN WT Patient 1
RR KO Patient 1
D
10^6
10^5
10^4
10^3
10^2
Cell Area (μm^2)
****
RRWT Patient 1
RRWT Patient 2
NNWT Patient 1
RRKO Patient 1
E
Fibronectin
Laminin
Collagen
min
max
RR WT
NN WT
RR KO
NN KO
F
250
200
150
100
50
0
τ_{50} (dynes/cm^2)
*
Spinning Disk
G
100
75
50
25
0
% Cells Detached
***
*
**
Microfluidic Device
RRWT Patient 1
RRWT Patient 2
NNWT Patient 1
RRKO Patient 1

2.4.2 Patient-specific adhesion sorting creates heterogenous but morphologically distinct VSMC subpopulations

Adhesion sorting was achieved by placing cells in a microfluidic device that exposed cells to acute, uniform fluidic shear stress and collected those cells that detached, i.e., the weakly adherent population (WA), relative to the population that remained adherent, i.e., the strongly adherent population (SA) **(Supplemental Figure 2.2).** The population fraction that detached was measured from device flowthrough at a shear stress of 90 dynes/cm^2, which is just below the τ_{50} for the risk haplotype. A greater percentage of cells detached for both RRWT patient lines compared to both NN and RRKO **(Figure 2.1F)**, confirming adhesion deficits in RRWT VSMCs are captured by both systems, whether population or single cell based.

To understand what cell phenotype(s) composed each population, we collected and analyzed the WA and SA populations for each haplotype at 90 dynes/cm^2. As expected, RRWT patient lines had a greater percentage of WA cells than their NN or RRKO counterparts **(Figure 2.2A inset)**. WA cells were smaller and more circular than their SA counterparts for most haplotypes **(Figure 2.2A-B)**, i.e., at this shear, this population was generally smaller than the average cell area of 3222 μm^2 (>90% of the population when it exists) with a shift to high circularity values. Smaller, more circular cells are indicative of a synthetic phenotype[179,193], suggesting that the microfluidic device could be used to sort cells into disease relevant subpopulations. Conversely, SA cells are larger on average larger and less circular for both RR patient lines, but the SA population for RRWT Patient 1 has considerable overlap with the WA population, with only 65% of the WA smaller than the average cell area for the line compared to 96% for RRWT Patient 2 **(Figure 2.2)**. These data suggest that there could be patient-specific sorting parameters.

To sort a more distinct WA population, we adjusted the sort parameters to be more selective for WA cells by reducing shear stress to 30 dynes/cm^2. With a smaller WA population (31% of cells; **Figure 2.2C, inset**), 96% of the population was smaller than the 3222 μm^2 average unsorted cell area **(Figure 2.2C)**, suggesting that by using patient specific parameters, adhesion strength can sort VSMCs into morphologically distinct subpopulations that are suggestive of synthetic and contractile populations. VSMCs have been shown to become more synthetic over time while in culture[194], hence we determined whether time in culture would impact sorting. Over ten cell passages, we noted that–while there were batch effects–there was no trend linking increasing culture time to a population shift to smaller, more circular cells for either RRWT patient line **(Supplemental Figure 2.3)**. While all subsequent experiments were performed using VSMCs having fewer than 10 passages, these data overall suggest that the RRWT lines have greater adhesive phenotype heterogeneity and a greater presence of weakly adherent cells.

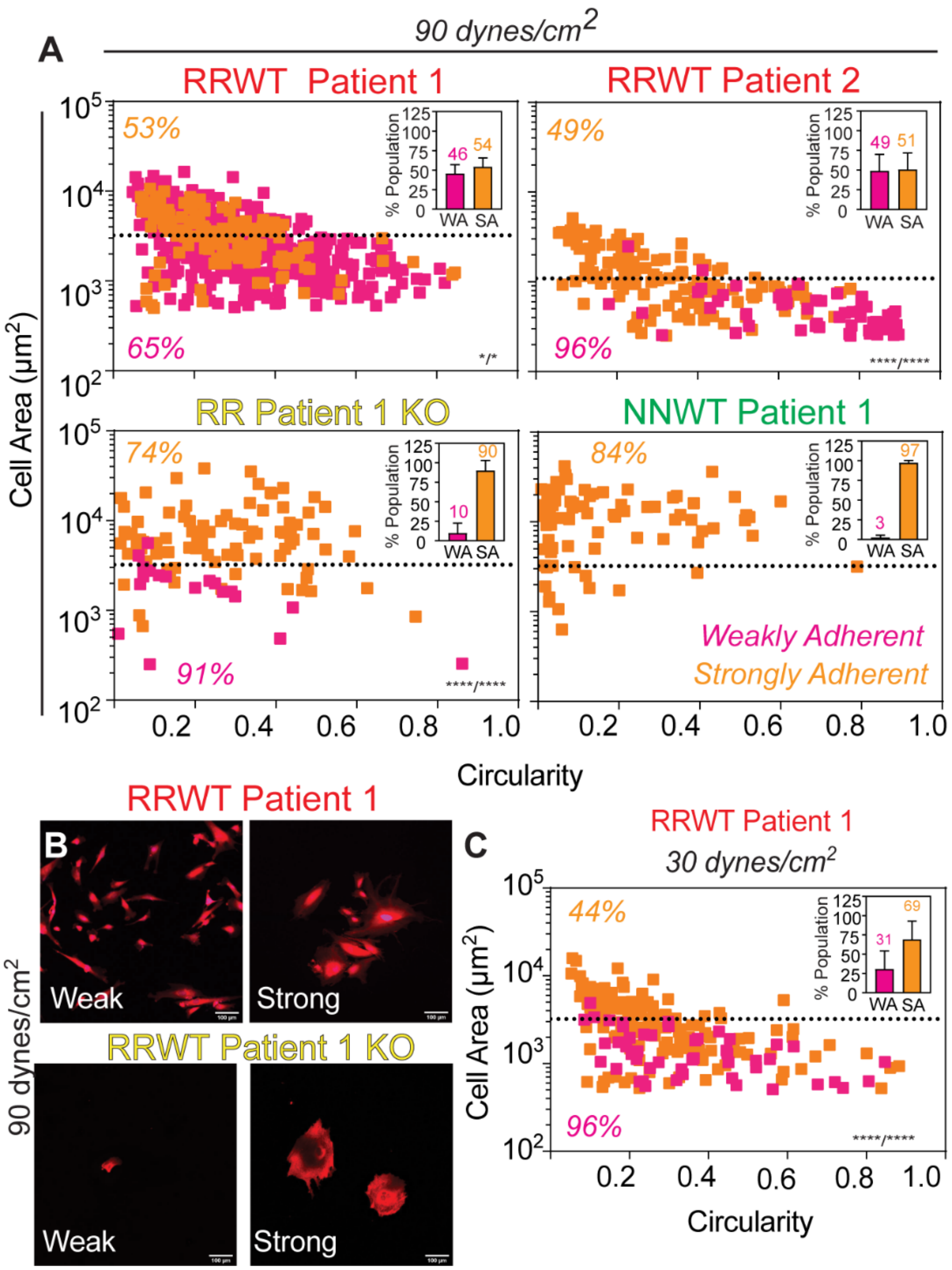

Figure 2.2. Haplotype- and patient-specific shear-based sorting stratifies VSMC phenotype: (A) Post-sort at 90 dynes/cm2, cell area and circularity measurements were plotted for weakly adherent (WA; pink) and strongly adherent (SA; orange) populations of the indicated haplotypes (text color coded from Fig. 1). The inset bar graphs show the percentage of the population that each adhesion fraction constitutes, averaged across multiple sorts. Within the scatter plots, percentages are shown to indicate the amount of data above or below the dashed line for SA and WA cells, respectively. Note the dashed line represents average cell area for each haplotype. For WA cells, N=504, 57, 22 and 0 for RRWT P1, RRWT P2, RRKO P1 and NNWT, respectively. For SA, N=140, 127, 57, and 77 for RRWT P1, RRWT P2, RRKO P1 and NNWT respectively. **(B)** Images of sorted iPSC-VSMCs (weak or strong) stained by a membrane dye. Scale bar is 100 µm. **(C)** RRWT P1 was sorted at 30 dynes/cm2, and area and circularity plotted and consistent with weaker adhesion from Fig. 1F-G. Note that a higher percentage of WA cells are now below the dashed line because of sorting at the lower, more selective shear stress. N=49 and 149 for WA and SA, respectively. *p<0.05 and ****p<10-4 for two-way ANOVA comparing haplotype area and circularity between WA and SA, with interaction and column factor comparisons, respectively.

2.4.3 Adhesion sorted cells exhibit functional differences

Having established patient-specific parameters that can separate morphologically distinct subpopulations, we next investigated whether sorted cells also exhibited functional characteristics aligned with synthetic and contractile phenotypes. Pre-sort RRWT cells are less contractile than the NN and RRKO lines **(Supplemental Figure 2.4A)** by traction force microscopy (TFM), but after sorting RRWT patient 1 (using the patient-specific shear stress of 30 dynes/cm^2), the WA sub-population was also less contractile than SA and unsorted control (US) sub-populations **(Figure 2.3A-B)**; substrate stiffness can influence VSMC contractility[173,181,183,184], but even on a 5-fold stiffer substrate, WA cells exert less strain energy compared to SA and US cells **(Supplemental Figure 2.4B)**. Concurrently, alpha Smooth Muscle Actin (αSMA) is increased in the contractile phenotype[173,179,185], hence αSMA comparisons across haplotype showed decreased expression in RRWT patient lines compared to NN and RRKO lines for the population **(Supplemental Figure 2.4C-D)** as well as single cells **(Supplemental Figure 2.4E)**. Post-sort however, αSMA expression in the WA cell fraction of RRWT patient 1 was significantly less than SA or US control populations **(Figure 2.3C-D)**. Finally, RR patient lines proliferated significantly faster than their NN and RRKO counterparts **(Supplemental Figure 2.4F)**, which together suggest a greater prevalence of the synthetic phenotype in RRWT patients that can be sorted by adhesion.

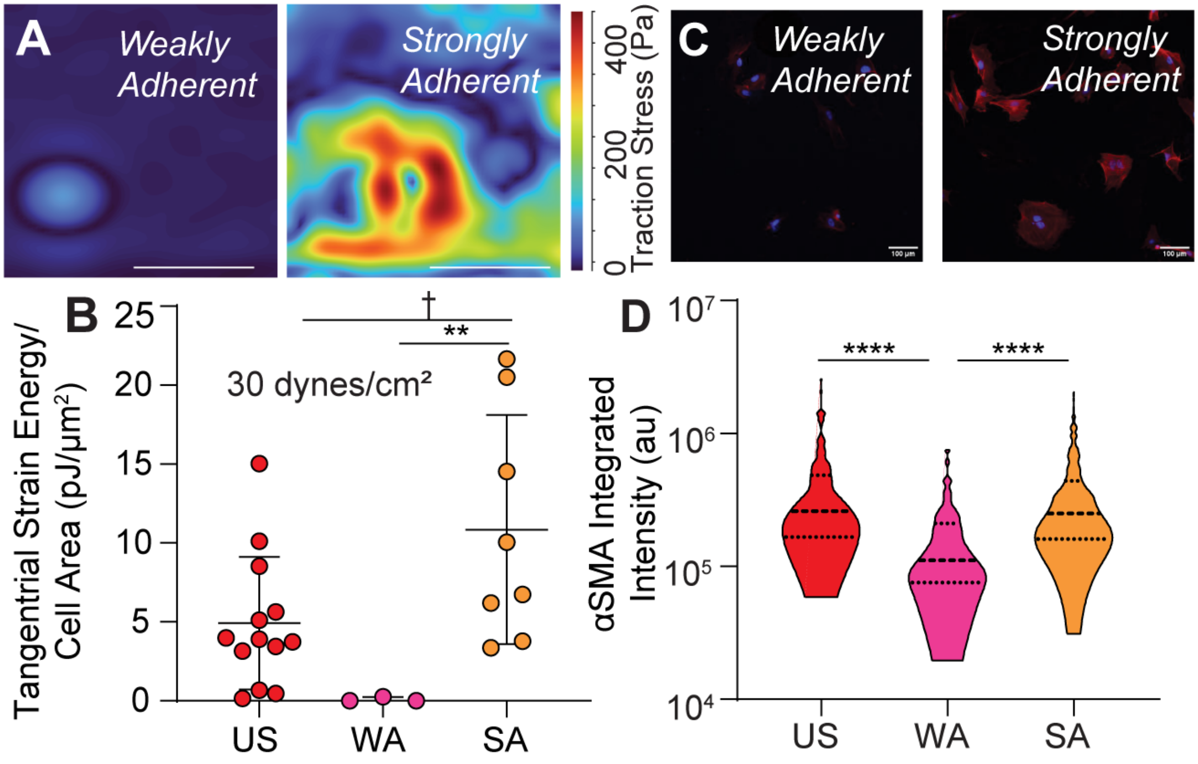

Figure. 2.3. RRWWT Patient 1 Weakly Adherent (WA) subpopulations exhibit reduced contractility and reduced contractile phenotype marker expression: (A) Heatmap displaying traction forces for a single cell measurement from traction force microscopy (TFM) performed on RRWT Patient 1 VSMCs sorted at 30 dynes/cm2, representative of the WA and SA populations. Scale bar is 50 µm. **(B)** Tangential strain energy normalized to cell area plotted for WA, SA, and unsorted (US) from RRWT Patient 1. N=13, 3, and 8 for US, WA, and SA, respectively. **p<10-2 and †p=0.107 for one-way ANOVA with Kruskal-Wallis multiple comparison test. **(C)** Immunofluorescence staining of Alpha Smooth Muscle Actin (αSMA) and DAPI for the sorted populations from RRWT Patient 1. Scale bar is 100 µm. (D) αSMA expression was measured using immunofluorescence staining and measuring the integrated intensity for individual cells (au). N= 137, 114 and 294 for US, WA, and SA respectively. **p<10-2 and ****p<10-4 for one-way ANOVA with Tukey's multiple comparison test.

2.4.4 Differentially Expressed Genes are both Disease Relevant and Co-regulated by Haplotype and Adhesion

Underlying functional differences, we sought to understand transcriptional differences resulting from the risk haplotype and adhesion. Bulk-RNA sequencing was performed on the sorted and unsorted populations from RRWT and RRKO Patient 1 using multiple passages and differentiation batches. Mapped sequence run counts were used to generate a Pearson correlation heat map for unsorted samples, which resulted in RRWT and

RRKO samples from Patient 1 to group together based on similarity in whole transcriptome (**Supplemental Figure 2.5A**). 3D Principal component analyses (PCA) of the unsorted RRWT and RRKO transcriptome, including similar VSMC data from Lo Sardo et al[23], showed clustering by haplotype, irrespective of batch, culture time, or data source (**Supplemental Fig 2.5B**). Similarly, when clustering by adhesion strength and using culture time as a co-variant, 3D PCA plots show divergence of sorted cells from unsorted RRWT parental cells in opposite directions; centroids for WA and SA cells show noticeable differences in PC1 and PC3 **(Figure 2.4A)**. However, within the transcriptomes of the WA and SA cell populations, we found 2206 differentially expressed genes (DEGs)–defined as a p-adj. value less than 0.05 **(Figure 2.4B).** Using PANTHER to assess gene ontology (GO) enrichment for molecular function (MF) terms, several of the top 30 GO terms mapped to relevant concepts with CAD, adhesion, and the cytoskeleton **(Figure 2.4C)**. Using the same approach with haplotype comparisons, we found 693 DEGs between RRWT and RRKO, and of those, 154 DEGs were common to sorted cell comparisons **(Figure 2.4D)** for which we mapped GO terms from PANTHER. Fold change for adhesion (x) and haplotype (y) were plotted against each other to determine co-regulation, and we found that >90% of DEGs were co-regulated with 67% being both upregulated **(Figure 2.4E).** Mapping the most common ontological term associated with each DEG, the most commonly co-regulated genes with GO terms included regulation of cell adhesion, microtubule processing, circulatory-system development, and cytoskeleton organization **(Figure 2.4E).**

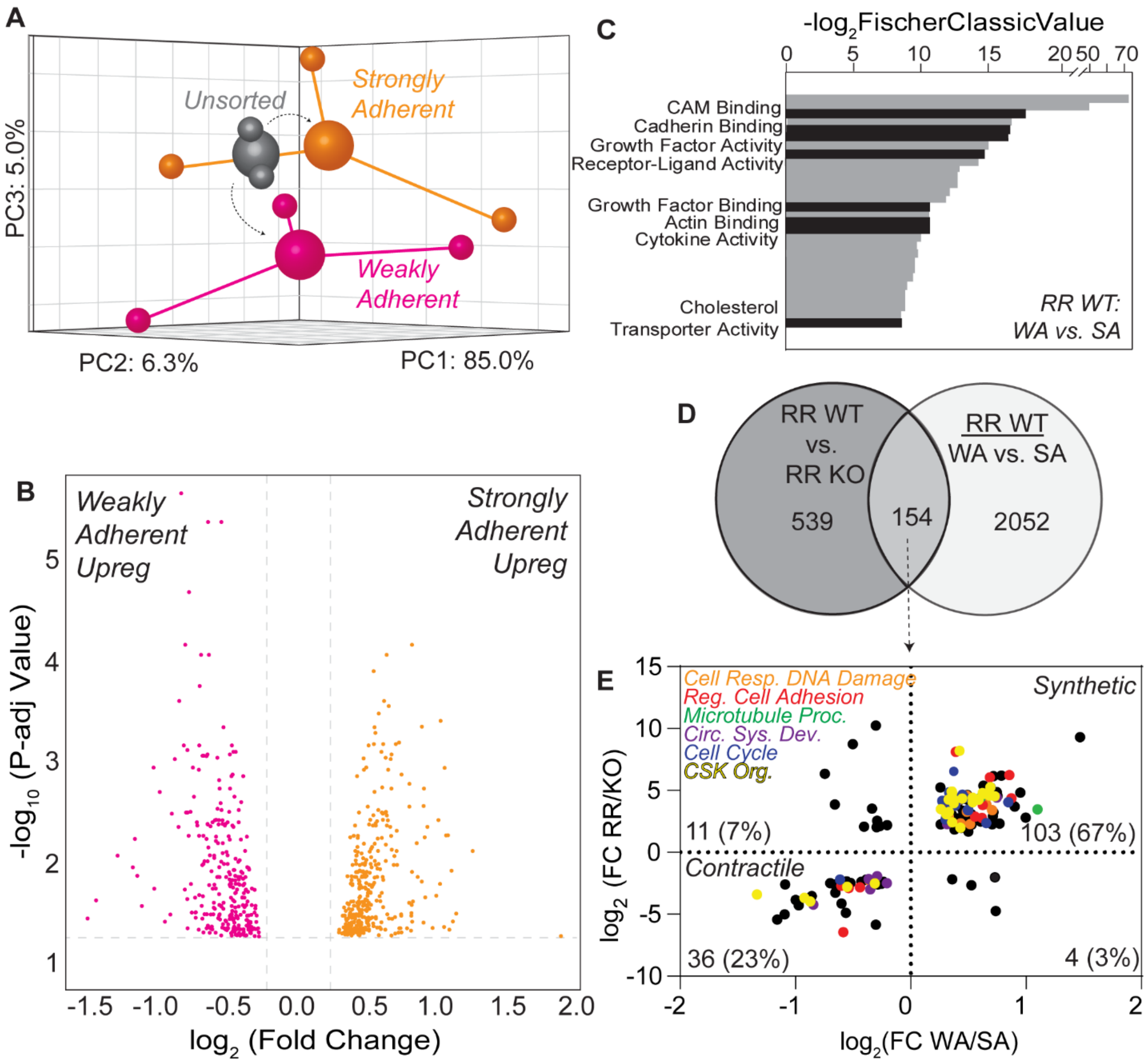

Figure 2.4. RNA Sequencing of sorted populations reveals differentially expressed genes (DEGs) that are co-regulated between haplotype and adhesion: (A) RNA sequencing of RRWT Patient 1 VSMC sorted populations was performed and principal component analysis (PCA) was plotted in 3D, with the centroids for each condition shown in the color of each respective population (US, WA, SA). **(B)** Volcano plot of the 2206 DEGs between WA and SA, defined as genes with p-adj<0.05.**(C)** The top 30 ontological terms associated with the DEGs in (B) including molecular function terms, plotted using –log2 (Fischer Classic Value) and highlighting terms of interest in gray. **(D)** Venn Diagram of DEGs for WA versus SA (light gray) and RRWT versus RRKO (dark gray), highlighting the 154 genes differentially expressed between both group comparisons. **(E)** DEGs common between both WA versus SA and RRWT versus RRKO were plotted based on the fold change for each comparison, such that DEGs that were overexpressed in WA versus SA as well as RRWT versus RRKO were plotted in the top right quadrant (67%) and those that were overexpressed in SA versus WA and RRWT versus RRKO were plotted in the bottom left quadrant (23%). Percentage of the 154 common DEGs in each quadrant is shown, with 90% of the common DEGs co-regulated color coded by associated ontological terms.

2.4.5 WA populations have reduced Signaling by Rho Family GTPases and are Driven by Short Isoforms of lncRNA ANRIL

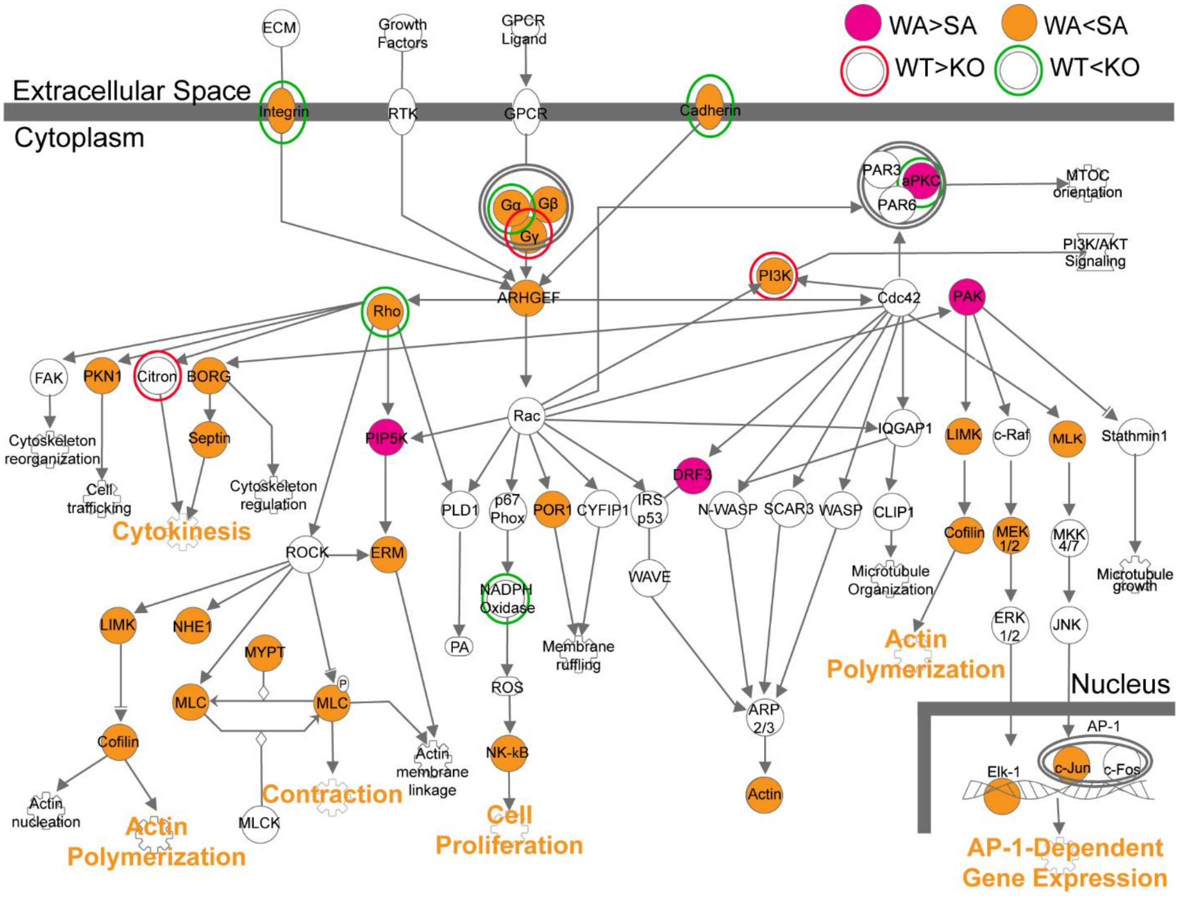

Figure 2.5. Ingenuity Pathway Analysis reveals the Weakly Adherent population has reduced RhoA signaling: Ingenuity Pathway Analysis of the genes differentially expressed between WA and SA as well as DEGs between RRWT and RRKO identified signaling by RhoA family GTPases as a top pathway. Genes overexpressed in WA compared to SA are filled with pink, whereas those overexpressed in SA are filled with orange. Those overexpressed in RRWT are circled in red, whereas those overexpressed in RRKO are circled in green**.**

To identify gene pathways differentially regulated by VSMC adhesion, ingenuity pathway analysis was performed on adhesion and haplotype DEGs. Signaling by RhoA family GTPases was a top pathway match for adhesion (p-value<1x10^{-5}) and haplotype ($p<0.05$) **(Figure 2.5)**. 31 adhesion DEGs and 8 haplotype DEGs mapped to the pathway, and of those, the majority showed downregulation, i.e., negative z-scores, in weakly adherent and risk haplotype-containing VSMCs. Most of these WA and/or RRWT DEGs associated with actin polymerization, contraction, proliferation, cytokinesis, and AP-1 gene dependent expression, consistent with prior GO terms, decreased adhesion, contractility, and lower αSMA expression. Data are also consistent with possibility that WA cells are more synthetic than SA cells, with increased prevalence of WA cells in RRWT patients.

To investigate how SNPs at 9p21 could regulate RhoA signaling and result in an increased WA cell fraction, expression of ANRIL–the lncRNA which overlaps with the 9p21 locus–was measured. ANRIL is subject to post transcriptional splicing resulting in multiple isoforms, including short isoforms spanning exons 6,7 and a longer isoform spanning that includes exons 19 and 20 (**Supplemental Figure 2.6**). Short isoforms of ANRIL 6,7 were previously reported to be higher in RRWT VSMCs compared to NNWT and RRKO [23]. Long ANRIL 19,20 (annotated as ANRIL 18,19 in Lo Sardo et al) was not detected in the RRKO, consistent with the location of TALEN mediated deletion and location of primer binding. Long ANRIL was higher in NNWT whereas short ANRIL was higher in RRWT (**Supplemental Figure 2.7**), suggesting that short ANRIL–but not long ANRIL–drive the RRWT phenotype. To further determine if ANRIL expression was driving phenotypic heterogeneity within RRWT VSMCs, we compared expression of sorted RRWT populations. For RRWT Patient 1, WA cells expressed more short ANRIL compared to both the SA and US cells but did not differentially expression long isoforms (**Figure 2.6A**), again suggesting that short isoforms, containing exons 6,7 but not 19, 20, are responsible for the VSMC phenotype change. Only isoforms A2, A3, A11 and A12 have been measured in iPSC-VSMCs[23] and of those, only isoforms A2 and A3 contain exons 19,20. Hence we deduced that either A11 or A12 were likely the isoforms differentially expressed between WA and SA cells as in addition the difference between RRWT and RRKO.

Figure 2.6. Overexpression of Short Isoforms of lncRNA ANRIL restores phenotypic heterogeneity of RR VSMCs: (A) Expression of the lncRNA ANRIL in the sorted populations (WA, SA) and unsorted (US) for RRWT Patient 1 was plotted after normalization to housekeeping gene PPIA and the average expression of cells seeded in the device but not exposed to shear stress (to account for phenotype changes from sorting). Short isoforms were measured using primers binding exons 6,7, (left; N = 9, 9, and 10 for US, WA and SA, respectively) and long isoforms were measured using primers binding exons 19, 20 (right; N=7, 10, and 7 for US, WA, and SA, respectively). **p<10-2 and †p≥.05 for one-way ANOVA with Tukey's multiple comparison test. **(B)** RRKO VSMCs overexpressing A11 (left) and A12 (right) were exposed to 90 dynes/cm^2 of shear stress, with post-sort morphology of the WA (pink) and SA (orange) populations plotted. The inset bar graphs show the percentage of the population that each adhesion fraction constitutes, averaged across multiple sorts. Note the dashed lines represents average cell area or circularity for each respective total population. Percentages shown indicate the amount of data above or below (left value) or to the right or left (right value) of the dashed lines for SA and WA cells. For A11 overexpressing cells, N = 76 and 297 for WA and SA, respectively. For A12 overexpressing, N=70 and 242 for WA and SA, respectively. **p<10-2 and ****p<10-4 two-way ANOVA comparing haplotype area and circularity between WA and SA, with interaction and column factor comparisons, respectively. **(C)** αSMA expression was measured using immunofluorescence staining and measuring the integrated intensity for individual cells (au). N = 342, 454, 76, and 297 for null control of RR KO, A11 overexpressing US, WA A11 overexpressing and SA A11 overexpressing, respectively. N = 343, 338, 70 and 242 for null control of RR KO, A12 overexpressing US, WA A12 overexpressing and SA A12 overexpressing, respectively. *p<0.05, ***p<10-3 and ****p<10-4 for one-way ANOVA with Tukey's multiple comparison test. **(D)** Tangential strain energy, normalized to cell area, was plotted for WA, SA, and unsorted (US) populations from RRKO VSMCs overexpressing A11 (left) and A12 (right) and RR KO controls. N= 20, 13, 7, and 8 for RRKO null control, A11 overexpressing US, WA and SA, respectively, and N = 12, 9, and 13 for A12 overexpressing US, WA, and SA, respectively. *p<0.05, **p<10-2 ***p<10-3 for one-way ANOVA with Kruskal-Wallis multiple comparison's test**.**

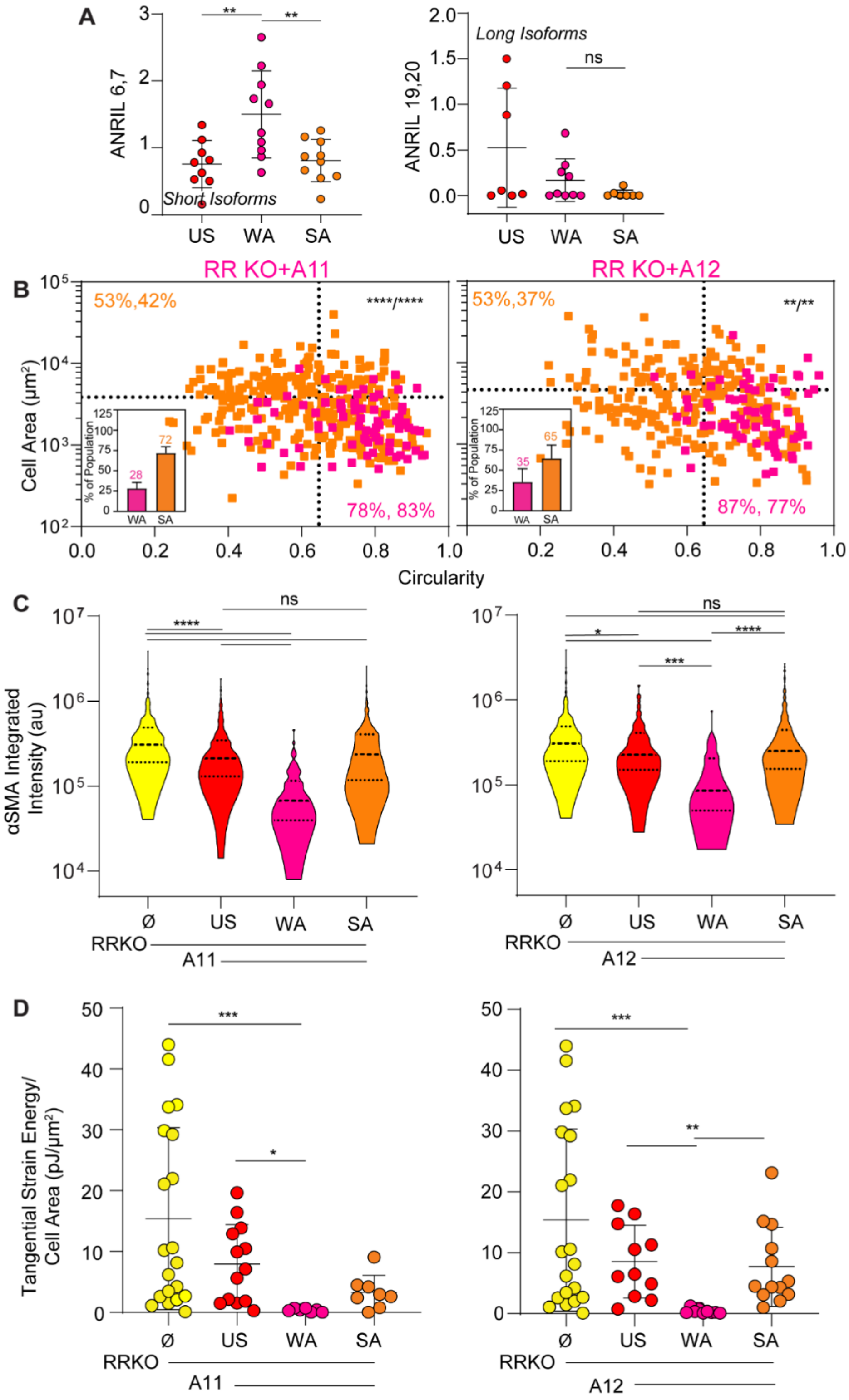
A
ANRIL 6,7
Short Isoforms
**
**
US
WA
SA
ANRIL 19,20
Long Isoforms
ns
US
WA
SA
B
RR KO+A11
RR KO+A12
Cell Area (μm²)
53%,42%
****/****
78%, 83%
53%,37%
/
87%, 77%
% of Population
28
72
35
65
WA
SA
Circularity
C
αSMA Integrated Intensity (au)
****
ns
*
***
****
Ø
US
WA
SA
RRKO
A11
A12
D
Tangential Strain Energy/ Cell Area (pJ/μm²)
***
*
**
Ø
US
WA
SA
RRKO
A11
A12

To determine whether the short isoforms of ANRIL, e.g., A11 or A12, were causative–and not just correlative–of phenotype plasticity, we used a lentivirus to deliver A11 and A12 to RRKO VSMCs that lack SNPs to determine if it could induce a RRWT-like phenotype (**Supplemental Figure 2.8A**). Across multiple differentiations and viral batches, we found that adding back A11 and A12 in a dose-dependent manner scaled directly with short ANRIL expression; rtTA and doxycycline alone–without the presence of A11 or A12 plasmids–did not increase short ANRIL expression (**Supplemental Figure .28B-C**). Using the lowest dosage to most closely mimic short ANRIL expression levels from RRWT, we compared RRKO cells overexpressing A11 or A12, i.e., "RRKO+A11" and "RRKO+A12", to parental cells in morphology and αSMA expression. Both RRKO+A11 and RRKO+ A12 were smaller and had reduced expression of αSMA compared to RRKO (**Supplemental Figure 2.8D-E**) as a direct result of the overexpression and not doxycycline treatment (**Supplemental Figure 2.8F-G**).

In addition to size and marker expression, we sorted cells by adhesion strength to determine if A11 and A12 shifted populations; at 90 dynes/cm^2 shear stress, a greater percentage of WA cells in RRKO patient 1 expressing A11 or A12 detached compared to RRKO cells cultured with or without doxycycline (**Figure 2.6B, Supplemental Figure 2.9A**). WA cells were smaller and more circular (**Figure 2.6B**), had reduced expression of αSMA (**Figure 2.6C**), and were less contractile (**Figure 2.6D**) than their SA counterparts for both RRKO+A11 and RRKO+A12, which together indicate a more synthetic phenotype. The WA were also less contractile than the SA and US controls, as measured by TFM for multiple sorts, differentiation and infection batches of RR KO+A11 and RR KO+A12 (**Figure 2.6D**), further indicating WA cells made up a more synthetic phenotype while SA cells were a more contractile phenotype. Notably, culturing cells in doxycycline without A11 or A12 did not decrease cell contractility or adhesion (**Supplemental Figure 2.9B**).

2.5 Discussion

Genome wide association studies have identified many disease-related SNPs, however, since many occur in non-coding loci, the mechanism(s) through which those enhance disease remains relatively unclear[16,18,195]. SNPs at the 9p21 locus have the highest odds ratio for CAD, yet how they result in disease remains poorly understood[20–22,196], partly due to the inadequacy of animal models, the polymorphisms occurring in linkage disequilibrium[197], overlapping risk regulators[19,198], and the potential for bulk measurements masking important biology[199]. Vascular smooth muscle cells (VSMCs), which account for the majority of cells within the fibrous cap[178], are an important cell type in atherosclerosis. As illustrated here, we used a genome editing strategy to isogenically assess variants in patient specific, iPSC derived VSMCs and a microfluidic approach to sort heterogenous VSMCs into disease relevant phenotypes. The risk haplotype increased the presence of a less adherent, less contractile phenotype within a VSMC population, but phenotype penetrance was variable; heterogenous expression of a lncRNA, which could potentially exacerbate CAD and was especially apparent when populations were sorted, could drive the variability that we observed in the lines across and within patients. Although we focused specifically on the 9p21 locus, the majority of disease associated SNPs are in non-coding loci, and thus it is important to recognize that some of the heterogeneity observed in disease progression[200–202] could be due to this. We believe that our findings are supportive of a general approach to exploring mechanisms by which non-coding loci enhance risk for disease and in which cellular heterogeneity is a hallmark.

It is becoming widely recognized that transcriptional differences exist even in established culture models, immortalized cell lines, or isogenic populations, and this can lead to variations in phenotype and disease penetrance. Biological markers can sort cells by function[203] but are best when used in combination[204]. Here even using a gene-edited, iPSC-based system to recapitulate disease phenotypes, we noted increased heterogeneity in morphology and cellular adhesion in the risk haplotypes consistent with variable penetrance *in vivo*[205]. Unlike conventional biomarkers, our approach with a microfluidic device enables one to perform a functional sort of cells based on their adhesion strength to ECM. While adhesion sorting is not novel, it has primarily been used to study cancer[34] or sort rare populations from blood, such as circulating tumor cells [44,206,207] or stem cells[208]. Many diseases, including CAD, progress through the development of divergent behaviors within a cell type[200–202,209], thus application of biophysical sorting has the potential to unveil key insights where other methods cannot. For example, we found that adhesion-based sorting of VSMCs allowed us to isolate subpopulations of weakly adherent, more synthetic and strongly adherent, more contractile phenotypes and directly compare them to better assess phenotype plasticity. Many studies have assessed causes of VSMC plasticity[173,179,181–184], but sorting VSMCs also allowed us to establish causative links to RNA-based mechanisms and correlate them to CAD. These data also established patient-to-patient variance as well, both in phenotype plasticity and sensitivity, which is perhaps less surprising given variability in patient derived iPSC models[210].

Not only did WA cells exhibit reduced area and increased circularity, which are morphological characteristics of synthetic VSMCs[179], but they were also less contractile than SA cells. While reduced contractility may be expected for weakly adherent cells, the correlation is not implied; previous studies of epithelial breast, prostate, and lung cancer cells did not find such a relationship[34], suggesting a cell type specific relationship in addition to patient-to-patient variance. Other factors, e.g., morphology, height and shape, membrane rheology, and focal adhesion complex turnover rate, play a role in determining a cell's adhesion strength[211] and therefore, VSMC sorting into more and less contractile populations using adhesion strength was non-trivial. Because substrate stiffness has been shown to influence VSMC phenotype plasticity and contractility[173,181–183], we additionally performed TFM using hydrogels of greater stiffness and found the WA are less contractile than SA, independent of substrate stiffness. Such trends are similar to epithelial cells[34], hence further verification for each cell type is implied by our data contrasted with others.

As noted above, cellular heterogeneity appears linked to natural variance in lncRNA expression for ANRIL even within the same patient and haplotype, i.e., variance was observed in both short and long ANRIL isoforms; while mechanical effects via adhesion differences naturally varied in the parent populations, especially for RRWT cells, it was surprising that similar variance was observed in RRKO cells expressing A11 or A12. While virus copy number and batch effects could certainly vary between cells and data points, respectively, variance up to an order of magnitude was surprising especially when considering that RRKO cells themselves exhibited almost no variance. Although unrelated to adhesion, similar lncRNA heterogeneity in cancer can be found in and between tumors[212] and can be a predictor distant metastasis[213]; opposing adhesive behavior in epithelial carcinomas[34] versus vascular smooth muscle may also suggest that their regulation is from heterogeneous lncRNA expression. For vascular cells specifically, association studies have implicated a number of loci containing lncRNAs[21,22,169] to disease, with strongest association and functional regulation of VSMCs[23] found in 9p21. While here we link function to adhesion and heterogenous expression of ANRIL, we were unable to find similar heterogenous lncRNA regulation of vascular cells, independent of mechanics. Despite that, numerous examples exist describing lncRNAs and VSMC adhesion; the lncRNA PAXIP1-AS1 has been associated with the synthetic phenotype and reduced adhesion as observed in idiopathic pulmonary arterial hypertension[214]. Conversely, the lncRNA VINAS regulates cell-cell adhesion in endothelial cells, and its silencing decreased expression of leukocyte adhesion molecules and impaired the ability of those cells to bind to the endothelium[215]. While heterogeneity is not described explicitly in these systems, variance in lncRNA expression may still be present in the disease context, and our data suggests that such exploration may be warranted.

Finally it is important to put these data in the appropriate disease context. The transcriptomic variance we observed suggest that ANRIL may have more genome wide roles than regulating CDNK2A and CDNK2B as previously implied, and there are likely many more isoform-specific tasks than indicated here, e.g., alternatively spliced transcripts are attributed to opposing effects in endothelial cells during atherosclerosis[216]. It is also not clear how SNPs drive lncRNA alternative splicing, and what causes differential expression within an isogenic VSMC population. Regardless, patients with the 9p21 risk haplotype have an overabundance of VSMCs in their atherosclerotic lesions[205], and our data here suggests that this could be due to heterogenous phenotypic switching as a result of variable short ANRIL expression, leading to more synthetic, weakly adherent cells that heighten the risk for atherosclerotic disease.

2.6 Methods

2.6.1 Ethical Compliance and Cell Lines

The authors have complied with all ethical regulations. Human subjects were enrolled and informed consent obtained under a study approved by the Scripps IRB (#115676) and cells were transferred and maintained under a study approved by UCSD IRB (#141315). The lines included in this study were from three patients: C151 (NN; clone WF9), C512 (RR WT clones 1-5 and 2-3 and isogenic RR KO clones 1-9 and WB46), and C021 (RR WT clone ED2-70 and isogenic RR KO clone ED2-65). Isogenic KO lines were derived by TALEN-mediated genome editing as previously described.

2.6.2 iPSC Maintenance and Smooth Muscle Cell Differentiation

iPSCs were cultured on Matrigel (Biolegend) coated 6 well plates in mTSER stem cell culture media (Stem Cell Technologies) with media changed daily and cells passaged using Versene (Thermo Fisher) and a cell scraper. To induce differentiation, a previously established SMC differentiation protocol[188] was followed, specifically the method for deriving SMCs from the intermediate lateral plate mesoderm. One day prior to passaging, “Day -2, when colonies were modestly sized (70% confluency,) media was changed to chemically defined media , “CDM” with 5mg/ml Bovine Serum Albumin, Fraction V (BSA-Calbiochem), 12ng FGF2 (Proteintech Group) and 10ng/ml Activin A (Biolegend). CDM media consisted of 1:1 IMDM [+ L-Glutamine +25mM HEPES] (Thermo Fisher): F12 [Ham Nutrient Mix + L-glutamine] (Thermo Fisher) 1% (v/v) chemically defined lipid concentrate (Thermo Fisher), 0.015 mg/ml Transferrin (Athens Research and Technology), 0.007mg/ml insulin (Kerafast), .004% (v/v) monothioglycerol (Sigma Aldrich). The following day, ‘Day -1”, cells were passaged using Versene onto 0.1% (w/v) gelatin (Porcine, Type A-Sigma) coated plates into 1mg/ml Poly(vinyl alcohol) (Sigma Aldrich) CDM, “CDM PVA” and 12ng/ml FGF2 and 10ng/ml Activin A. On “Day 0”, cells were inducted into the mesoderm by changing media to CDM PVA with 20ng/ml FGF2, 10uM LY294002 (LC Laboratories), and 10ng/ml BMP4 (Humanzyme). 36 hours later, on “Day 1.5”, media was changed to CDM PVA with 20ng/ml FGF2 and 50ng/ml BMP4. 48 hours later, “Day 3.5’, half of the media was replaced. 36 hours later, on “Day 5” cells were split onto new gelatin coated wells, at 190,000 cells/well, using TrypleE (Thermo Fisher), and resuspending in “Day 5” media, which constituted of CDM PVA with 10ng/ml PDGF (Biolegend) and 2ng/ml TGF-β (Biolegend). 24 hours later, media was changed with “Day 5” media and for the next 12 days media was changed every two to three days using the same. When cells became confluent, they were split 1:3 using TrypleE and the same “Day 5” media. On day 18, the differentiation was complete, and media was changed to DMEM/F12 (Thermo Fisher) with 10% (v/v) Fetal Bovine Serum (FBS- Gemini Bio-Products) 1% (v/v) Penicillin Streptomycin (Gemini Bio-Procuts) and .2% (v/v) MEM Non-Essential Amino Acid Concentrate 100x (Thermo Fisher). VSMCs were cultured as such, changing media every two to three days and passaged using TrypleE 1:3 at least once before any experiments were performed or cells were frozen down for storage in liquid nitrogen (using the described DMEM/F12 media with 10% Dimethyl Sulfoxide (DMSO-Sigma Aldrich).

2.6.3 Microfluidic Device Channel Design and COMSOL Simulation

Microfluidic device channels were designed in AutoCad, which was printed onto PET film transparencies (Outputcity) using the 2D design to serve as the photomasks for photolithography. Channels were designed for simplicity of microfabrication as rectangular with a height of 150µm, large enough for cells to be transported through the channel in the streamline (h=75µm) but small enough to result in laminar flow with a large surface to maximize the number of cells and the throughput. Laminar flow was verified by calculating the Reynolds number, which for a rectangular channel is defined as $Re = \frac{\rho U_o D_h}{\mu}$ with $D_h = 2h$ for $h \ll w$ where ρ is fluid's density, U_o is velocity, D_h is hydraulic diameter, and μ is viscosity. The maximum flow rate, 90ml/min, was calculated by solving for flow rate with a Reynolds number of 2000, which results in shear stresses of 2670 dynes/cm^{2,} a magnitude of order larger than the shear stresses identified using the spinning disk assay to remove 50% of the cell populations. A larger surface area of 2214mm^2 is achieved using a channel with width of 1.5mm and turns with radius of curvature of 1mm, which allow the channel to cover a large area on the 4inch silicon wafer onto which the design is microfabricated. The 3D design was imported into COMSOL Multiphysics software and the Laminar Flow physics (spf) was used to simulate fluid flow of an incompressible fluid and shear stress over the channel surface was plotted for various input flow rates using the equation $\tau = \dot{\gamma} * \mu$, where τ =shear stress, $\dot{\gamma}$= shear rate, and μ = viscosity, (or COMSOL as spf.mu*spf.sr).

2.6.4 Photolithography and Silicon Wafer Fabrication

Mastermolds with channel features were microfabricated using SU-8 2100 (MicroChem), a permanent epoxy negative photoresist in Nano3 clean room facilities. A silicon wafer (University Wafer) was cleaned with IPA, acetone and H_2O, and coated with SU-8 2100 by using the recommended spinning parameters described by Microchem for a feature height of 150μm. Specifically, 4mL of SU-8 2100 was spun first at 500 rpm for 10 seconds, accelerated at 100 rpm/sec and then at 200 rpm for 30 seconds, accelerated at 300 rpm/sec. Once coated, edge beads were removed and the wafer was baked for 5 minutes at 65°C and then 28-30 minutes at 95°C, or until dry. The softly baked photoresist coated wafer was then exposed to UV while in hard contact with the photomask using a Karl Suss Mask Aligner for 23.6 seconds, delivering 11mW/cm^2 of power and 260 mJ/cm^2 of energy to cure exposed regions. The wafer was baked post exposure at 65°C for 5 minutes and then for 12 minutes at 95°C. The uncured photoresist was then removed by washing in SU-8 developer for 15-17 minutes. Feature height was measured using a DekTak Surface Profiler and finished wafers were coated using chemical vapor deposition with dichlorodimethylsilane (DCDMS, Arcos) overnight.

2.6.5 Soft Lithography and Microfluidic Device Fabrication

Microfluidic devices were fabricated using Polydimethylsiloxane, PDMS, Sylgard 184 (The Dow Chemical Company) 1:10 curing agent to silicone elastomer and cast onto the master mold wafer. Cast samples were degassed in a vacuum chamber and cured either overnight at room temperature or at 65°C. Inlet and outlet holes were formed by using a 1mm biopsy punch and PDMS. PDMS was cleaned with IPA, water, and scotch tape and bound to a 10.6cm x 10.2cm glass slide (The Gel Company) by plasma treating each surface for 30 seconds using an AutoGlow Plasma System (GLOW Research,) with its chamber's oxygen pressure set to .85 Torr and Radio Frequency (RF) set point at 30 Watts. Samples were then baked for an hour at 80°C.

2.6.6 Quantification of Adhesion Strength under Uniform Shear Stress and sorting of WA and SA populations

To expose cells to a uniform shear stress in the microfluidic device, the inlet is connected to a syringe pump with a programmable flow rate through a syringe (Becton Dickinson), tubing with 1/8 inch inner diameter (Fisher Scientific), polypropylene luer fixtures (Cole Parmer), and stainless steel inlet needle (Vita Needle). Bound microfluidic devices were sterilized by running 70% ethanol through the device, having autoclaved the tubing, luer locks, and needles for 15 minutes at 121°C prior. The devices are then coated with gelatin for 10 minutes and then serum proteins for 30 minutes by flowing .1% gelatin and DMEM/F12 +10% FBS+.2% amino acid concentrate+1% P/S through the device till it coats the surface. SMCs are then seeded in the device by flowing concentrated cell suspension at 300,000 cells/mL to result in approximately 4000 cells/cm^2 through the channels at 0.1ml/min for 0.5ml, a low enough flow rate that the resultant shear stresses are considered not physiologically relevant and using a volume large enough to coat the device. Seeded devices are then incubated overnight at 37°C and 5% CO2 to allow for cell attachment and placed in a closed petri dish to prevent media evaporation through the porous PDMS and inlet/outlet overnight.

To perform shear assays and select for the weakly and strongly adherent populations, the chosen shear stress is achieved by adjusting the input volumetric flow rate, using the following relationship between flow rate and shear stress:

$$\tau = \frac{6\mu Q}{wh^2}$$

Where τ= shear stress Q=the flow rate, μ= viscosity of the fluid, *w*=width of the channel and *h*=height of the channel, as measured by the DekTak. To select the weakly adherent population (WA), 4.5 mg/ml dextrose (Fisher) in Phosphate Buffered Saline (PBS, Gibco) was loaded into the syringe and run over the cells for 2 minutes at a preselected flow rate, while the outlet flow through containing cells was collected into a conical tube. Flow through was then counted using a hemocytometer and centrifugation at 1500 RPM for 3 minutes. The cells were then either replated on gelatin coated plates at 3000 cell/cm^2 for immunofluorescent analysis or resuspended in another reagent for a different biochemical assay, such as Qiazol (Qiagen) to isolate RNA for qPCR.

The strongly adherent population (SA) was then collected by enzymatic dissociation, flowing TryplE through the device at 0.1 ml/min for 0.5 ml, enough volume to coat the surface. The device was then incubated for 4 minutes, or until the cells lifted, and the SA population was then collected in a conical tube at the outlet by running 1ml DMEM/F12 media through the device at 1ml/min. This fraction is counted, centrifuged, and resuspended in the same media or reagent for further analysis as was done for the WA.

To measure the percentage of cells that detached from the device at a given shear stress or chosen flow rate, the transparency of the device was utilized to count the number of cells in three different representative areas of the channel, drawn onto the glass bottom. The number of cells in each area was counted and averaged before exposure to shear stress and then again immediately after WA selection.

2.6.7 Spinning Disk Assay

VSMCs were seeded onto collagen coated glass coverslips and spun using a spinning disk protocol previously described[217].

2.6.8 Immunofluorescence Assays

Cells were fixed in 3.7% formaldehyde in Solution A for 10 minutes and permeabilized using 1% (w/v) Triton X-100 for 15 minutes at room temperature and samples were stored at 4°C. Solution A consisted of .5mM MgCl2 in PBS. iPSCs were incubated in 2.5% (v/v) donkey serum in Sol A blocking buffer for 30 minutes at room temperature. Next, samples were incubated for two hours at room temperature in anti-Sox2 (mouse, 1:200, Abcam), anti-Nanog (Rabbit, 1:20, Abgent) and anti-Oct4 (Goat, 1:200, Abcam) antibodies in 2.5% goat serum in Sol A. Samples were then incubated for 45 minutes at room temperature in Alexa Fluor 488 conjugated donkey anti-mouse secondary antibody (1:1000, Life Technologies), Alexa Fluor 568 conjugated donkey anti-rabbit secondary antibody (1:1000, Life Technologies), Alexa Fluor 647 conjugated donkey anti-goat secondary antibody (1:1000, Life Technologies) in 2.5% donkey serum in Sol A.

For staining to confirm cells were differentiated, VSMCs were incubated in 10% FBS in Sol A blocking buffer for 20 minutes and then incubated at room temperature for 2 hours in anti-Calponin (Mouse, 1:200, Abcam) and anti-SM22 (Rabbit, 1:200, Abcam) antibodies in 10% FBS in Sol A. Next, cells were incubated for 45 minutes in Alexa Fluor 488 goat anti-mouse secondary antibody (1:1000, Life Technologies) and Alexa Fluor 568 goat anti-rabbit secondary antibody (1:1000, Life Technologies) in 10%FBS in Sol A.

For Alpha Smooth Muscle Actin expression measurements, VSMCs were incubated with 10% FBS in Sol A blocking buffer for 20 minutes and then for 2 hours at room temp in anti-αSMA (Rabbit, 1:200, Abcam). Finally, cells (both iPSC and SMC) were stained with DAPI (1:1000, Sigma/Roche) in H2O for 3 minutes and mounted to glass slides using Fluoromount-G (Southern Biotech) following rinsing in DI H2O. Cells were imaged using a 10x objective on a Nikon Eclipse T1 fluorescent microscope and Metamorph 7.6 software or using a LSM 780 Zeiss confocal microscope and Zeiss software.

For Alpha SMA quantification, all samples were stained using the same antibody master mix on the same day and imaging was completed using 10x magnification and the same microscope exposure settings for all samples. Images were then analyzed an Image J (Fiji) and the open-source integrated intensity density descriptor measurement tool to output the integrated pixel intensity for the selected cell area.

2.6.9 Morphology of WA and SA populations

WA and SA populations were seeded on gelatin coated 6 wells at 3000 cells/cm^2 and incubated overnight. Samples were then fixed using 3.7% formaldehyde in Sol A for 10 minutes after rinsing with PBS three times. Samples were treated with cell membrane stain Cell Mask (1:1000, Thermo Scientific) and DAPI (1:1000) for 15 minutes in the dark and then rinsed and stored in PBS and parafilm at 4°C. Imaging was performed at 10x magnification in the CY5 channel using LSM 780 Zeiss confocal microscope and Zeiss software. Images were then analyzed an Image J (Fiji) script which converted images to a binary mask for pixels above a threshold intensity and used the open-source area and cell shape descriptors measurement tools to output cell area and circularity.

2.6.10 Traction Force Microscopy

Cell contraction strength of the WA, SA and unsorted, US, populations was measured using traction force microscopy (TFM). 2.6 kPa polyacrylamide gels (PA) embedded with 2% (v/v) 0.2µm fluorescent beads (680/605) were fabricated to mimic the stiffness of the arterial wall and SMCs were seeded onto the PA gels at 6,000 cell/well for imaging of bead displacement. To develop the PA gels, 12 well plates with glass bottoms (Cellvis) were first functionalized for 5 minutes using 0.5% (v/v) % 3-methacrylate 3% (v/v) acetic acid in ethanol solution post UV-Ozone treatment for 5 minutes to promote gel-glass binding. Acrylamide/bis-acrylamide (Fisher) polymer solution was cured by sequentially adding and vortexing 1% (v/v) of 10% ammonium persulfate (Fisher) for crosslinking, fluorescent beads, and 0.1% (v/v) of Tetramethylethylenediamine (TEMED, VWR International) to catalyze the reaction. 20uL of PA gel solution is added to each functionalized glass well and the surface is flattened by sandwhiching the gel with a DCDMS treated (to prevent binding) 15mm glass coverslip, which allows for the PA solution to polymerize with a flat surface. Once polymerized, the coverslip was removed and the surface was functionalized with collagen using N-sulphosuccinimidyl-6-(4’-azido-2’nitrophenylamino) hexanoate (sulfo-SANPAH, Fisher), which provides a photoactivated linker between the gel and amine groups on the protein of choice. Specifically, 0.2mg/ml sulfo-SANPHA in sterile 50mM HEPES, pH 8.5, was added to the hydrogels and was UV activated for 10 minutes using a UV box (wavelength 350nm, intensity 4mW/cm^2). 0.1% gelatin solution was added after rinsing in HEPES three times and the gels were coated overnight in the incubator. After sterilizing with UV for one hour in the biosafety hood, cells are seeded on the gel at 1300 cells/cm^2 and incubated overnight before imaging using a 60x water immersion confocal objective. Individual cells were located and imaged in brightfield, and the beads at the top of the gel at the same xy position were imaged in TXRED and position recorded. Cells are then removed/lysed by added 10% Triton X for 15 minutes and the beads in the same xyz position are imaged again without the cells for a relaxed hydrogel, reference image. Bead displacement between images with and without cells were determined using a particle image velocimetry script in Matlab and normalized to cell area, measured in Image J.

2.6.11 Doubling Time Measurement

Doubling time was determined by measuring cell growth for five days, every 24 hours, post replating. Cells were seeding at initial seeding density of 3000 cells/cm^2 and were counted in Brightfield in four representative areas marked on the bottom of the well. Cell count over time was plotted and an exponential growth curve was fit using Microsoft excel. Doubling time was calculated using $time_{doubling} = \frac{ln2}{growth\ rate}$ and growth rate=exponent of exponential best fit curve.

2.6.12 Quantification of Alpha-Smooth Muscle Actin Expression using Western Blot

iPSC-derived VSMC's were seeded in a 6 well plate at a density of 10,900 cells$^/$cm^2, cultured for 24 hours, then rinsed with PBS before adding 300uL of mRIPA (50mM HEPES, .5M EDTA, 1.5mM,150mM NaCl in 10% MgCl2,1% Triton X, 1% Sodium Deoxycholate, 0.15% Soldium Dodecyl Sulfate, with 1 protease inhibitor tablet /50mL (Pierce Protease Inhibitors #88266), and 5 phosphatase inhibitor tablets/50mL (PhosSTOP, Cat 04 906 836 001) for 1-2 minutes. Cell lysis was collected using a cell scraper and transferred to a microfuge tube. Samples were incubated on ice and vortexed every 5 minutes for a total of 30 minutes and then centrifuged at 4°C for 15 minutes at 15000 rpm. Supernatant was then collected and was either used immediately for Bicinchoninic Acid (BCA) assay or stored at -80°C. For the BCA assay,10ul of each BCA standard and sample was loaded into 3 wells of a 96 well plate. 200ul of BCA working reagent (Thermofisher) was pipetted into each of the wells. The plate was then incubated for 30 minutes before absorbance of each well was measured using Synergy 4 Multi-Mode Microplate Reader (BioTek). A standard curve was generated, and the polynomial was used to calculate the average protein concentration of each sample. 5ug of protein sample was added with 4X loading buffer (1:4 dilution, Laemmli), 50mM DTT, and a variable amount of mRIPA to a total of 50uL in microfuge tubes. Samples were then heat inactivated for 5 minutes at 95° in a heating block and immediately placed on ice afterwards. Room temperature 4-12% bis tris gel (Invitrogen) and 1X MOPS buffer (Invitrogen) was used for gel electrophoresis. Samples were loaded carefully into each well alongside protein ladder chameleon duo (LiCor). Gel was run at 140V for 1 hour. After gel electrophoresis was complete, the transfer system and gel were then assembled according to the iBlot Invitrogen protocol. The transfer system was run for 7 minutes. The blot was then removed from transfer system and was blocked using fluorescent blot blocking buffer (Azure) for 1 hour at room temperature with agitation. After blocking, the blot was incubated with anti-α-SMA (Mouse, 1:2000, Abcam) and anti-GAPDH (Mouse, 1:2000, Abcam) antibodies in fluorescent blocking buffer overnight at 4°C with agitation. After primary antibody incubation, the blot was rinsed 3 times for 5 minutes with 1X tris buffered saline + 0.1% Tween (TBST) with agitation. Secondary antibody (Goat anti-Mouse, 1:5000, Lifetechnologies) in blocking buffer was then added at a 1:5000 ratio for 1 hour at room temperature with agitation. The blot was then rinsed again 3 times for 5 minutes with TBST before blot was imaged on LICOR imaging system. α-SMA abundance was then normalized using GAPDH.

2.6.13 RNA Sequencing

RNA sequencing was performed on these patient derived iPSC lines and the differentiated SMCs as previously described[23]. To investigate integrin transcriptomic differences between SMCs of different risk factor, bulk raw counts for integrin genes (log scale) were accessed using accession number GEO: GSE12099 and were analyzed using Morpheus software (Broad Institute). Hierarchical clustering was performed across patient lines using the Pearson correlation to cluster patient line by similarity of gene expression.

RNA was also isolated from VSMCs of the sorted populations (WA, SA) RR Patient 1 as well as unsorted controls from RR Patient 1 WT and RR Patient 1 KO were submitted to the UCSD Institute for Genomic Medicine Sequencing Core. Quality of total RNA was assessed using an Agilent Tapestation 4200, and samples with an RNA Integrity Number (RIN) greater than 8.0 were used to generate RNA sequencing libraries using the TruSeq Stranded mRNA Sample Prep Kit with TruSeq Unique Dual Indexes (Illumina, San Diego, CA). Samples were processed following manufacturer's instructions and resulting libraries were multiplexed and sequenced with 100 basepair (bp) paired end reads (PE100) to a depth of approximately 25 million reads per sample on an Illumina NovaSeq 6000. Samples were demultiplexed using bcl2fastq v2.20 Conversion Software (Illumina, San Diego, CA). Analysis was conducted using STAR, R, DeSeq2, and python software. Data were further analyzed through the use of IPA (QIAGEN Inc., https://www.qiagenbioinformatics.com/products/ingenuitypathway-analysis). GO terms for co-regulated DEGs were identified using Gene Enrichment Analysis powered by PANTHER version 14[218–220]. GEO accession number for RNA Sequencing Data is GSE211144.

2.6.14 Reverse Transcription Quantitative Polymerase Chain Reaction (RT-qPCR)

WA, SA, US, and an unsorted population cultured in the device (USID) were replated onto gelatin coated 6 well plates at 3,000 cells/cm^2 and cultured overnight. Cells were then rinsed it PBS three times before resuspension in Qiazol for storage at -80°C. RNA was isolated using Qiagen's miRNeasy Kit, a Qiazol-chloroform extraction protocol. All samples were handled using Ambion DNA-free DNase Treatment (Thermo Scientific) to remove genomic DNA contamination, as per manufacturer's instructions. Following RNA isolation, samples were treated with a recombinant DNAse to eliminate any gDNA contamination, using Thermo Fisher's DNA-Free kit. 30-100ng of isolated RNA was then reverse transcribed to cDNA using Super Script III Reverse Transcriptase (Thermo Scientific) and quantitative PCR as performed using 7900 HT Fast Real-Time PCR System. cDNA was amplified and detected using Q SYPBR Green Supermix (Bio-Rad Laboratories) and primer sets for the short and long isoforms as described in the supplementary material **Table S7**. A fibronectin plasmid standard curve was generated to calculate absolute quantity of RNA based and data was normalized to Peptidylprolyl Isomerase A (PPIA) expression per sample. Expression relative to PPIA was further normalized to the average expression of either RR or USID for haplotype or adhesion based sorted comparisons, respectfully.

2.6.15 Doxycycline Inducible ANRIL Overexpression by Lentivirus Transformation

RRKO VSMCs from multiple differentiation batches, and various passage numbers, were replated the day before infection, at a seeding density equal to or less than 3,500 cells/cm^2. Lentiviral particles containing sequences encoding either A11 or A12, two short isoforms of *ANRIL* were added to the cells at various concentrations (2,4,6, or 8 ul per thousand cells), alongside reverse tetracycline-controlled transactivator, rtTA (2,4,6, or 8ul per thousand cells) to determine the concentration that would result in ANRIL expression levels most comparable to the RR VSMCs from the same patient as the RRKO. 24 hours after infecting the cells, media was changed to that containing 100ng/ml Doxycycline hyclate (Sigma D9891) an analog of Tetracycline, which induced expression of ANRIL, by binding rtTA such that it could bind the Tet Responsive Element (TRE) containing the Tetatrycyline Operator (TetO). Doxycycline media was replenished every other day due the relatively short half-life of doxycycline. After 8 days, cells were lysed using Qiazol for qPCR. ANRIL expression was measured using the primers that bind the short isoforms of ANRIL, as described in **Table S7**, and expression was normalized to the average expression for RR VSMCs. The concentration of lentiviral particles and rtTA which resulted in expression of ANRIL closest to that of the RR was then selected for all future viral infections. All sorts using the microfluidic device using RRKO overexpressing A11 or A12 were performed by seeding cells in the device on Day 8 of Doxycycline treatment, using media not containing Doxycycline, such that levels reported in PCR were expected at the time cells were exposed to fluidic shear stress. Similarly, cells were replated on Day 8 for other assays, such as IF to measure Alpha SMA expression and TFM.

2.6.16 Statistical Analysis

All given values are means expressed with +/- standard deviation. When comparing two groups, statistical differences were tested using a two-tailed Student's t test. Statistical differences between more than two groups were analyzed using one-way analysis of variance (ANOVA) and then Tukey's multiple comparison test, with $p<0.05$ as the threshold for significance. For TFM and PCR of the titration of lenti-viral prep, non-parametric one-way ANOVA was used with the Kruskal-Wallis multiple comparison test, with $p<0.05$ was the threshold for significance. All statistical analysis was performed in Prism software (Graphpad). For comparisons of two factors on a dependent variable/group (for example: cell area and circularity for WA or SA), two-way ANOVA was used, and column factor and interaction were calculated, with $p<0.05$ was the threshold for significance.

2.7 Supplemental Figures

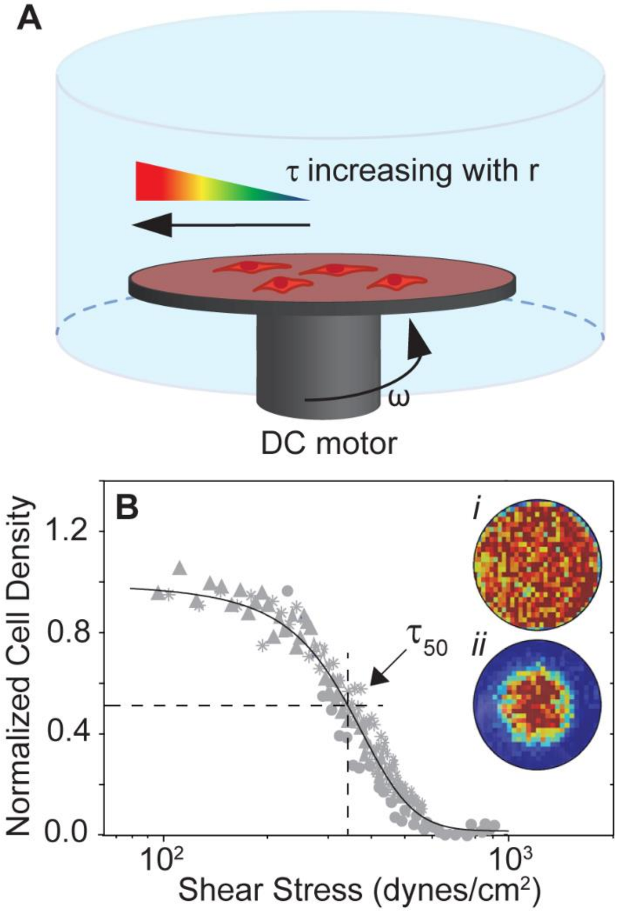

Supplemental Figure 2.1. Spinning Disk Assay Measures a population's strength of adhesion to the ECM: (A) Schematic for the spinning disk assay, in which cells are seeded onto a coverslip seeded with ECM protein, in these experiments collagen, submerged in a water bath, and spun (ω symbolizes angular velocity). This results in radially (r) increasing shear stress (τ; measured in dynes/cm^2). **(B)** Imaging of the coverslip before (i) and after (ii) rotation allows for normalized cell density to be plotted versus shear stress (a function of radial position). The shear stress at which 50% of the population detaches, τ_{50}, is then used as a metric for the adhesion strength of a population, with a greater τ_{50}, for more adhesive populations as a greater shear stress is required to detach cells (n = 702 cells in the example fit).

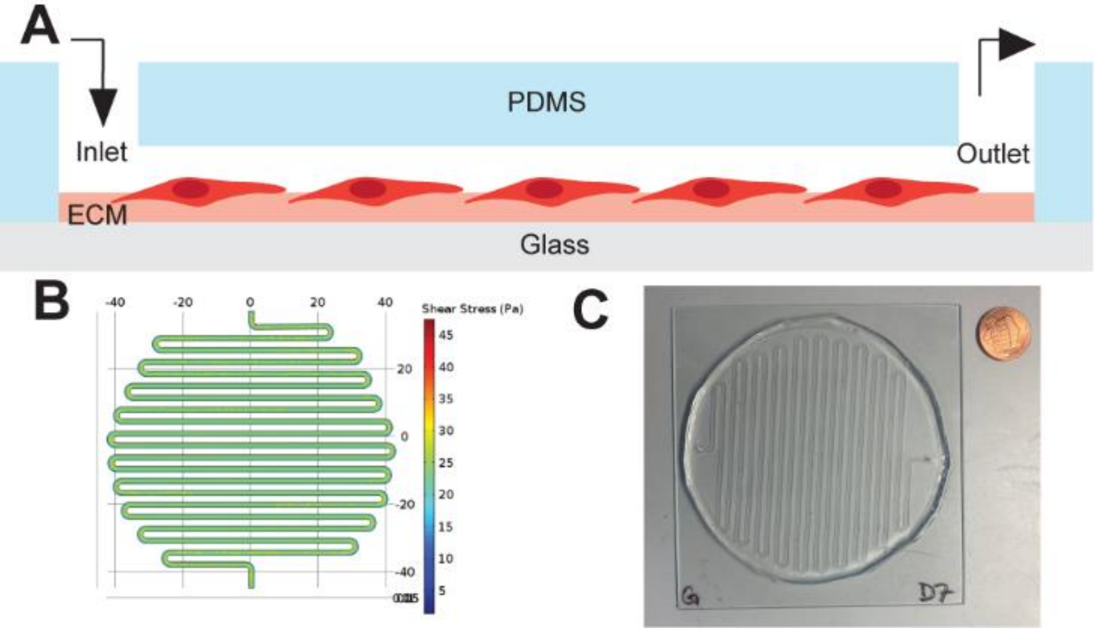

Supplemental Figure 2.2. Microfluidic Device Collects Weakly Adherent (WA) and Strongly Adherent (SA) populations: (A) Schematic of the microfluidic device used to capture WA and SA populations. A rectangular channel bound between glass and PDMS is coated with ECM protein (e.g., collagen) and connected to syringe pump at the inlet. Cells seeded in the device are exposed to a tunable shear stress as media is perfused through the channel. Cells that detach when exposed to the fluidic shear stress are collected at the outlet (WA) and those that remain adherent in the channel (SA) are collected by enzymatic dissociation, running TryplE through the channel. The device was designed such that flow rates resulting in wall shear stress of 2500 dynes/cm^2 (an order of magnitude higher than the greatest $\tau 50$ identified using the spinning disk) still results in laminar flow (Reynolds number<2000). **(B)** Heatmap of the shear stress across the surface of the channel, generated using COMSOL, indicating the uniformity of the shear stress at an arbitrary volumetric flow rate. **(C)** Image of the microfluidic device (with adjacent penny for scale). The channel width and height are 1.5 mm and 150µm, respectively. The serpentine pattern maximizes surface area for cell adhesion in the device.

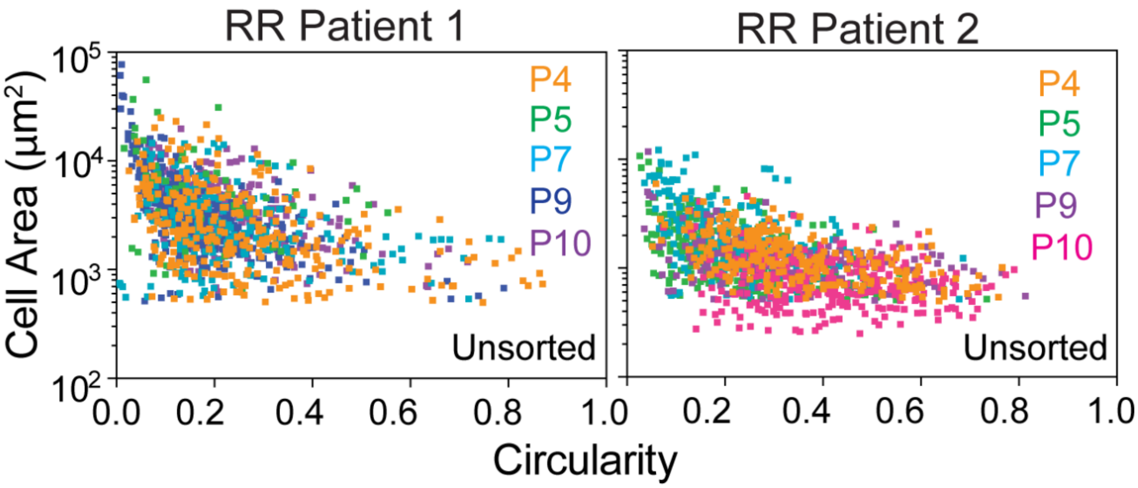

Supplemental Figure 2.3. iPSC derived VMSC morphology does not shift with time in culture and cell culture passaging: The cell area and circularity for VSMCs derived from both RR patients are plotted after passaging, color coded by passage number from passages 4 (P4) to 10 (P10). No statistical differences were found between any population within the same patient. N=292, 58, 227, 368, and 287 cells for RR patient 1 for P4, P5, P7, P9, and P10, respectively. N=263, 335, 227, 151, and 310 cells for RR patient 2 for P4, P5, P7, P9, and P10, respectively.

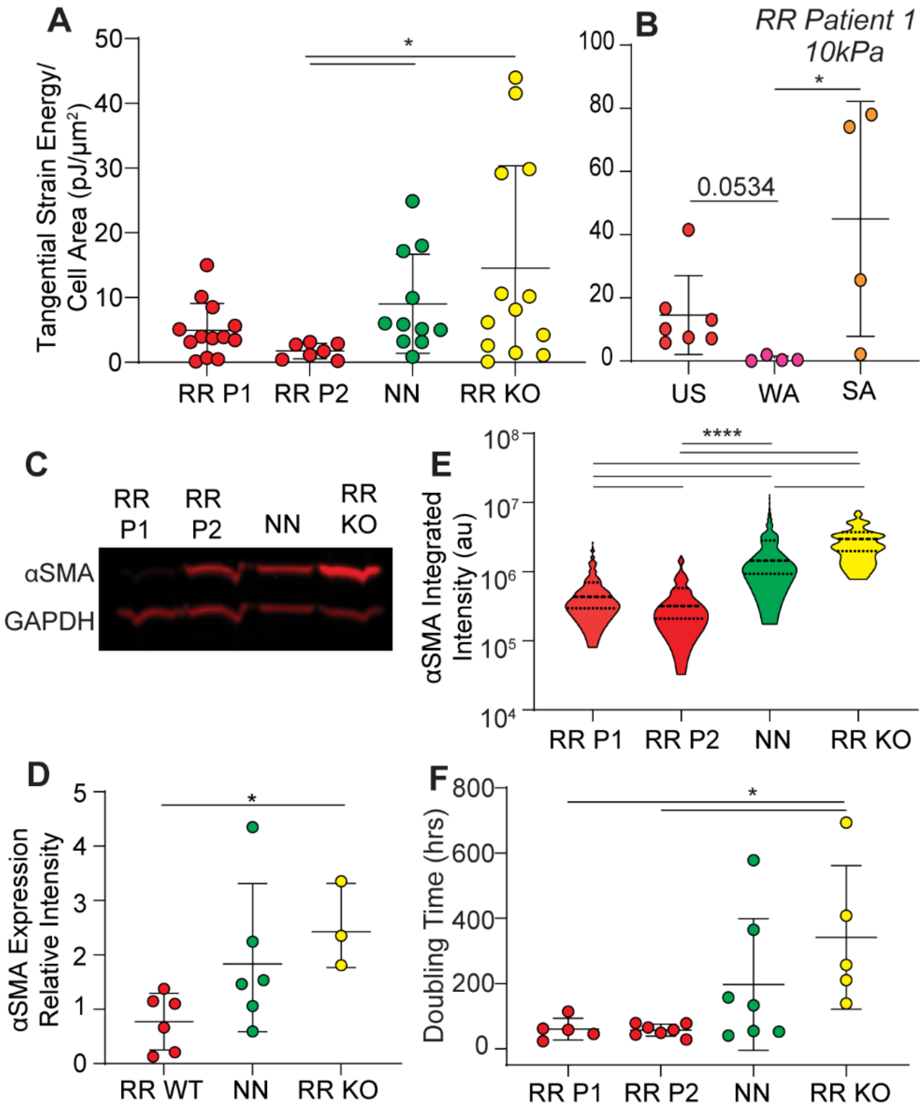

Supplemental Figure 2.4. Phenotype differences between RRWT Patients and NNWT Patients and RRKO VSMCs: (A) Traction force microscopy (TFM) contractility measurements of unsorted VSMCs derived from RRWT, NNWT, and RRKO patients. Tangential strain energy per square micron is plotted using batches from different differentiations and at different passage number. N = 13, 7, 11, and 13 cells from RRWT P1, RRWT P2, NNWT, and RRKO, respectively. *$p<0.05$ for one-way ANOVA with Kruskal-Wallis multiple comparisons test. **(B)** TFM measurements of RRWT Patient 1 derived VSMC sorted at 30 dynes/cm2 measured on a stiffer polyacrylamide (PA) gel, specifically elastic modulus of 10 kPa. N = 7, 4, and 4 cells from unsorted, weakly adherent and strongly adherent cells, respectively. *$p<0.05$ for one-way ANOVA with Kruskal-Wallis multiple comparisons test. **(C)** A representative western blot is shown for αSMA expression and GAPDH for unsorted VSMCs derived from the indicated haplotypes. **(D)** αSMA expression, measured using the band intensity from Western blots, comparing haplotypes, measured using multiple differentiation and passage number batches. N = 6, 6, and 3 blots for RRWT (pooled from both patients), NNWT, and RRKO, respectively. **(E)** αSMA expression measured using immunofluorescent imaging and summing pixel intensity over cell surface area for different haplotypes also measured using multiple differentiation and passage number batches. N = 166, 187, 229 and 84 cells from RRWT P1, RRWT P2, NNWT, and RRKO, respectively. **(F)** Doubling time of VSMCs derived from RRWT, NNTW and RRKO iPSC lines, for multiple differentiation and passage number batches. N = 5, 7, 7, and 5 cell cultures from RRWT P1, RRWT P2, NNWT, and RRKO, respectively. *$p<0.05$, **$p<10-2$, ***$p<10-3$, and ****$p<10-4$ for one-way ANOVA with Tukey's multiple comparisons test.

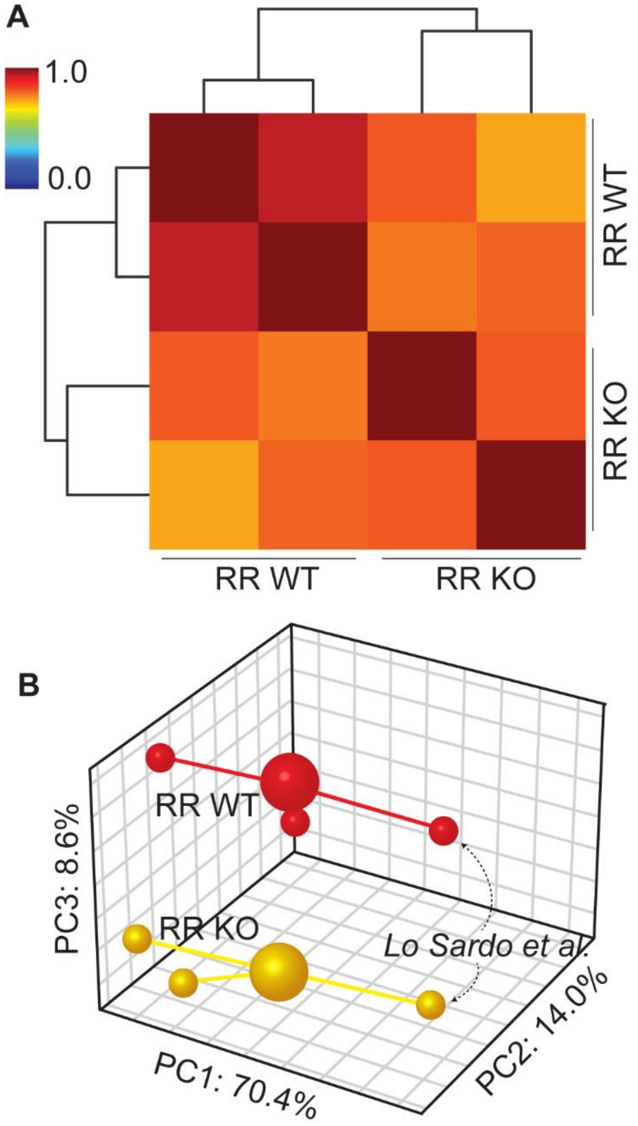

Supplemental Figure 2.5. RNA Sequencing of unsorted VSMCs from RR Patient 1 and its KO line demonstrate clustering by genotype: (A) Pearson’s correlation plot is shown based on the whole transcriptome sequenced from patient iPSC-derived VSMCs (unsorted), with haplotypes indicated. Dendogram indicates sample clustering and color map is plotted between 0 and 1. **(B)** A 3D PCA plot is shown for transcriptomes from RR Patient 1 WT (red) and RR Patient 1 KO (yellow) unsorted VSMCs from multiple differentiation batches and passage numbers; transcriptome from Day 17 VSMCs from the same iPSC clonal lines as reported in Lo Sardo et al are also included. The contribution of each PCA axis is noted alongside the axis itself.

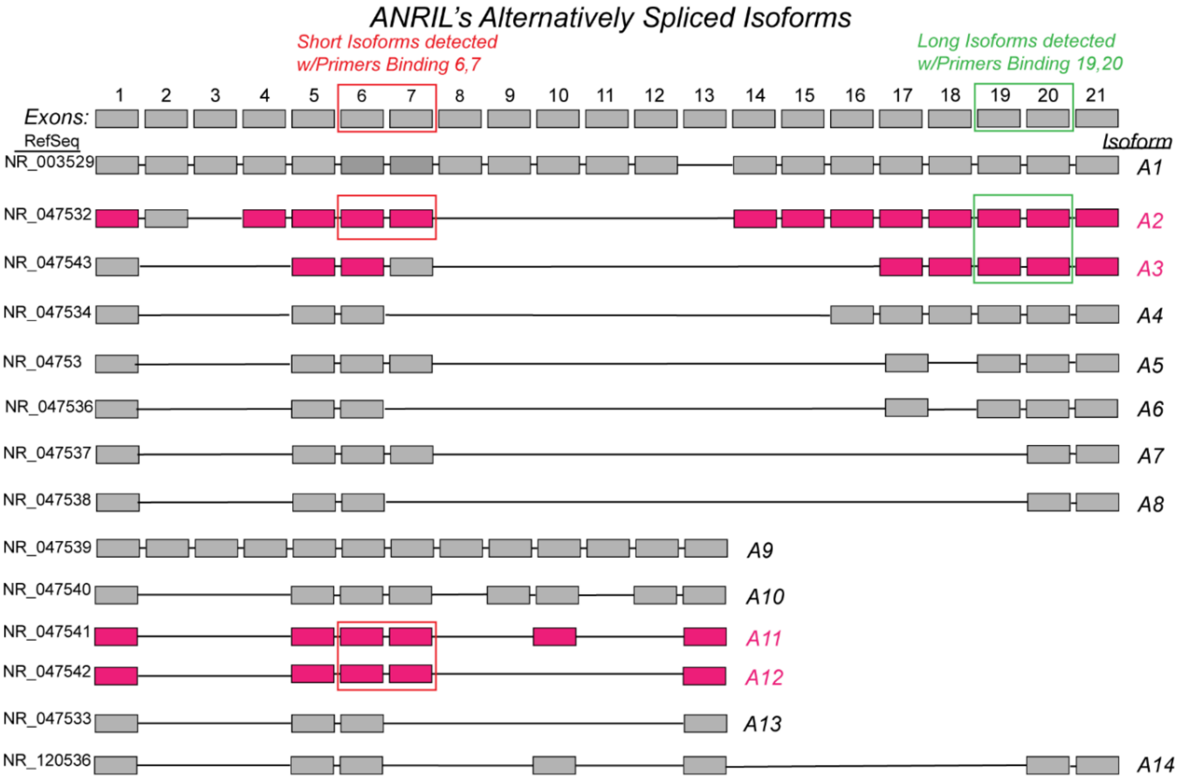

Supplemental Figure 2.6. Alternative Splicing of Exons Resulting in the Linear Isoforms of ANRIL measured using qPCR: Schematic showing exons of ANRIL, and how they are alternatively spliced to form different linear isoforms, as described in Kong et al[221] with their corresponding RefSeq IDs from NCBI. Isoforms are numbered A1-A14, with the exons of the isoforms that were detected in Day 17 iPSC-VSMCs highlighted in pink, as previously numbered and reported in Lo Sardo et al[23] . For RT-qPCR, "short isoforms" of ANRIL were measured using primers binding exons 6 and 7 (red), "long isoforms" of ANRIL were measured using primers binding exons 19 and 20 (green). Notably, exons 19 and 20 in this schematic are consistent with the numbering system in Kong, and match exons "18 and 19" in Lo Sardo et al[23].

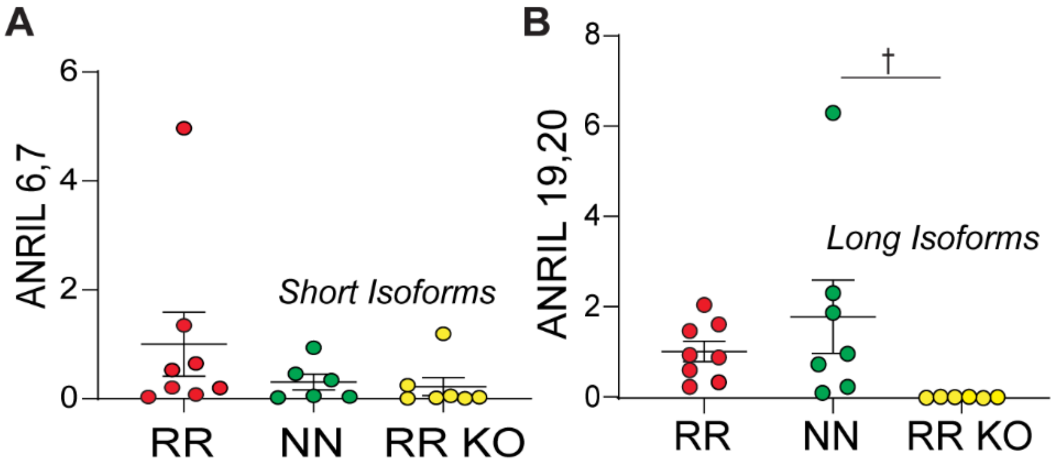

Supplemental Figure 2.7. Increased expression of lncRNA, ANRIL, in RRWT derived VSMCs relative to NNWT and RRKO iPSC lines: (A) Expression of isoforms of ANRIL spanning exons 6,7 measured using qPCR for VSMCs derived from patients with different haplotypes (RRWT-red, NNWT-green) and a RRKO line (yellow). ANRIL expression, relative to housekeeping gene PPIA, was normalized to average expression for the RRWT haplotype. VSMCs were used from multiple differentiation batches and on day 17 of differentiation. N = 8, 6, and 7 for RR, NN and RR KO, respectively. **(B)** Expression of long isoforms of ANRIL, measured using primers binding exons 19, 20. N = 8, 7, and 6 for RR, NN and RR KO respectively. *p<0.05, **p<10-2, ***p<10-3, and ****p<10-4 for one-way ANOVA with Tukey's multiple comparison test.

Supplemental Figure 2.8. Validation of A11 and A12 vector overexpression in RRKO VSMCs and phenotype effects: (A) Schematic demonstrating the lentiviral transformation of VSMCs differentiated from RRKO iPSCs. Cells were infected with viral particles, cultured for 24 hours, before A11 or A12 expression was induced using doxycycline media for 8 days before analysis. **(B)** Expression of ANRIL, measured using qPCR with primers binding exons 6,7, relative to housekeeping gene PPIA, normalized to average expression of RR haplotype. VSMCs were from multiple differentiation batches and passage numbers, for RR (red) and RR KO, which were cultured without exposure to lentivirus particle (regular media-yellow, Doxycycline media-orange, Doxycycline and rtTA containing media-orange) and exposed to a titration of viral prep concentration (pink) (in µl/10^3 cells-counted during replating the day prior to infection). Plasmid contained sequence for A11 isoform of ANRIL. †p=0.0629, *p<0.05, **p<10-2, ***p<10-3, and ****p<10-4 for one-way ANOVA with Kruskal-Wallis multiple comparison test. **(C)** ANRIL expression measured across a viral titration using plasmid containing sequence for A12 isoform of ANRIL, as described in panel B. **(D)** Cell area from multiple differentiation batches of RRKO VSMCs with multiple batches of the least concentrated viral infection with A11 or A12 (pink) as well as the null control (ø-yellow). N = 342, 454, and 386 cells from the null control, A11, and A12, respectively. ***p<10-3 and ****p<10-4 for one-way ANOVA with Tukey's multiple comparison test. **(E)** αSMA expression, as measured by the integrated intensity density of individual cells after immunofluorescent staining. Data is show from multiple differentiation batches of RRKO VSMCs with multiple batches of the least concentrated viral infection with A11 or A12 (pink) as well as the null control (ø-yellow). **p<10-2 and ****p<10-4 for one-way ANOVA with Tukey's multiple comparison test. N = 342, 454, and 338 cells from RRKO null control, A11 overexpressing, and A12 overexpressing. **(F)** Cell area of RRKO VSMCs after cultured in doxycycline media for 8 days (orange) compared to a null control (ø-yellow) from a singular differentiation batch and immunofluorescent staining batch. N = 135 and 108 cells from RRKO null control and doxycycline treated RRKO, respectively. **(G)** αSMA expression of RR KO VSMCs after cultured in doxycycline media for 8 days (orange) compared to a null control (ø-yellow) from a singular differentiation batch and immunofluorescent staining batch. N = 135 and 108 cells from RR KO null control and doxycycline treated RR KO, respectively. Student's t-test indicated non-significant (ns) differences in panels F and G.

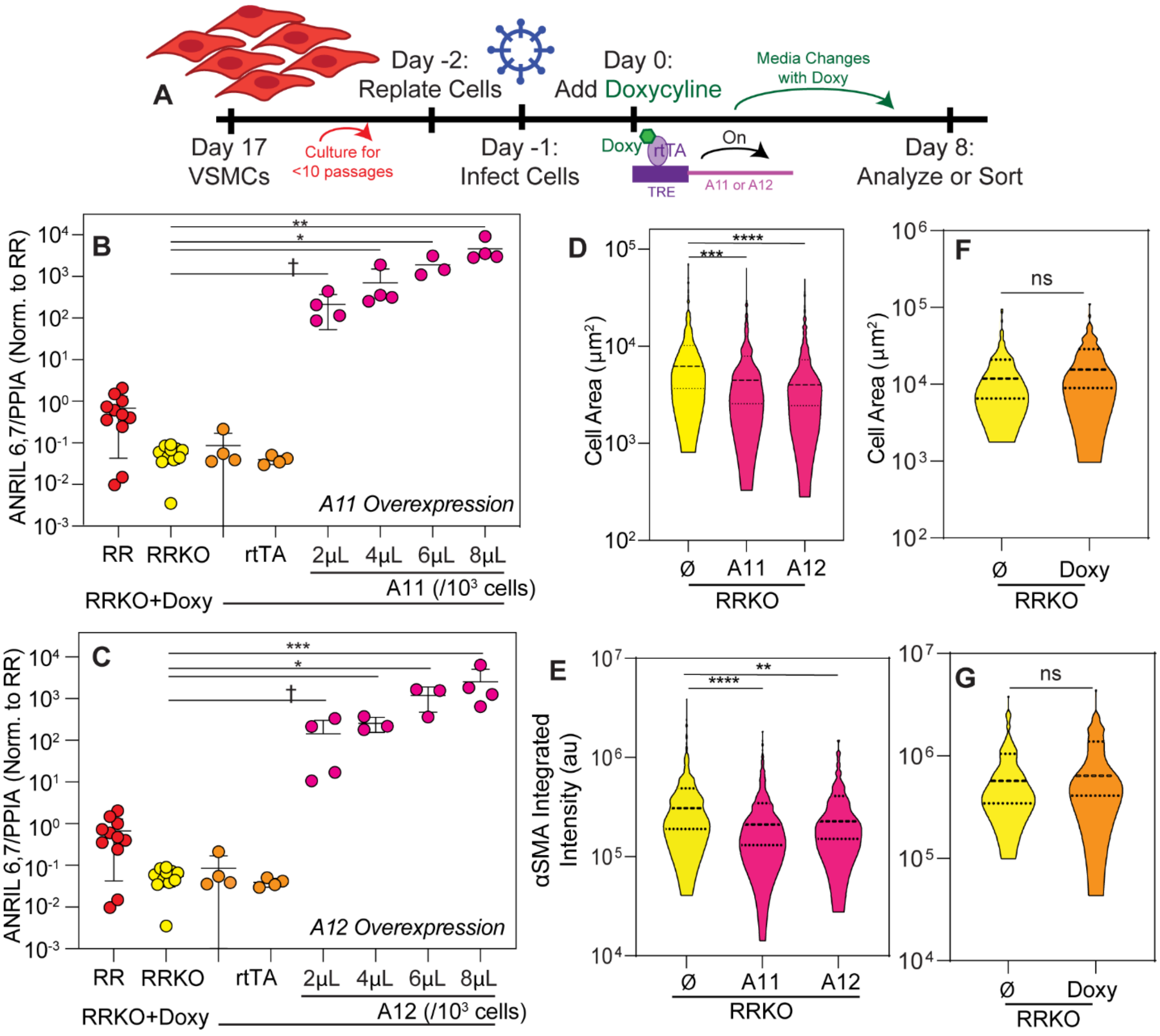
A
Day 17
VSMCs
Culture for
<10 passages
Day -2:
Replate Cells
Day -1:
Infect Cells
Day 0:
Add Doxycyline
Doxy
rtTA
TRE
On
A11 or A12
Media Changes
with Doxy
Day 8:
Analyze or Sort
B
ANRIL 6,7/PPIA (Norm. to RR)
10^4
10^3
10^2
10^1
10^0
10^{-1}
10^{-2}
10^{-3}
**
*
†
A11 Overexpression
RR
RRKO
rtTA
2μL
4μL
6μL
8μL
A11 (/10^3 cells)
RRKO+Doxy
C
ANRIL 6,7/PPIA (Norm. to RR)
***
*
†
A12 Overexpression
RR
RRKO
rtTA
2μL
4μL
6μL
8μL
A12 (/10^3 cells)
RRKO+Doxy
D
Cell Area (μm^2)
10^5
10^4
10^3
10^2
****
***
Ø
A11
A12
RRKO
F
Cell Area (μm^2)
10^6
10^5
10^4
10^3
10^2
ns
Ø
Doxy
RRKO
E
αSMA Integrated
Intensity (au)
10^7
10^6
10^5
10^4
**
****
Ø
A11
A12
RRKO
G
10^7
10^6
10^5
10^4
ns
Ø
Doxy
RRKO

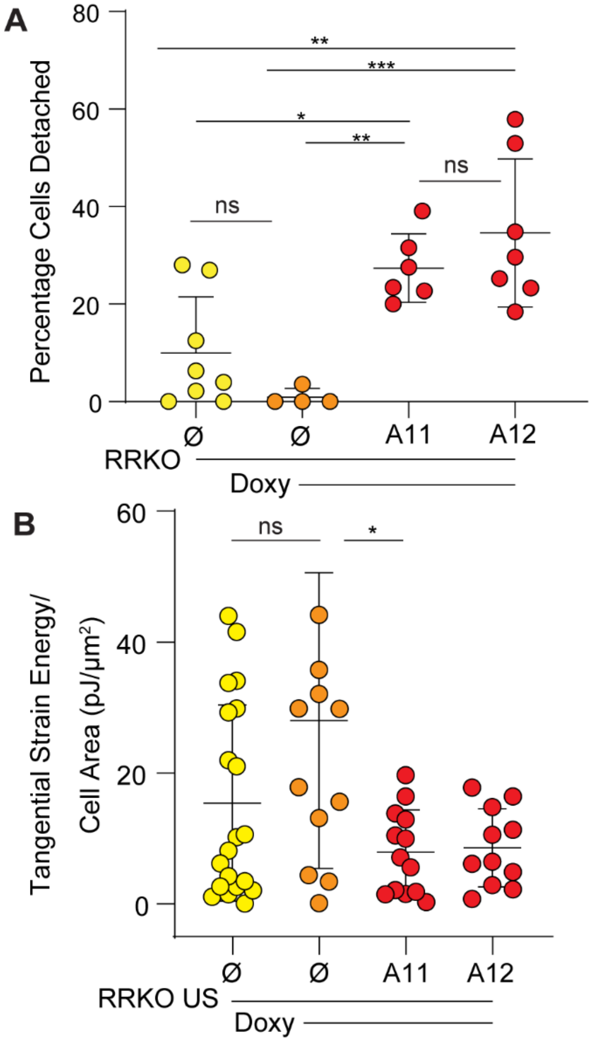

Supplemental Figure 2.9. RR KO VSMCs overexpressing A11 and A12 have reduced adhesion strength and contractility: (A) RR KO VSMCs were seeded into the microfluidic device and exposed to 90 dynes/cm^2 of fluidic shear stress. The percentage of cells that detached was measured for multiple differentiation batches for the null control (ø-yellow), cells cultured in Doxycycline for 8 days (ø-orange) and those overexpressing A11 or A12 (red) with multiple batches of lentiviral transformation. N=8, 4, 6 and 7 for RR KO null control, doxycycline only negative control, A11 overexpressing, and A12 overexpressing, respectively. *$p<0.05$, **$p<10^{-2}$, ***$p<10^{-3}$ for one-way ANOVA with Tukey multiple comparison test. **(B)** TFM measurements of unsorted RR KO transformed to overexpress A11 or A12 (red), and those not exposed to viral particles but cultured in doxycycline media for 8 days (orange) or regular media (ø-yellow). Tangential strain energy per square micron is plotted using different differentiation and passage number batches. N= 20, 13, 13, and 11 for RR KO null control, doxycycline only negative control, A11 overexpressing, and A12 overexpressing, respectively. *$p<0.05$ for one-way ANOVA with Kruskal-Wallis multiple comparison test.

2.8 Acknowledgements

The authors would like to thank Dr. Kristen Jepsen of the Institute for Genomic Medicine (UCSD) for technical assistance with sequencing, Cody Fine, Vu Nguyen, and Elsa Molina (Sanford Consortium Stem Cell and Genomic Cores) for technical expertise in flow cytometry and microscopy, Dr. Jesse Placone (UCSD) for assistance with manuscript preparation, and Dr. Jeff Hasty (UCSD) for equipment access. This work was performed in part at the San Diego Nanotechnology Infrastructure (SDNI) of UCSD, a member of the National Nanotechnology Coordinated Infrastructure, which is supported by the National Science Foundation (Grant ECCS-2025752). The authors acknowledge funding and equipment support from the National Institutes of Health (R01AG045428 and R01 to A.J.E. and S10OD026929 to UCSD IGM Genomics Center). Fellowship support was provided by the National Science Foundation (to A.K. and P.B.), National Institutes of Health (T32HL105373 to J.M.M. and T32GM008666 to E.M.M.), and American Heart Association (20PRE35180166 to E.M.M.). Chapter 2, in full, is a partial reprint of material as it appears in Mayner J, Masutani E, Demeester E, Kumar A, Macapugay G, Beri P, Lo Sardo V, Engler A.J. Heterogeneous Expression of Alternatively Spliced lncRNA mediates Vascular Smooth Cell Plasticity. Submitted. The dissertation author was the primary author of this paper.

2.9 Author Contributions

J.M.M., V.L.S., and A.J.E. conceived of the project and designed the experiments. J.M.M., E.D. and A.K. performed cell assays. J.M.M. and P.B designed microfabrication methods and microfluidic protocols. E.M.M. and J.M.M. performed and analyzed RNA sequencing.

G.M. and V.L.S. produced the lentivirus used in the manuscript. The manuscript was written by J.M.M. and A.J.E. with input from the other authors.

CONCLUSION

Both genetic and environmental factors influence cellular phenotype. While disease models that investigate these influences independently are tightly controlled and offer valuable insights, they do not capture the entire picture of disease. Systems where both factors and how they act together are modeled can elucidate novel pathways in disease development, prompting drug discoveries. This dissertation aimed to highlight the utility of such cross disciplinary studies, by first reviewing studies in which genetics and mechanical influence on cells were independently manipulated, and then providing an overview of studies in which combinatorial effects were investigated for their role in various cancers and heart diseases. In the second chapter, we provided a case study where mechanical and genetic factors were jointly manipulated to unveil insight into how a non-coding locus increases risk for coronary artery disease. Specifically, an adhesion-based microfluidic cell separation platform was used in combination with haplotype editing of patient derived iPSCs to identify how heterogenous expression of a long non coding RNA regulates vascular smooth muscle cell phenotype plasticity, creating more diverse populations in risk patients.

Genetic risk for disease includes both inherited and acquired sequence variants, in coding and non-coding loci. Next-generation sequencing techniques, have pathed the way for both genome wide association studies (GWAS), highlighting previously unknown disease associated loci, and tools for investigating gene expression profiles and chromatin accessibility, such as RNA Seq or ATAC Seq. Coupled with novel gene editing tools, such as TALENs and CRISPR, these developments have ushered in a new era of disease modeling where the contribution of individual genes to disease pathogenesis can be modeled *in vitro*.

Mechanical forces also play an important role in disease. Mechanical cues from the environment are largely passive and sensed by cells pulling or pushing on their niche. Conversely, external application of forces on cells, by matrix, other cells, or fluid, can also significantly impact cell function. Engineering systems that mimic these passive and active forces from the microenvironment, allow for conditions in which a cells gene expression and phenotype more closely recapitulate *in vivo*. For example, to mimic the elastic and viscoelastic properties of the ECM, hydrogels with tunable stiffness can be utilized [57,59,222,223]. The fibrillar architecture of collagen and fibrin, while not captured with hydrogels, can be recreated with electrospinning fibrous scaffolds[112–115]. To mimic hydrodynamic forces exerted on cells, microfluidic devices or 3D printing of vasculature can be employed, with the later able to mimic patient specific 3D architecture when paired with MRI or CT data[119].

For some pathologies, a change in the mechanical output of individual cells or tissues is hallmark of the disease, such as reduced cardiomyocyte contractility in dilated cardiomyopathy[28]. In other diseases, the relationship between mechanical output and disease status is less understood. For both, the use of materials based mechanobiological measurements adds valuable quantification to cellular phenotype. Such measurements can examine a cell's interaction with the ECM, or such as the traction forces exerted by a cell onto its environment [36], or the adhesion of the cell to the ECM when exposed to fluidic shear stress [37]. These mechanobiological measurements can also measure cell-cell interactions, which can be altered in disease, such as disruption of the endothelium in coronary artery disease [38,47–51] or intravasation of cancer cells from the primary tumor.

Combinatorial effects of genetics and mechanics are increasingly becoming recognized for their importance in disease pathology. Most genetic risk variants identified through GWAS for CAD act through unknown mechanisms[20] and therefore present a perfect opportunity for novel approaches that perturb and measure both genetics and mechanics. As a model, we chose to study the SNPs at the 9p21 locus, which have the highest association with coronary artery and increases risk up to 60% risk[21]. Using VSMCs differentiated from patient derived iPSCs, we noted significant heterogeneity in morphology and adhesive properties in populations derived from patients homozygous for 9p21 SNPs. Because VSMCs exhibit phenotypic plasticity, and dedifferentiate from a quiescent, contractile phenotype to a more synthetic one during CAD, we first investigated whether this increased heterogeneity was due to the increased presence of the synthetic, disease associated phenotype. The contractile phenotype has greater integrin expression than the synthetic, so we postulated we could utilize differences in attachment to sort VSMC populations into synthetic and contractile phenotypic subpopulations using a microfluidic adhesion-based sorting platform.

We found that adhesion-based sorting of VSMCs allowed us to isolate subpopulations of weakly adherent (WA), synthetic and strongly adherent (SA) contractile, cells. RNA sequencing of our sorted populations revealed differential expression of ~2200 genes, which were associated with ontological terms relevant to synthetic and contractile phenotypes. Signaling by RhoA family of GTPases was a top signaling pathway that mapped to DEGs between different adhesive groups as well as in an isogenic comparison of RR and RR KO VSMCs. Notably, of the DEGs common between both adhesion and isogenic comparisons, 90% were co-regulated. RhoA signaling was downregulated in both WA compared to SA and RR compared to RR KO, suggesting it is downregulated in synthetic compared to contractile cells. The RhoA pathway, being an important mechanotransduction pathway for regulating the dynamic organization of the actin cytoskeleton, has previously been implicated in VSMC phenotypic switching[184,224,225], although usually in the context of an external stimuli rather than non-coding gene locus.

To investigate how SNPs at the 9p21 loci could lead to such transcriptomic and functional changes and heterogeneity, we investigated the expression of a long non coding RNA that overlaps with the region, ANRIL. Comparing the expression of both short and long isoforms of ANRIL, we found short, but not long isoforms, were overexpressed in both RR VSMCs compared to NN and RR KO haplotypes as well as WA compared to SA. This suggested that differential splicing within a single risk patient VSMC population could be responsible for the phenotypic heterogeneity we observed, exacerbating the synthetic phenotype for RR patients compared to NN and RR KO.

To confirm ANRIL, instead of other molecules downstream of the SNPs, were the cause of these phenotypic changes, we used a lentiviral system to deliver the short isoforms of ANRIL to RR KO cells. Intriguingly overexpression of both short isoforms, A11 and A12, reduced cellular contractility, expression of alpha smooth muscle actin, and adhesion strength, creating populations that could be sorted into WA, synthetic and SA, contractile phenotypes. These results are the first to suggest that heterogeneous expression of an alternatively spliced lncRNA regulates VSMC phenotype plasticity. ANRIL's variable penetrance in risk patient populations offers an explanation as to how vascular disease pathology may be variable in patients despite the elevated risk caused by this lncRNA.

In summary, this dissertation provides evidence for the value of cross disciplinary studies in which genetics and mechanical influence on cells are manipulated to identify new disease mechanisms that would not be realized when studies independently. In addition to highlighting studies in which both genetic and mechanical cues were either independently or jointly investigated, we provided a case study of a combinational approach, utilizing biophysical sorting and TALEN edited iPSC technology. This approach yielded novel insights into how a lncRNA exacerbates the synthetic, CAD associated phenotype of VSMCs through its heterogeneous expression, increasing risk for patients with disease associated SNPs with a variable penetrance. Such approaches have broad applicability and can also unveil key insights in other diseases for which genetic risk is appreciated but poorly understood.

REFERENCES

1. Allada, R. Genetics of Sleep in a Simple Model Organism: Drosophila. In *Principles and Practice of Sleep Medicine* vol. 5 151 (2011).

2. Martin, A.-M. Genetic and Hormonal Risk Factors in Breast Cancer. *J Natl Cancer Inst* **92**, 1126–1135 (2000).

3. Foulkes, W. D. Inherited Susceptibility to Common Cancers. *New England Journal of Medicine* **359**, 2143–2153 (2008).

4. Li, C. & Williams, S. M. Human Somatic Variation: It's Not Just for Cancer Anymore. *Curr Genet Med Rep* **1**, 212–218 (2013).

5. Rizzolo, P., Silvestri, V., Falchetti, M. & Ottini, L. Inherited and acquired alterations in development of breast cancer. *Application of Clinical Genetics* **4**, 145–158 (2011).

6. Barrangou, R. & Marraffini, L. A. CRISPR-cas systems: Prokaryotes upgrade to adaptive immunity. *Molecular Cell* vol. 54 234–244 Preprint at https://doi.org/10.1016/j.molcel.2014.03.011 (2014).

7. Gaj, T., Gersbach, C. A. & Barbas, C. F. ZFN, TALEN, and CRISPR/Cas-based methods for genome engineering. *Trends in Biotechnology* vol. 31 397–405 Preprint at https://doi.org/10.1016/j.tibtech.2013.04.004 (2013).

8. Nemudryi, A. A., Valetdinova, K. R., Medvedev, S. P. & Zakian, S. M. TALEN and CRISPR/Cas genome editing systems: Tools of discovery. *Acta Naturae* vol. 6 19–40 Preprint at https://doi.org/10.32607/20758251-2014-6-3-19-40 (2014).

9. Kim, Y.-G., Cha, J. & Chandrasegaran, S. *Hybrid restriction enzymes: Zinc finger fusions to Fok I cleavage domain (Flavobacterium okeanokoites/chimeric restriction endonuclease/protein engineering/recognition and cleavage domains)*. vol. 93 (1996).

10. Ma, N., Shan, Y., Liao, B., Kong, G., Wang, C., Huang, K., Zhang, H., Cai, X., Chen, S., Pei, D., Chen, N. & Pan, G. Factor-induced reprogramming and zinc finger nuclease-aided gene targeting cause different genome instability in β-thalassemia induced pluripotent stem cells (iPSCs). *Journal of Biological Chemistry* **290**, 12079–12089 (2015).

11. Method of the Year 2011. *Nature Methods* vol. 9 1 Preprint at https://doi.org/10.1038/nmeth.1852 (2012).

12. Adli, M. The CRISPR tool kit for genome editing and beyond. *Nature Communications* vol. 9 1–13 Preprint at https://doi.org/10.1038/s41467-018-04252-2 (2018).

13. The top 10 causes of death. https://www.who.int/news-room/fact-sheets/detail/the-top-10-causes-of-death.

14. Cassar, A., Holmes, D. R., Rihal, C. S. & Gersh, B. J. Chronic coronary artery disease: Diagnosis and management. in *Mayo Clinic Proceedings* vol. 84 1130–1146 (Elsevier Ltd, 2009).

15. Kessler, T., Erdmann, J. & Schunkert, H. Genetics of Coronary Artery Disease and Myocardial Infarction-2013. *Cardiovascular Genomics* **15**, 8 (2013).

16. Topol, E. J., Smith, J., Plow, E. F. & Wang, Q. K. Genetic susceptibility to myocardial infarction and coronary artery disease. *Hum Mol Genet* **15**, R117–R123 (2006).

17. Roberts, R. & Stewart, A. F. R. Genes and coronary artery disease: Where are we? *Journal of the American College of Cardiology* vol. 60 1715–1721 Preprint at https://doi.org/10.1016/j.jacc.2011.12.062 (2012).

18. Cambien, F. & Tiret, L. Genetics of cardiovascular diseases: from single mutations to the whole genome. *Circulation* **116**, 1714–24 (2007).

19. Schaub, M. A., Boyle, A. P., Kundaje, A., Batzoglou, S. & Snyder, M. Linking disease associations with regulatory information in the human genome. *Genome Res* **22**, 1748–1759 (2012).

20. Roberts, R. & Stewart, A. F. R. 9p21 and the genetic revolution for coronary artery disease. *Clinical Chemistry* vol. 58 104–112 Preprint at https://doi.org/10.1373/clinchem.2011.172759 (2012).

21. Samani, N. J. & Schunkert, H. Chromosome 9p21 and cardiovascular disease: the story unfolds. *Circulation. Cardiovascular genetics* vol. 1 81–84 Preprint at https://doi.org/10.1161/CIRCGENETICS.108.832527 (2008).

22. McPherson, R. Chromosome 9p21.3 locus for coronary artery disease: How little we know. *Journal of the American College of Cardiology* vol. 62 1382–1383 Preprint at https://doi.org/10.1016/j.jacc.2013.07.032 (2013).

23. lo Sardo, V., Chubukov, P., Ferguson, W., Kumar, A., Teng, E. L., Duran, M., Zhang, L., Cost, G., Engler, A. J., Urnov, F., Topol, E. J., Torkamani, A. & Baldwin, K. K. Unveiling the Role of the Most Impactful Cardiovascular Risk Locus through Haplotype Editing. *Cell* **175**, 1796-1810.e20 (2018).

24. Roura, S. & Bayes-Genis, A. Vascular dysfunction in idiopathic dilated cardiomyopathy. *Nature Reviews Cardiology* vol. 6 590–598 Preprint at https://doi.org/10.1038/nrcardio.2009.130 (2009).

25. Maron, B. J., Towbin, J. A., Thiene, G., Antzelevitch, C., Corrado, D., Arnett, D., Moss, A. J., Seidman, C. E. & Young, J. B. Contemporary definitions and

classification of the cardiomyopathies: An American Heart Association Scientific Statement from the Council on Clinical Cardiology, Heart Failure and Transplantation Committee; Quality of Care and Outcomes Research and Functional Genomics and Translational Biology Interdisciplinary Working Groups; and Council on Epidemiology and Prevention. *Circulation* **113**, 1807–1816 (2006).

26. Yang, C., Al-Aama, J., Stojkovic, M., Keavney, B., Trafford, A., Lako, M. & Armstrong, L. Concise Review: Cardiac Disease Modeling Using Induced Pluripotent Stem Cells. *Stem Cells* **33**, 2643–2651 (2015).

27. Guo, G., Chen, L., Rao, M., Chen, K., Song, J. & Hu, S. A modified method for isolation of human cardiomyocytes to model cardiac diseases. *J Transl Med* **16**, 288 (2018).

28. Sun, N., Yazawa, M., Liu, J., Han, L., Sanchez-Freire, V., Abilez, O. J., Navarrete, E. G., Hu, S., Wang, L., Lee, A., Pavlovic, A., Lin, S., Chen, R., Hajjar, R. J., Snyder, M. P., Dolmetsch, R. E., … Wu, J. C. Patient-specific induced pluripotent stem cells as a model for familial dilated cardiomyopathy. *Sci Transl Med* **4**, 130ra47-130ra47 (2012).

29. Sehnert, A. J., Huq, A., Weinstein, B. M., Walker, C., Fishman, M. & Stainier, D. Y. R. Cardiac troponin T is essential in sarcomere assembly and cardiac contractility. *Nat Genet* **31**, 106–110 (2002).

30. Yamamoto, Y., Makiyama, T., Harita, T., Sasaki, K., Wuriyanghai, Y., Hayano, M., Nishiuchi, S., Kohjitani, H., Hirose, S., Chen, J., Yokoi, F., Ishikawa, T., Ohno, S., Chonabayashi, K., Motomura, H., Yoshida, Y., … Kimura, T. Allele-specific ablation rescues electrophysiological abnormalities in a human iPS cell model of long-QT syndrome with a CALM2 mutation. *Hum Mol Genet* **26**, 1670–1677 (2017).

31. Hashem, S. I., Perry, C. N., Bauer, M., Han, S., Clegg, S. D., Ouyang, K., Deacon, D. C., Spinharney, M., Panopoulos, A. D., Izpisua Belmonte, J. C., Frazer, K. A., Chen, J., Gong, Q., Zhou, Z., Chi, N. C. & Adler, E. D. Brief Report: Oxidative Stress Mediates Cardiomyocyte Apoptosis in a Human Model of Danon Disease and Heart Failure. *Stem Cells* **33**, 2343–2350 (2015).

32. Deacon, D. C., Happe, C. L., Chen, C., Tedeschi, N., Manso, A. M., Li, T., Dalton, N. D., Peng, Q., Farah, E. N., Gu, Y., Tenerelli, K. P., Tran, V. D., Chen, J., Peterson, K. L., Schork, N. J., Adler, E. D., … Chi, N. C. Combinatorial interactions of genetic variants in human cardiomyopathy. *Nat Biomed Eng* **3**, 147–157 (2019).

33. Peng, X., Nelson, E. S., Maiers, J. L. & DeMali, K. A. New Insights into Vinculin Function and Regulation. in *International Review of Cell and Molecular Biology* vol. 287 191–231 (Elsevier Inc., 2011).

34. Beri, P., Popravko, A., Yeoman, B., Kumar, A., Chen, K., Hodzic, E., Chiang, A., Banisadr, A., Placone, J. K., Carter, H., Fraley, S. I., Katira, P. & Engler, A. J. Cell Adhesiveness Serves as a Biophysical Marker for Metastatic Potential. (2020) doi:10.1158/0008-5472.CAN-19-1794.

35. Baugh, E. H., Ke, H., Levine, A. J., Bonneau, R. A. & Chan, C. S. Why are there hotspot mutations in the TP53 gene in human cancers? *Cell Death and Differentiation* vol. 25 154–160 Preprint at https://doi.org/10.1038/cdd.2017.180 (2018).

36. Dawson, P. J., Wolman, S. R., Tait, L., Heppner, G. H. & Miller, F. R. MCF10AT: A model for the evolution of cancer from proliferate breast disease. *American Journal of Pathology* **148**, 313–319 (1996).

37. Kraning-Rush, C. M., Califano, J. P. & Reinhart-King, C. A. Cellular Traction Stresses Increase with Increasing Metastatic Potential. *PLoS One* **7**, e32572 (2012).

38. Liu, Z., Tan, J. L., Cohen, D. M., Yang, M. T., Sniadecki, N. J., Ruiz, S. A., Nelson, C. M. & Chen, C. S. Mechanical tugging force regulates the size of cell-cell junctions. *Proc Natl Acad Sci U S A* **107**, 9944–9949 (2010).

39. Gkretsi, V. & Stylianopoulos, T. Cell Adhesion and Matrix Stiffness: Coordinating Cancer Cell Invasion and Metastasis. *Front Oncol* **8**, (2018).

40. Runge, J., Reichert, T., Fritsch, A., Käs, J., Bertolini, J. & Remmerbach, T. Evaluation of single-cell biomechanics as potential marker for oral squamous cell carcinomas: a pilot study. *Oral Dis* **20**, e120–e127 (2014).

41. Lherbette, M., Santos, Á. dos, Hari-Gupta, Y., Fili, N., Toseland, C. P. & Schaap, I. A. T. Atomic Force Microscopy micro-rheology reveals large structural inhomogeneities in single cell-nuclei OPEN. doi:10.1038/s41598-017-08517-6.

42. Zink, D., Fischer, A. H. & Nickerson, J. A. Nuclear structure in cancer cells. *Nature Reviews Cancer* vol. 4 677–687 Preprint at https://doi.org/10.1038/nrc1430 (2004).

43. Gill, N. K., Ly, C., Nyberg, K. D., Lee, L., Qi, D., Tofig, B., Reis-Sobreiro, M., Dorigo, O., Rao, J. Y., Wiedemeyer, R., Karlan, B., Lawrenson, K., Freeman, M. R., Damoiseaux, R. & Rowat, A. C. A scalable filtration method for high throughput screening based on cell deformability. *Lab Chip* **19**, 343–357 (2019).

44. Han, X., Liu, Z., Zhao, L., Wang, F., Yu, Y., Yang, J., Chen, R. & Qin, L. Microfluidic Cell Deformability Assay for Rapid and Efficient Kinase Screening with the CRISPR-Cas9 System. *Angewandte Chemie International Edition* **55**, 8561–8565 (2016).

45. Zhan, T., Rindtorff, N., Betge, J., Ebert, M. P. & Boutros, M. CRISPR/Cas9 for cancer research and therapy. *Seminars in Cancer Biology* vol. 55 106–119 Preprint at https://doi.org/10.1016/j.semcancer.2018.04.001 (2019).

46. Shen, J. P., Zhao, D., Sasik, R., Luebeck, J., Birmingham, A., Bojorquez-Gomez, A., Licon, K., Klepper, K., Pekin, D., Beckett, A. N., Sanchez, K. S., Thomas, A., Kuo, C. C., Du, D., Roguev, A., Lewis, N. E., … Mali, P. Combinatorial CRISPR-Cas9 screens for de novo mapping of genetic interactions. *Nat Methods* **14**, 573–576 (2017).

47. Chu, Y.-S., Thomas, W. A., Eder, O., Pincet, F., Perez, E., Paul Thiery, J. & Dufour, S. Force measurements in E-cadherin-mediated cell doublets reveal rapid adhesion strengthened by actin cytoskeleton remodeling through Rac and Cdc42. *J Cell Biol* **167**, 1183–1194 (2004).

48. Panorchan, P., Thompson, M. S., Davis, K. J., Tseng, Y., Konstantopoulos, K. & Wirtz, D. Single-molecule analysis of cadherin-mediated cell-cell adhesion. *J Cell Sci* **119**, 66–74 (2006).

49. Sancho, A., Vandersmissen, I., Craps, S., Luttun, A. & Groll, J. A new strategy to measure intercellular adhesion forces in mature cell-cell contacts. *Sci Rep* **7**, 1–14 (2017).

50. Puech, P. H., Poole, K., Knebel, D. & Muller, D. J. A new technical approach to quantify cell-cell adhesion forces by AFM. *Ultramicroscopy* **106**, 637–644 (2006).

51. Baumgartner, W., Hinterdorfer, P., Ness, W., Raab, A., Vestweber, D., Schindler, H. & Drenckhahn, D. *Cadherin interaction probed by atomic force microscopy*. www.pnas.org.

52. Buchanan, C. F., Verbridge, S. S., Vlachos, P. P. & Rylander, M. N. Flow shear stress regulates endothelial barrier function and expression of angiogenic factors in a 3D microfluidic tumor vascular model. *Cell Adh Migr* **8**, 517–524 (2014).

53. Polacheck, W. J., Kutys, M. L., Yang, J., Eyckmans, J., Wu, Y., Vasavada, H., Hirschi, K. K. & Chen, C. S. A non-canonical Notch complex regulates adherens junctions and vascular barrier function. *Nature* **552**, 258–262 (2017).

54. Ivanovska, I., Swift, J., Harada, T., Pajerowski, J. D. & Discher, D. E. Physical Plasticity of the Nucleus and its Manipulation. *Methods Cell Biol* **98**, 207–220 (2010).

55. Baumgartner, W., Schütz, G. J., Wiegand, J., Golenhofen, N. & Drenckhahn, D. Cadherin function probed by laser tweezer and single molecule fluorescence in vascular endothelial cells. *Journal of Cell Science* vol. 116 1001–1011 Preprint at https://doi.org/10.1242/jcs.00322 (2003).

56. Grashoff, C., Hoffman, B. D., Brenner, M. D., Zhou, R., Parsons, M., Yang, M. T., McLean, M. A., Sligar, S. G., Chen, C. S., Ha, T. & Schwartz, M. A. Measuring mechanical tension across vinculin reveals regulation of focal adhesion dynamics. *Nature* **466**, 263–266 (2010).

57. Jhon, M. S. & Andrade, J. D. Water and hydrogels. *J Biomed Mater Res* **7**, 509–522 (1973).

58. Zhu, J. & Marchant, R. E. Design properties of hydrogel tissue-engineering scaffolds. *Expert Rev Med Devices* **8**, 607–626 (2011).

59. Lee, K. Y., Rowley, J. A., Eiselt, P., Moy, E. M., Bouhadir, K. H. & Mooney, D. J. Controlling mechanical and swelling properties of alginate hydrogels independently by cross-linker type and cross-linking density. *Macromolecules* **33**, 4291–4294 (2000).

60. Jiang, Z., Bhaskaran, A., Aitken, H. M., Shackleford, I. C. G. & Connal, L. A. Using Synergistic Multiple Dynamic Bonds to Construct Polymers with Engineered Properties. *Macromol Rapid Commun* **40**, 1900038 (2019).

61. Kai, F. B., Laklai, H. & Weaver, V. M. Force Matters: Biomechanical Regulation of Cell Invasion and Migration in Disease. *Trends in Cell Biology* vol. 26 486–497 Preprint at https://doi.org/10.1016/j.tcb.2016.03.007 (2016).

62. Pelham, R. J. & Wang, Y. L. Cell locomotion and focal adhesions are regulated by substrate flexibility. *Proc Natl Acad Sci U S A* **94**, 13661–13665 (1997).

63. Lo, C. M., Wang, H. B., Dembo, M. & Wang, Y. L. Cell movement is guided by the rigidity of the substrate. *Biophys J* **79**, 144–152 (2000).

64. Acerbi, I., Cassereau, L., Dean, I., Shi, Q., Au, A., Park, C., Chen, Y. Y., Liphardt, J., Hwang, E. S. & Weaver, V. M. Human breast cancer invasion and aggression correlates with ECM stiffening and immune cell infiltration. *Integrative Biology* **7**, 1120–1134 (2015).

65. Voutouri, C., Mpekris, F., Papageorgis, P., Odysseos, A. D., Stylianopoulos, T. & Singh, P. K. Role of Constitutive Behavior and Tumor-Host Mechanical Interactions in the State of Stress and Growth of Solid Tumors. (2014) doi:10.1371/journal.pone.0104717.

66. Kohn, J. C., Zhou, D. W., Bordeleau, F., Zhou, A. L., Mason, B. N., Mitchell, M. J., King, M. R. & Reinhart-King, C. A. Cooperative effects of matrix stiffness and fluid shear stress on endothelial cell behavior. *Biophys J* **108**, 471–478 (2015).

67. Cavo, M., Fato, M., Peñuela, L., Beltrame, F., Raiteri, R. & Scaglione, S. Microenvironment complexity and matrix stiffness regulate breast cancer cell activity in a 3D in vitro model. *Sci Rep* **6**, 1–13 (2016).

68. Lang, N. R., Skodzek, K., Hurst, S., Mainka, A., Steinwachs, J., Schneider, J., Aifantis, K. E. & Fabry, B. Biphasic response of cell invasion to matrix stiffness in three-dimensional biopolymer networks. *Acta Biomater* **13**, 61–67 (2015).

69. Wei, S. C., Fattet, L., Tsai, J. H., Guo, Y., Pai, V. H., Majeski, H. E., Chen, A. C., Sah, R. L., Taylor, S. S., Engler, A. J. & Yang, J. Matrix stiffness drives epithelial-mesenchymal transition and tumour metastasis through a TWIST1-G3BP2 mechanotransduction pathway. *Nat Cell Biol* **17**, 678–688 (2015).

70. Ondeck, Matthew G.; Kumar, Aditya; Placone, Jesse K.; Plunkett,Christopher M.; Matte, Bibiana F.;Wong, Kirsten C.; Fattet, Laurent; Yang, Jing,; and Engler, A. J. Dynamically stiffened matrix promotes malignant transformation of mammary epithelial cells via collective mechanical signaling contributed new reagents/analytic tools. *PNAS* **11**, 3502–3507 (2019).

71. Jung, H. Y., Fattet, L., Tsai, J. H., Kajimoto, T., Chang, Q., Newton, A. C. & Yang, J. Apical–basal polarity inhibits epithelial–mesenchymal transition and tumour metastasis by PAR-complex-mediated SNAI1 degradation. *Nat Cell Biol* **21**, 359–371 (2019).

72. Tilghman, R. W., Cowan, C. R., Mih, J. D., Koryakina, Y., Gioeli, D., Slack-Davis, J. K., Blackman, B. R., Tschumperlin, D. J. & Parsons, J. T. Matrix rigidity regulates cancer cell growth and cellular phenotype. *PLoS One* **5**, (2010).

73. Yangben, Y., Wang, H., Zhong, L., Chiang, M. Y. M., Tan, Q., Singh, G. K., Li, S. & Yang, L. Relative Rigidity of Cell–Substrate Effects on Hepatic and Hepatocellular Carcinoma Cell Migration. *J Biomater Sci Polym Ed* **24**, 148–157 (2013).

74. Moazzem Hossain, M., Wang, X., Bergan, R. C. & Jin, J. P. Diminished expression of h2-calponin in prostate cancer cells promotes cell proliferation, migration and the dependence of cell adhesion on substrate stiffness. *FEBS Open Bio* **4**, 627–636 (2014).

75. Matte, B. F., Kumar, A., Placone, J. K., Zanella, V. G., Martins, M. D., Engler, A. J. & Lamers, M. L. Matrix stiffness mechanically conditions EMT and migratory behavior of oral squamous cell carcinoma. *Journal of Cell Science* vol. 132 Preprint at https://doi.org/10.1242/jcs.224360 (2019).

76. Nasrollahi, S., Walter, C., Loza, A. J., Schimizzi, G. v., Longmore, G. D. & Pathak, A. Past matrix stiffness primes epithelial cells and regulates their future collective migration through a mechanical memory. *Biomaterials* **146**, 146–155 (2017).

77. Tang, X., Kuhlenschmidt, T. B., Li, Q., Ali, S., Lezmi, S., Chen, H., Pires-Alves, M., Laegreid, W. W., Saif, T. A. & Kuhlenschmidt, M. S. A

mechanically-induced colon cancer cell population shows increased metastatic potential. *Mol Cancer* **13**, 131 (2014).

78. Charrier, E. E., Pogoda, K., Wells, R. G. & Janmey, P. A. Control of cell morphology and differentiation by substrates with independently tunable elasticity and viscous dissipation. *Nat Commun* **9**, 449 (2018).

79. Levental, I., Levental, K. R., Klein, E. A., Assoian, R., Miller, R. T., Wells, R. G. & Janmey, P. A. A simple indentation device for measuring micrometer-scale tissue stiffness. *Journal of Physics: Condensed Matter* **22**, 194120 (2010).

80. Chaudhuri, O., Gu, L., Klumpers, D., Darnell, M., Bencherif, S. A., Weaver, J. C., Huebsch, N., Lee, H. P., Lippens, E., Duda, G. N. & Mooney, D. J. Hydrogels with tunable stress relaxation regulate stem cell fate and activity. *Nat Mater* **15**, 326–334 (2016).

81. Wisdom, K. M., Adebowale, K., Chang, J., Lee, J. Y., Nam, S., Desai, R., Rossen, N. S., Rafat, M., West, R. B., Hodgson, L. & Chaudhuri, O. Matrix mechanical plasticity regulates cancer cell migration through confining microenvironments. *Nat Commun* **9**, 1–13 (2018).

82. Lautscham, L. A., Lin, C. Y., Auernheimer, V., Naumann, C. A., Goldmann, W. H. & Fabry, B. Biomembrane-mimicking lipid bilayer system as a mechanically tunable cell substrate. *Biomaterials* **35**, 3198–3207 (2014).

83. Huang, N. F., Chaudhuri, O., Cahan, P., Wang, A., Engler, A. J., Wang, Y., Kumar, S., Khademhosseini, A. & Li, S. Multi-scale cellular engineering: From molecules to organ-on-a-chip. *APL Bioeng* **4**, 10906 (2020).

84. Günay, K. A., Ceccato, T. L., Silver, J. S., Bannister, K. L., Bednarski, O. J., Leinwand, L. A. & Anseth, K. S. PEG–Anthracene Hydrogels as an On-Demand Stiffening Matrix To Study Mechanobiology. *Angewandte Chemie International Edition* **58**, 9912–9916 (2019).

85. Marozas, I. A., Anseth, K. S. & Cooper-White, J. J. Adaptable boronate ester hydrogels with tunable viscoelastic spectra to probe timescale dependent mechanotransduction. *Biomaterials* **223**, 119430 (2019).

86. Kä, E., Delgado, S. M. & Kasko, A. M. Shape-Changing Photodegradable Hydrogels for Dynamic 3D Cell Culture. (2016) doi:10.1021/acsami.6b05527.

87. Wei, J. & Yu, Y. Photodeformable polymer gels and crosslinked liquid-crystalline polymers. *Soft Matter* vol. 8 8050–8059 Preprint at https://doi.org/10.1039/c2sm25474c (2012).

88. DuChez, B. J., Doyle, A. D., Dimitriadis, E. K. & Yamada, K. M. Durotaxis by Human Cancer Cells. *Biophys J* **116**, 670–683 (2019).

89. Louis, S. F. & Zahradka, P. Vascular smooth muscle cell motility: From migration to invasion. *Exp Clin Cardiol* **15**, e75 (2010).

90. Raab, M., Swift, J., Dingal, P. C. D. P., Shah, P., Shin, J. W. & Discher, D. E. Crawling from soft to stiff matrix polarizes the cytoskeleton and phosphoregulates myosin-II heavy chain. *Journal of Cell Biology* **199**, 669–683 (2012).

91. Frey, M. T. & Wang, Y. L. A photo-modulatable material for probing cellular responses to substrate rigidity. *Soft Matter* **5**, 1918–1924 (2009).

92. Kim, Jungwook ; Whang, M. Synthetic Hydrogels with Stiffness Gradients for Durotaxis Study and Tissue Engineering Scaffold. *Tissue Engineering Regenerative Medicine* **13**, 126–139 (2016).

93. Sunyer, R., Jin, A. J., Nossal, R. & Sackett, D. L. Fabrication of Hydrogels with Steep Stiffness Gradients for Studying Cell Mechanical Response. *PLoS One* **7**, e46107 (2012).

94. Kloxin, A. M., Kasko, A. M., Salinas, C. N. & Anseth, K. S. Photodegradable hydrogels for dynamic tuning of physical and chemical properties. *Science (1979)* **324**, 59–63 (2009).

95. Kaneko, S., Nakayama, H., Yoshino, Y., Fushimi, D., Yamaguchi, K., Horiike, Y. & Nakanishi, J. Photocontrol of cell adhesion on amino-bearing surfaces by reversible conjugation of poly(ethylene glycol) via a photocleavable linker. *Physical Chemistry Chemical Physics* **13**, 4051–4059 (2011).

96. Marklein, R. A. & Burdick, J. A. Spatially controlled hydrogel mechanics to modulate stem cell interactions. *Soft Matter* **6**, 136–143 (2009).

97. Diederich, V. E. G., Studer, P., Kern, A., Lattuada, M., Storti, G., Sharma, R. I., Snedeker, J. G. & Morbidelli, M. Bioactive polyacrylamide hydrogels with gradients in mechanical stiffness. *Biotechnol Bioeng* **110**, 1508–1519 (2013).

98. Burdick, J. A., Khademhosseini, A. & Langer, R. Fabrication of gradient hydrogels using a microfluidics/photopolymerization process. *Langmuir* **20**, 5153–5156 (2004).

99. Zaari, N., Rajagopalan, P., Kim, S. K., Engler, A. J. & Wong, J. Y. Photopolymerization in microfluidic gradient generators: Microscale control of substrate compliance to manipulate cell response. *Advanced Materials* **16**, 2133–2137 (2004).

100. Rao, N., Grover, G. N., Vincent, L. G., Evans, S. C., Choi, Y. S., Spencer, K. H., Hui, E. E., Engler, A. J. & Christman, K. L. A co-culture device with a tunable stiffness to understand combinatorial cell-cell and cell-matrix interactions. *Integrative Biology (United Kingdom)* **5**, 1344–1354 (2013).

101. Maloney, J. M., Walton, E. B., Bruce, C. M. & van Vliet, K. J. Influence of finite thickness and stiffness on cellular adhesion-induced deformation of compliant substrata. doi:10.1103/PhysRevE.78.041923.

102. Choi, Y. S., Vincent, L. G., Lee, A. R., Kretchmer, K. C., Chirasatitsin, S., Dobke, M. K. & Engler, A. J. The alignment and fusion assembly of adipose-derived stem cells on mechanically patterned matrices. *Biomaterials* **33**, 6943–6951 (2012).

103. Kuo, C.-H. R., Xian, J., Brenton, J. D., Franze, K. & Sivaniah, E. Complex Stiffness Gradient Substrates for Studying Mechanotactic Cell Migration. *Advanced Materials* **24**, 6059–6064 (2012).

104. Gray, D. S., Tien, J. & Chen, C. S. Repositioning of cells by mechanotaxis on surfaces with micropatterned Young's modulus. *J Biomed Mater Res* **66A**, 605–614 (2003).

105. Isenberg, B. C., DiMilla, P. A., Walker, M., Kim, S. & Wong, J. Y. Vascular smooth muscle cell durotaxis depends on substrate stiffness gradient strength. *Biophys J* **97**, 1313–1322 (2009).

106. Wong, J. Y., Velasco, A., Rajagopalan, P. & Pham, Q. Directed Movement of Vascular Smooth Muscle Cells on Gradient-Compliant Hydrogels †. (2003) doi:10.1021/la026403p.

107. Happe, C. L., Tenerelli, K. P., Gromova, A. K., Kolb, F. & Engler, A. J. Mechanically patterned neuromuscular junctionsina-dish have improved functional maturation. *Mol Biol Cell* **28**, 1950–1958 (2017).

108. Cullen, D. K., Lessing, M. C. & Laplaca, M. C. Collagen-dependent neurite outgrowth and response to dynamic deformation in three-dimensional neuronal cultures. *Ann Biomed Eng* **35**, 835–846 (2007).

109. Smeal, R. M., Rabbitt, R., Biran, R. & Tresco, P. A. Substrate Curvature Influences the Direction of Nerve Outgrowth. *Ann Biomed Eng* **33**, 376–382 (2005).

110. Qiu, J., Zheng, Y., Hu, J., Liao, D., Gregersen, H., Deng, X., Fan, Y. & Wang, G. Biomechanical regulation of vascular smooth muscle cell functions: From in vitro to in vivo understanding. *J R Soc Interface* **11**, (2014).

111. Janmey, P. A., Winer, J. P. & Weisel, J. W. Fibrin gels and their clinical and bioengineering applications. *Journal of the Royal Society Interface* vol. 6 1–10 Preprint at https://doi.org/10.1098/rsif.2008.0327 (2009).

112. Barnes, C. P., Sell, S. A., Boland, E. D., Simpson, D. G. & Bowlin, G. L. Nanofiber technology: Designing the next generation of tissue engineering

scaffolds. *Advanced Drug Delivery Reviews* vol. 59 1413–1433 Preprint at https://doi.org/10.1016/j.addr.2007.04.022 (2007).

113. Lannutti, J., Reneker, D., Ma, T., Tomasko, D. & Farson, D. Electrospinning for tissue engineering scaffolds. *Materials Science and Engineering: C* **27**, 504–509 (2007).

114. Huang, Z. M., Zhang, Y. Z., Kotaki, M. & Ramakrishna, S. A review on polymer nanofibers by electrospinning and their applications in nanocomposites. *Compos Sci Technol* **63**, 2223–2253 (2003).

115. Pham, Q. S. U. and M. A. G. *Electrospinning of Polymeric Nanofibers for Tissue Engineering Applications: A Review*. *Tissue Engineering* www.liebertpub.com (2006).

116. Tan, A. R., Ifkovits, J. L., Baker, B. M., Brey, D. M., Mauck, R. L. & Burdick, J. A. Electrospinning of photocrosslinked and degradable fibrous scaffolds. *J Biomed Mater Res A* **87**, 1034–1043 (2008).

117. Xue, J., Wu, T. & Xia, Y. Perspective: Aligned arrays of electrospun nanofibers for directing cell migration. *APL Mater* **6**, 120902 (2018).

118. Hodgkinson, T., Yuan, X.-F. & Bayat, A. Electrospun silk fibroin fiber diameter influences in vitro dermal fibroblast behavior and promotes healing of ex vivo wound models. *J Tissue Eng* **5**, 204173141455166 (2014).

119. Heller, M., Bauer, H.-K., Goetze, E., Gielisch, M., Roth, K. E., Drees, P., Maier, G. S., Dorweiler, B., Ghazy, A., Neufurth, M., Müller, W. E. G., Schröder, H. C., Wang, X., Vahl, C.-F. & Al-Nawas, B. Applications of patient-specific 3D printing in medicine. *Int J Comput Dent* **19**, 323–339.

120. Jakus, A. E., Rutz, A. L. & Shah, R. N. Advancing the field of 3D biomaterial printing. *Biomedical Materials* **11**, 014102 (2016).

121. Bose, S., Vahabzadeh, S. & Bandyopadhyay, A. Bone tissue engineering using 3D printing. *Materials Today* vol. 16 496–504 Preprint at https://doi.org/10.1016/j.mattod.2013.11.017 (2013).

122. Lee Ventola, C. Medical applications for 3D printing: Current and projected uses. *P and T* **39**, 704–711 (2014).

123. Vijayavenkataraman, S., Lu, W. F. & Fuh, J. Y. H. 3D bioprinting of functional human skin: production and in vivo analysis Related content 3D bioprinting of skin: a state-of-the-art review on modelling, materials, and processes. (2016) doi:10.1088/1758-5090/9/1/015006.

124. McBeth, C. ; L. J. O. M. C. J. S. A. and S.-B. A. F. 3D bioprinting of GelMA scaffolds triggers mineral deposition by primary human osteoblasts - IOPscience. *Biofabrication* **9**, (2017).

125. Fedorovich, N. E., Schuurman, W., Wijnberg, H. M., Prins, H. J., van Weeren, P. R., Malda, J., Alblas, J. & Dhert, W. J. A. Biofabrication of osteochondral tissue equivalents by printing topologically defined, cell-laden hydrogel scaffolds. *Tissue Eng Part C Methods* **18**, 33–44 (2012).

126. Bae, H., Puranik, A. S., Gauvin, R., Edalat, F., Carrillo-Conde, B., Peppas, N. A. & Khademhosseini, A. Building vascular networks. *Sci Transl Med* **4**, (2012).

127. Bertassoni, L. E., Cecconi, M., Manoharan, V., Nikkhah, M., Hjortnaes, J., Cristino, A. L., Barabaschi, G., Demarchi, D., Dokmeci, M. R., Yang, Y. & Khademhosseini, A. Hydrogel bioprinted microchannel networks for vascularization of tissue engineering constructs. *Lab Chip* **14**, 2202–2211 (2014).

128. Hu, M., Dailamy, A., Lei, Y., Parekh, U., Mcdonald, D., Kumar, A. & Mali, P. Facile Engineering of Long-Term Culturable Ex Vivo Vascularized Tissues Using Biologically Derived Matrices. (2018) doi:10.1002/adhm.201800845.

129. Venugopal Menon, N., Tay, H. M., Pang, K. T., Dalan, R., Wong, S. C., Wang, X., Li, K. H. H. & Hou, H. W. A tunable microfluidic 3D stenosis model to study leukocyte-endothelial interactions in atherosclerosis. *APL Bioeng* **2**, 016103 (2018).

130. Wong, A. K., LLanos, P., Boroda, N., Rosenberg, S. R. & Rabbany, S. Y. A Parallel-Plate Flow Chamber for Mechanical Characterization of Endothelial Cells Exposed to Laminar Shear Stress. *Cell Mol Bioeng* **9**, 127–138 (2016).

131. DePaola, N., Gimbrone, M. A., Davies, P. F. & Dewey, C. F. Vascular endothelium responds to fluid shear stress gradients. *Arteriosclerosis and Thrombosis* **12**, 1254–1257 (1992).

132. Wang, K. C., Yeh, Y. T., Nguyen, P., Limqueco, E., Lopez, J., Thorossian, S., Guan, K. L., Li, Y. S. J. & Chien, S. Flow-dependent YAP/TAZ activities regulate endothelial phenotypes and atherosclerosis. *Proc Natl Acad Sci U S A* **113**, 11525–11530 (2016).

133. Huang, Y., Wang, L., Luo, J. Y., Li, B., Tian, X. Y., Chen, L. J., Huang, Y., Liu, J., Deng, D., Lau, C. W., Wan, S., Ai, Di., Mak, K. L. K., Tong, K. K., Kwan, K. M., Wang, N., … Zhu, Y. Integrin-YAP/TAZ-JNK cascade mediates atheroprotective effect of unidirectional shear flow. *Nature 2016 540:7634* **540**, 579–582 (2016).

134. Yeom, E., Park, J. H., Kang, Y. J. & Lee, S. J. Microfluidics for simultaneous quantification of platelet adhesion and blood viscosity. *Sci Rep* **6**, 1–11 (2016).

135. Sugimura, K., Lenne, P. F. & Graner, F. Measuring forces and stresses in situ in living tissues. *Development (Cambridge)* **143**, 186–196 (2016).

136. Heer, N. C. & Martin, A. C. Tension, contraction and tissue morphogenesis. *Development (Cambridge)* vol. 144 4249–4260 Preprint at https://doi.org/10.1242/dev.151282 (2017).

137. Needleman, D. & Dogic, Z. Active matter at the interface between materials science and cell biology. *Nature Reviews Materials* vol. 2 1–14 Preprint at https://doi.org/10.1038/natrevmats.2017.48 (2017).

138. van Engeland, N. C. A., Pollet, A. M. A. O., den Toonder, J. M. J., Bouten, C. V. C., Stassen, O. M. J. A. & Sahlgren, C. M. A biomimetic microfluidic model to study signalling between endothelial and vascular smooth muscle cells under hemodynamic conditions. *Lab Chip* **18**, 1607–1620 (2018).

139. Cicha, I., Urschel, K., Daniel, W. G. & Garlichs, C. D. Telmisartan prevents VCAM-1 induction and monocytic cell adhesion to endothelium exposed to non-uniform shear stress and TNF-α. *Clin Hemorheol Microcirc* **48**, 65–73 (2011).

140. Simonds, N. I., Ghazarian, A. A., Pimentel, C. B., Schully, S. D., Ellison, G. L., Gillanders, E. M. & Mechanic, L. E. Review of the Gene-Environment Interaction Literature in Cancer: What Do We Know? *Genet Epidemiol* **40**, 356–365 (2016).

141. Boffetta, P., Winn, D. M., Ioannidis, J. P., Thomas, D. C., Little, J., Smith, G. D., Cogliano, V. J., Hecht, S. S., Seminara, D., Vineis, P. & Khoury, M. J. Recommendations and proposed guidelines for assessing the cumulative evidence on joint effects of genes and environments on cancer occurrence in humans. *Int J Epidemiol* **41**, 686–704 (2012).

142. Thomas, D. Gene-environment-wide association studies: Emerging approaches. *Nature Reviews Genetics* vol. 11 259–272 Preprint at https://doi.org/10.1038/nrg2764 (2010).

143. Hunter, D. J. Gene-environment interactions in human diseases. *Nature Reviews Genetics* vol. 6 287–298 Preprint at https://doi.org/10.1038/nrg1578 (2005).

144. Giral, H., Landmesser, U. & Kratzer, A. Into the Wild: GWAS Exploration of Non-coding RNAs. *Frontiers in Cardiovascular Medicine* vol. 5 181 Preprint at https://doi.org/10.3389/fcvm.2018.00181 (2018).

145. Frayling, T. M. Genome-wide association studies: The good, the bad and the ugly. *Clinical Medicine, Journal of the Royal College of Physicians of London* vol. 14 428–431 Preprint at https://doi.org/10.7861/clinmedicine.14-4-428 (2014).

146. Belair, D. G., Whisler, J. A., Valdez, J., Velazquez, J., Molenda, J. A., Vickerman, V., Lewis, R., Daigh, C., Hansen, T. D., Mann, D. A., Thomson, J. A., Griffith, L. G., Kamm, R. D., Schwartz, M. P. & Murphy, W. L. Human Vascular Tissue Models Formed from Human Induced Pluripotent Stem Cell Derived Endothelial Cells. *Stem Cell Rev Rep* **11**, 511–525 (2015).

147. Kurokawa, Y. K., Yin, R. T., Shang, M. R., Shirure, V. S., Moya, M. L. & George, S. C. Human Induced Pluripotent Stem Cell-Derived Endothelial Cells for Three-Dimensional Microphysiological Systems. *Tissue Eng Part C Methods* **23**, 474–484 (2017).

148. Vazão, H., Rosa, S., Barata, T., Costa, R., Pitrez, P. R., Honório, I., de Vries, M. R., Papatsenko, D., Benedito, R., Saris, D., Khademhosseini, A., Quax, P. H. A., Pereira, C. F., Mercader, N., Fernandes, H. & Ferreira, L. High-throughput identification of small molecules that affect human embryonic vascular development. doi:10.1073/pnas.1617451114.

149. Dash, B. C., Levi, K., Schwan, J., Luo, J., Bartulos, O., Wu, H., Qiu, C., Yi, T., Ren, Y., Campbell, S., Rolle, M. W. & Qyang, Y. Tissue-Engineered Vascular Rings from Human iPSC-Derived Smooth Muscle Cells. *Stem Cell Reports* **7**, 19–28 (2016).

150. Ge, X., Ren, Y., Bartulos, O., Lee, M. Y., Yue, Z., Kim, K. Y., Li, W., Amos, P. J., Bozkulak, E. C., Iyer, A., Zheng, W., Zhao, H., Martin, K. A., Kotton, D. N., Tellides, G., Park, I. H., … Qyang, Y. Modeling supravalvular aortic stenosis syndrome with human induced pluripotent stem cells. *Circulation* **126**, 1695–1704 (2012).

151. Sundaram, S., One, J., Siewert, J., Teodosescu, S., Zhao, L., Dimitrievska, S., Qian, H., Huang, A. H. & Niklason, L. Tissue-Engineered Vascular Grafts Created From Human Induced Pluripotent Stem Cells. *Stem Cells Transl Med* **3**, 1535–1543 (2014).

152. Karamariti, E., Margariti, A., Winkler, B., Wang, X., Hong, X., Baban, D., Ragoussis, J., Huang, Y., Han, J. D. J., Wong, M. M., Sag, C. M., Shah, A. M., Hu, Y. & Xu, Q. Smooth muscle cells differentiated from reprogrammed embryonic lung fibroblasts through dkk3 signaling are potent for tissue engineering of vascular grafts. *Circ Res* **112**, 1433–1443 (2013).

153. Scaffidi, P. & Misteli, T. Reversal of the cellular phenotype in the premature aging disease Hutchinson-Gilford progeria syndrome. *Nat Med* **11**, 440–445 (2005).

154. Atchison, L., Zhang, H., Cao, K. & Truskey, G. A. A Tissue Engineered Blood Vessel Model of Hutchinson-Gilford Progeria Syndrome Using Human iPSC-derived Smooth Muscle Cells. *Sci Rep* **7**, 1–12 (2017).

155. Ribas, J., Zhang, Y. S., Pitrez, P. R., Leijten, J., Miscuglio, M., Rouwkema, J., Dokmeci, M. R., Nissan, X., Ferreira, L. & Khademhosseini, A. Biomechanical Strain Exacerbates Inflammation on a Progeria-on-a-Chip Model. *Small* **13**, 1603737 (2017).

156. Atchison, L., Abutaleb, N. O., Snyder-Mounts, E., Gete, Y., Ladha, A., Ribar, T., Cao, K. & Truskey, G. A. iPSC-Derived Endothelial Cells Affect Vascular Function in a Tissue-Engineered Blood Vessel Model of Hutchinson-Gilford Progeria Syndrome. *Stem Cell Reports* **14**, 325–337 (2020).

157. Hinson, J. T., Chopra, A., Nafissi, N., Polacheck, W. J., Benson, C. C., Swist, S., Gorham, J., Yang, L., Schafer, S., Sheng, C. C., Haghighi, A., Homsy, J., Hubner, N., Church, G., Cook, S. A., Linke, W. A., … Seidman, C. E. Titin mutations in iPS cells define sarcomere insufficiency as a cause of dilated cardiomyopathy. *Science (1979)* **349**, 982–986 (2015).

158. Kumar, A., Thomas, S. K., Wong, K. C., lo Sardo, V., Cheah, D. S., Hou, Y. H., Placone, J. K., Tenerelli, K. P., Ferguson, W. C., Torkamani, A., Topol, E. J., Baldwin, K. K. & Engler, A. J. Mechanical activation of noncoding-RNA-mediated regulation of disease-associated phenotypes in human cardiomyocytes. *Nat Biomed Eng* **3**, 137–146 (2019).

159. Mucci, L. A., Hjelmborg, J. B., Harris, J. R., Czene, K., Havelick, D. J., Scheike, T., Graff, R. E., Holst, K., Möller, S., Unger, R. H., McIntosh, C., Nuttall, E., Brandt, I., Penney, K. L., Hartman, M., Kraft, P., … Halekoh, U. Familial risk and heritability of cancer among twins in nordic countries. *JAMA - Journal of the American Medical Association* **315**, 68–76 (2016).

160. Aul, P., Ichtenstein, L., Olm, I. V. H., Erkasalo, I. K. v, Nastasia, A., Liadou, I., Aakko, J., Aprio, K., Arkku, M., Oskenvuo, K., Ero, E., Ukkala, P., Xel, A., Kytthe, S., Ari, K. & Emminki, H. *The New England Journal of Medicine ENVIRONMENTAL AND HERITABLE FACTORS IN THE CAUSATION OF CANCER Analyses of Cohorts of Twins from Sweden, Denmark, and Finland A BSTRACT Background The contribution of hereditary factors*. *J U L Y* vol. 343 (2000).

161. Rudolph, A., Chang-Claude, J. & Schmidt, M. K. Gene-environment interaction and risk of breast cancer. *British Journal of Cancer* vol. 114 125–133 Preprint at https://doi.org/10.1038/bjc.2015.439 (2016).

162. Wong, S. Y., Ulrich, T. A., Deleyrolle, L. P., MacKay, J. L., Lin, J. M. G., Martuscello, R. T., Jundi, M. A., Reynolds, B. A. & Kumar, S. Constitutive activation of myosin-dependent contractility sensitizes glioma tumor-initiating

cells to mechanical inputs and reduces tissue invasion. *Cancer Res* **75**, 1113–1122 (2015).

163. Wang, H. B., Dembo, M. & Wang, Y. L. Substrate flexibility regulates growth and apoptosis of normal but not transformed cells. *Am J Physiol Cell Physiol* **279**, (2000).

164. Nardone, G., Oliver-De La Cruz, J., Vrbsky, J., Martini, C., Pribyl, J., Skládal, P., Pešl, M., Caluori, G., Pagliari, S., Martino, F., Maceckova, Z., Hajduch, M., Sanz-Garcia, A., Pugno, N. M., Stokin, G. B. & Forte, G. YAP regulates cell mechanics by controlling focal adhesion assembly. *Nat Commun* **8**, 1–13 (2017).

165. Meng, Z., Qiu, Y., Lin, K. C., Kumar, A., Placone, J. K., Fang, C., Wang, K.-C., Lu, S., Pan, M., Hong, A. W., Moroishi, T., Luo, M., Plouffe, S. W., Diao, Y., Ye, Z., Park, H. W., … Guan, K.-L. RAP2 mediates mechanoresponses of the Hippo pathway. *Nature* **560**, 655–660 (2018).

166. Plunkett, C., Kumar, A., Yrastorza, J., Hou, Y., Placone, J. K., Grennan, G. & Engler, A. J. H-Ras Transformation of Mammary Epithelial Cells Induces ERK-Mediated Spreading on Low Stiffness Matrix. *Adv Healthc Mater* 1901366 (2020) doi:10.1002/adhm.201901366.

167. Kumar, A., Thomas, S. K., Wong, K. C., lo Sardo, V., Cheah, D. S., Hou, Y. H., Placone, J. K., Tenerelli, K. P., Ferguson, W. C., Torkamani, A., Topol, E. J., Baldwin, K. K. & Engler, A. J. Mechanical activation of noncoding-RNA-mediated regulation of disease-associated phenotypes in human cardiomyocytes. *Nat Biomed Eng* **3**, 137–146 (2019).

168. CDC. Heart Disease Facts & Statistics | cdc.gov. https://www.cdc.gov/heartdisease/facts.htm.

169. Helgadottir, A., Thorleifsson, G., Manolescu, A., Gretarsdottir, S., Blondal, T., Jonasdottir, A., Jonasdottir, A., Sigurdsson, A., Baker, A., Palsson, A., Masson, G., Gudbjartsson, D. F., Magnusson, K. P., Andersen, K., Levey, A. I., Backman, V. M., … Stefansson, K. A common variant on chromosome 9p21 affects the risk of myocardial infarction. *Science (1979)* **316**, 1491–1493 (2007).

170. Visel, A., Zhu, Y., May, D., Afzal, V., Gong, E., Attanasio, C., Blow, M. J., Cohen, J. C., Rubin, E. M. & Pennacchio, L. A. Targeted deletion of the 9p21 non-coding coronary artery disease risk interval in mice. *Nature* **464**, 409–412 (2010).

171. Folkersen, L., Kyriakou, T., Goel, A., Peden, J., Mälarstig, A., Paulsson-Berne, G., Hamsten, A., Franco-Cereceda, A., Gabrielsen, A. & Eriksson, P. Relationship between CAD Risk Genotype in the Chromosome 9p21 Locus

and Gene Expression. Identification of Eight New ANRIL Splice Variants. *PLoS One* **4**, e7677 (2009).

172. Louis, S. F. & Zahradka, P. Vascular smooth muscle cell motility: From migration to invasion. *Experimental and Clinical Cardiology* vol. 15 Preprint at (2010).

173. Ahmed, S. & Warren, D. T. Vascular smooth muscle cell contractile function and mechanotransduction. *Vessel Plus* **2**, 36 (2018).

174. Ross, R. The pathogenesis of atherosclerosis: a perspective for the 1990s. *Nature* (1993).

175. ZARGHAM, R. & THIBAULT, G. Alpha8Beta1 Integrin expression in the rat carotid artery: involvement in smooth muscle cell migration and neointima formation. *Cardiovasc Res* **65**, 813–822 (2005).

176. Bennett, M. R., Sinha, S. & Owens, G. K. Vascular Smooth Muscle Cells in Atherosclerosis. *Circ Res* **118**, 692–702 (2016).

177. Christen, T., Verin, V., Bochaton-Piallat, M. L., Popowski, Y., Ramaekers, F., Debruyne, P., Camenzind, E., van Eys, G. & Gabbiani, G. Mechanisms of neointima formation and remodeling in the porcine coronary artery. *Circulation* **103**, 882–888 (2001).

178. Basatemur, G. L., Jørgensen, H. F., Clarke, M. C. H., Bennett, M. R. & Mallat, Z. Vascular smooth muscle cells in atherosclerosis. *Nature Reviews Cardiology 2019 16:12* **16**, 727–744 (2019).

179. Rensen, S. S. M., Doevendans, P. A. F. M. & van Eys, G. J. J. M. Regulation and characteristics of vascular smooth muscle cell phenotypic diversity. *Netherlands Heart Journal* vol. 15 100–108 Preprint at https://doi.org/10.1007/BF03085963 (2007).

180. Petsophonsakul, P., Furmanik, M., Forsythe, R., Dweck, M., Schurink, G. W., Natour, E., Reutelingsperger, C., Jacobs, M., Mees, B. & Schurgers, L. Role of Vascular Smooth Muscle Cell Phenotypic Switching and Calcification in Aortic Aneurysm Formation. *Arterioscler Thromb Vasc Biol* **39**, 1351–1368 (2019).

181. Yu, C. K., Xu, T., Assoian, R. K. & Rader, D. J. Mining the Stiffness-Sensitive Transcriptome in Human Vascular Smooth Muscle Cells Identifies Long Noncoding RNA Stiffness Regulators. *Arterioscler Thromb Vasc Biol* **38**, 164–173 (2018).

182. Qiu, J., Zheng, Y., Hu, J., Liao, D., Gregersen, H., Deng, X., Fan, Y. & Wang, G. Biomechanical regulation of vascular smooth muscle cell functions: From

in vitro to in vivo understanding. *Journal of the Royal Society Interface* vol. 11 Preprint at https://doi.org/10.1098/rsif.2013.0852 (2014).

183. Xie, S. A., Zhang, T., Wang, J., Zhao, F., Zhang, Y. P., Yao, W. J., Hur, S. S., Yeh, Y. T., Pang, W., Zheng, L. S., Fan, Y. B., Kong, W., Wang, X., Chiu, J. J. & Zhou, J. Matrix stiffness determines the phenotype of vascular smooth muscle cell in vitro and in vivo: Role of DNA methyltransferase 1. *Biomaterials* **155**, 203–216 (2018).

184. Peyton, S. R., Kim, P. D., Ghajar, C. M., Seliktar, D. & Putnam, A. J. The effects of matrix stiffness and RhoA on the phenotypic plasticity of smooth muscle cells in a 3-D biosynthetic hydrogel system. *Biomaterials* **29**, 2597–2607 (2008).

185. Alexander, M. R. & Owens, G. K. Epigenetic Control of Smooth Muscle Cell Differentiation and Phenotypic Switching in Vascular Development and Disease. *Annu Rev Physiol* **74**, 13–40 (2012).

186. Frid, M. G., Moiseeva, E. P. & Stenmark, K. R. Multiple phenotypically distinct smooth muscle cell populations exist in the adult and developing bovine pulmonary arterial media in vivo. *Circ Res* **75**, 669–681 (1994).

187. Kong, Y., Hsieh, C. H. & Alonso, L. C. ANRIL: A lncRNA at the CDKN2A/B locus with roles in cancer and metabolic disease. *Front Endocrinol (Lausanne)* **9**, 405 (2018).

188. Cheung, C., Bernardo, A. S., Pedersen, R. A. & Sinha, S. Directed differentiation of embryonic origin-specific vascular smooth muscle subtypes from human pluripotent stem cells. *Nat Protoc* **9**, 929–938 (2014).

189. Ayoubi, S., Sheikh, S. P. & Eskildsen, T. V. Human induced pluripotent stem cell-derived vascular smooth muscle cells: differentiation and therapeutic potential. *Cardiovasc Res* **113**, 1282–1293 (2017).

190. Cheung, C., Bernardo, A. S., Trotter, M. W. B., Pedersen, R. A. & Sinha, S. Generation of human vascular smooth muscle subtypes provides insight into embryological origin–dependent disease susceptibility. *Nature Biotechnology 2012 30:2* **30**, 165–173 (2012).

191. Mozafari, H., Zhou, C. & Gu, L. Mechanical contribution of vascular smooth muscle cells in the tunica media of artery. *Nanotechnol Rev* **8**, 50–60 (2019).

192. O'Connell, M. K., Murthy, S., Phan, S., Xu, C., Buchanan, J. A., Spilker, R., Dalman, R. L., Zarins, C. K., Denk, W. & Taylor, C. A. The three-dimensional micro- and nanostructure of the aortic medial lamellar unit measured using 3D confocal and electron microscopy imaging. *Matrix Biology* **27**, 171–181 (2008).

193. Chang, S., Song, S., Lee, J., Yoon, J., Park, J., Choi, S., Park, J.-K., Choi, K. & Choi, C. Phenotypic Modulation of Primary Vascular Smooth Muscle Cells by Short-Term Culture on Micropatterned Substrate. *PLoS One* **9**, e88089 (2014).

194. Chang, S., Song, S., Lee, J., Yoon, J., Park, J., Choi, S., Park, J. K., Choi, K. & Choi, C. Phenotypic modulation of primary vascular smooth muscle cells by short-term culture on micropatterned substrate. *PLoS One* **9**, (2014).

195. Roberts, R., Stewart, A. F. R., Wells, G. A., Williams, K. A., Kavaslar, N. & McPherson, R. Identifying genes for coronary artery disease: An idea whose time has come. *Canadian Journal of Cardiology* **23**, 7A-15A (2007).

196. Helgadottir, A., Thorleifsson, G., Manolescu, A., Gretarsdottir, S., Blondal, T., Jonasdottir, A. A., Jonasdottir, A. A., Sigurdsson, A., Baker, A., Palsson, A., Masson, G., Gudbjartsson, D. F., Magnusson, K. P., Andersen, K., Levey, A. I., Jonsdottir, T., … Stefansson, K. A common variant on chromosome 9p21 affects the risk of myocardial infarction. *Science (1979)* **316**, 1491–1494 (2007).

197. Harismendy, O., Notani, D., Song, X., Rahim, N. G. & Frazer, K. A. 9p21 DNA variants associated with Coronary Artery Disease impair IFN-γ signaling response. *Nature* **470**, 264–268 (2011).

198. Larson, M. G., Atwood, L. D., Benjamin, E. J., Cupples, L. A., D'Agostino, R. B. S., Fox, C. S., Govindaraju, D. R., Guo, C.-Y., Heard-Costa, N. L., Hwang, S.-J., Murabito, J. M., Newton-Cheh, C., O'Donnell, C. J., Seshadri, S., Vasan, R. S., Wang, T. J., … Levy, D. Framingham Heart Study 100K project: Genome-wide associations for cardiovascular disease outcomes. *BMC Med Genet* **8 Suppl 1**, S5 (2007).

199. Altschuler, S. J. & Wu, L. F. Cellular heterogeneity: when do differences make a difference? *Cell* **141**, 559 (2010).

200. Dagogo-Jack, I. & Shaw, A. T. Tumour heterogeneity and resistance to cancer therapies. *Nature Reviews Clinical Oncology 2017 15:2* **15**, 81–94 (2017).

201. Syed, N. A., Bhatti, A., Ahmed, S., Syed, H. & John, P. Single-cell omics in metabolic disorders. *Single-Cell Omics: Volume 2: Application in Biomedicine and Agriculture* 153–164 (2019) doi:10.1016/B978-0-12-817532-3.00008-6.

202. Fu, J., Akat, K. M., Sun, Z., Zhang, W., Schlondorff, D., Liu, Z., Tuschl, T., Lee, K. & He, J. C. Single-cell RNA profiling of glomerular cells shows dynamic changes in experimental diabetic kidney disease. *Journal of the American Society of Nephrology* **30**, 533–545 (2019).

203. Holmes, M. v., Richardson, T. G., Ference, B. A., Davies, N. M. & Davey Smith, G. Integrating genomics with biomarkers and therapeutic targets to

invigorate cardiovascular drug development. *Nature Reviews Cardiology 2021 18:6* **18**, 435–453 (2021).

204. Wallstrom, G., Anderson, K. S. & Labaer, J. Biomarker discovery for heterogeneous diseases. *Cancer Epidemiology Biomarkers and Prevention* **22**, 747–755 (2013).

205. Motterle, A., Pu, X., Wood, H., Xiao, Q., Gor, S., Liang ng, F., Chan, K., Cross, F., Shohreh, B., Poston, R. N., Tucker, A. T., Caulfield, M. J. & Ye, S. Functional analyses of coronary artery disease associated variation on chromosome 9p21 in vascular smooth muscle cells. *Hum Mol Genet* **21**, 4021–4029 (2012).

206. Hvichia, G. E., Parveen, Z., Wagner, C., Janning, M., Quidde, J., Stein, A., Müller, V., Loges, S., Neves, R. P. L., Stoecklein, N. H., Wikman, H., Riethdorf, S., Pantel, K. & Gorges, T. M. A novel microfluidic platform for size and deformability based separation and the subsequent molecular characterization of viable circulating tumor cells. *Int J Cancer* **138**, 2894–2904 (2016).

207. Ribeiro-Samy, S., Oliveira, M. I., Pereira-Veiga, T., Muinelo-Romay, L., Carvalho, S., Gaspar, J., Freitas, P. P., López-López, R., Costa, C. & Diéguez, L. Fast and efficient microfluidic cell filter for isolation of circulating tumor cells from unprocessed whole blood of colorectal cancer patients. *Scientific Reports 2019 9:1* **9**, 1–12 (2019).

208. Chen, Z., Luo, X., Zhao, X., Yang, M. & Wen, C. Label-free cell sorting strategies via biophysical and biochemical gradients. *J Orthop Translat* **17**, 55 (2019).

209. Ai, Y. & Li, P. Label-free multivariate biophysical phenotyping-activated acoustic sorting at the single-cell level. *Anal Chem* **93**, 4108–4117 (2021).

210. Volpato, V. & Webber, C. Addressing variability in iPSC-derived models of human disease: guidelines to promote reproducibility. *Dis Model Mech* **13**, (2020).

211. Paddillaya, N., Mishra, A., Kondaiah, P., Pullarkat, P., Menon, G. I. & Gundiah, N. Biophysics of Cell-Substrate Interactions Under Shear. *Front Cell Dev Biol* **7**, 251 (2019).

212. Zhao, Z., Guo, Y. Y., Liu, Y., Sun, L., Chen, B., Wang, C., Chen, T., Wang, Y., Li, Y., Dong, Q., Ai, L., Wang, R., Gu, Y. & Li, X. Individualized lncRNA differential expression profile reveals heterogeneity of breast cancer. *Oncogene 2021 40:27* **40**, 4604–4614 (2021).

213. Liang, Y. L., Zhang, Y., Tan, X. R., Qiao, H., Liu, S. R., Tang, L. L., Mao, Y. P., Chen, L., Li, W. F., Zhou, G. Q., Zhao, Y., Li, J. Y., Li, Q., Huang, S. Y.,

Gong, S., Zheng, Z. Q., … Liu, N. A lncRNA signature associated with tumor immune heterogeneity predicts distant metastasis in locoregionally advanced nasopharyngeal carcinoma. *Nature Communications 2022 13:1* **13**, 1–12 (2022).

214. Jandl, K., Thekkekara Puthenparampil, H., Marsh, L. M., Hoffmann, J., Wilhelm, J., Veith, C., Sinn, K., Klepetko, W., Olschewski, H., Olschewski, A., Brock, M. & Kwapiszewska, G. Long non-coding RNAs influence the transcriptome in pulmonary arterial hypertension: the role of PAXIP1-AS1. *J Pathol* **247**, 357–370 (2019).

215. Simion, V., Zhou, H., Pierce, J. B., Yang, D., Haemmig, S., Tesmenitsky, Y., Sukhova, G., Stone, P. H., Libby, P. & Feinberg, M. W. LncRNA VINAS regulates atherosclerosis by modulating NF-κB and MAPK signaling. *JCI Insight* **5**, (2020).

216. Cho, H., Li, Y., Archacki, S., Wang, F., Yu, G., Chakrabarti, S., Guo, Y., Chen, Q. & Wang, Q. K. Splice variants of lncRNA RNA ANRIL exert opposing effects on endothelial cell activities associated with coronary artery disease. *RNA Biol* **17**, 1391–1401 (2020).

217. Banisadr, A., Eick, M., Beri, P., Parisian, A. D., Yeoman, B., Placone, J. K., Engler, A. J. & Furnari, F. EGFRvIII uses intrinsic and extrinsic mechanisms to reduce glioma adhesion and increase migration. *J Cell Sci* **133**, (2020).

218. Consortium, T. G. O., Ashburner, M., Ball, C. A., Blake, J. A., Botstein, D., Butler, H., Cherry, J. M., Davis, A. P., Dolinski, K., Dwight, S. S., Eppig, J. T., Harris, M. A., Hill, D. P., Issel-Tarver, L., Kasarskis, A., Lewis, S., … Sherlock, G. Gene Ontology: tool for the unification of biology. *Nat Genet* **25**, 25 (2000).

219. Consortium, T. G. O. The Gene Ontology resource: enriching a GOld mine. *Nucleic Acids Res* **49**, D325 (2021).

220. H, M., A, M., D, E., X, H. & PD, T. PANTHER version 14: more genomes, a new PANTHER GO-slim and improvements in enrichment analysis tools. *Nucleic Acids Res* **47**, D419–D426 (2019).

221. Kong, Y., Hsieh, C. H. & Alonso, L. C. ANRIL: A lncRNA at the CDKN2A/B locus with roles in cancer and metabolic disease. *Front Endocrinol (Lausanne)* **9**, 405 (2018).

222. Engler, A. J., Sen, S., Sweeney, H. L. & Discher, D. E. Matrix elasticity directs stem cell lineage specification. *Cell* **126**, 677–689 (2006).

223. Vincent, L. G., Choi, Y. S., Alonso-Latorre, B., del Álamo, J. C. & Engler, A. J. Mesenchymal stem cell durotaxis depends on substrate stiffness gradient strength. *Biotechnol J* **8**, 472–484 (2013).

224. Tang, L., Dai, F., Liu, Y., Yu, X., Huang, C., Wang, Y. & Yao, W. RhoA/ROCK signaling regulates smooth muscle phenotypic modulation and vascular remodeling via the JNK pathway and vimentin cytoskeleton. *Pharmacol Res* **133**, 201–212 (2018).

225. Talwar, S., Kant, A., Xu, T., Shenoy, V. B. & Assoian, R. K. Mechanosensitive smooth muscle cell phenotypic plasticity emerging from a null state and the balance between Rac and Rho. *Cell Rep* **35**, 109019 (2021).